Consolidation of High Melting SiO_2-Al_2O_3-La_2O_3 Glass Powders with Gas Pressure Vacuum Viscous Sintering Technology

Dissertation

zur Erlangung des akademischen Grades doctor rerum naturalium

(Dr. rer. nat.)

vorgelegt dem Rat der Chemisch-Geowissenschaftlichen Fakultät der Friedrich-Schiller-Universität Jena

von Master of Science, Zhiwen Pan

geboren am 28.05.1981 in Guangdong, China

Gutachter:

1. PD. Dr. Antje Kriltz

2. Prof. Dr. Hartmut Bartelt

Tag der Verteidigung: 17.02.2016

Acknowledgements

This dissertation is based on the 3 years of work in Leibniz Institute of Photonic Technology Jena, in the working group of Fiber Optics (FA.21). I would like to show my grateful to all my dear colleagues, for offering me a very nice working environment.

My deepest gratitude goes foremost to my supervisors: Dr. Antje Kriltz and Dr. Wolfgang Seeber, who trusted me and gave me this opportunity to pursue my PhD work, supervising me and discussing with me for all the problems I had from time to time. I emphasize my grateful for the great effort from Dr. Kriltz who paid large amount of time in correcting this dissertation seriously, sentence by sentence, for several times. I am also glad to attend her thermodynamic lectures and learned from her. I would never forget the encouragement from Dr. Seeber for me to learn German and the interests in the industry.

I also want to present my sincere acknowledgement to Dr. Johannes Kirchhof and Dr. Kay Schuster for providing me abundant resources and help for the success of this work. The viscosity method developed here was inspired by the discussion with Dr. Kirchhof and his previous work. I also want to express my attitude to Dr. Schuster, without him and his trust; I cannot continue my work with hundreds of failed samples prepared and tens of working tools broken. In addition, he offered me a period of special time that I can focus on the writing, which I appreciated very much.

I would also like to give my special thanks to Doris Litzkendorf and Stephan Grimm, who were taking care of my first living in Jena. They guided me through all the necessary background knowledge of SAL glass system and its preparation technique. It was pleasant to share ideas with them, have intense discussions with them and to learn from them.

Moreover, I would like to thank Prof. Hartmut Bartelt, who showed up in every of my season report, broadened my mind to find the connection between my work and the scientific community, asked me questions which inspired me a lot.

I also owe a special debt of gratitude to Prof. Lothar Wondraczek, from whose great support at the final stage of this dissertation and enlightening lectures I have benefited a lot and academically prepared for the glass science part of this work.

I am also grateful to my colleague Benjamin Philipp Viktor Heiz for his excellent translation of the conclusion part into German in Swiss style.

I would never be able to finish this dissertation without the help of my dear colleagues. My sincere thanks also goes to Anne Matthes for the clear striae patterns taken from glasses at tiny inhomogeneity in refractive index, Dr. Frank Froehlich for all his kindness help and the expert measurements in FTIR, Claudia Aichele for the refractive index measurement, Dr. Jan Dellith, Christa Schmidt and Andy Scheffel for the devoting their efforts in XRD, SEM, BSE and AFM measurements, Dr. Gaëlle Delaizir in SPCTS laboratory France for the particle size distribution, Dr. Jens Kobelke for the intense discussions in every aspect in glass technology especially in fiber drawing and viscosity, Hardy Baierl for his genius ideas in solving hundreds of engineering problems in this work, Dr. Joerg Bierlich, Dr. Sonja Unger, Jens Kupis, Anka Schwuchow, Petra Dittmann, Birgit Mueller and Karin Hinze for sharing their precious experiences, Stefan Pochert and Andre Kalide for keeping me and the GPS furnace safe, Hans-Joachim Pissler for the experiment setup of the VSM method, Mattias Arnz and Wolfgang Ludwig for their excellent cutting and polishing technique in glass processing.

Last but not least, I would like to thank my wife, my parents and my little baby who is still in the belly for supporting me spiritually throughout the writing of this work.

Content

List of Figures

List of Tables

Abbreviations

RE	Rare earth
SAL	Lanthanum doped Aluminosilicate (glass)
GPWS	Gas Pressure-Assisted Vacuum Viscous Sintering
FEM	Finite Element Method
HP	Hot Pressing
HIP	Hot Isostatic Pressing
GPS	Gas Pressure Sintering
SPS	Spark Plasma Sintering
DC	Direct Current
VFT	Vogel-Fulcher-Tammann (equation)
Eq	Equation
FTIR	Fourier Transform Infrared
UV	Ultra Violet
VIS	Visible
MIR	Middle Infrared
DIC	Differential Interference Contrast (microscopy)
XRD	X-Ray Diffraction
FWHM	Full Width at Half Maximum
AFM	Atomic Force Microscopy
eV	Electronvolt
SE	Secondary Electrons
SEM	Scanning Electron Microscopy
BSE	Backscattered Electrons
DTA	Differential Thermal Analysis
EDX	Energy Dispersive X-ray Analysis
WDX	Wavelength Dispersive X-ray Analysis
GPa	Giga Pascal
VSM	Viscous Stretching Method
ODCs	Oxygen Deficient Centers

Motivation

Rare earth doped silica glasses have been widely used as gain medium in high power fiber lasers for its ability to provide highly efficient[15] and broad linewidth fiber lasing at 0.4 - 3 µm[10], to withstand high thermal shocks[1] (low thermal expansion coefficient) and to show high mechanical strength[2]. The SiO_2-Al_2O_3-La_2O_3 (SAL, RE as network modifier) glass is one most suitable glass host material[18, 22] for the RE dopants. However, not all these SAL glass compositions, which have superior thermal-mechanical properties, can be prepared by melting and quenching (crucible melting) technology. Some of them are reported unmelted due to the limitation of the Pt crucible to 1700°C[22].

An alternative method to prepare SAL glasses is proposed to separate the vitrification processes from the consolidation process. If the vitrification of the raw crystalline powder is carried out by other techniques, such as plasma melting[3], chemical precipitation (e.g. REPUSIL[4] developed in IPHT Jena) or sol-gel[5] process, the Pt crucible might not be necessary and therefore the temperature is not more limited to 1700 °C. Consequently, glasses from high temperature melting crystalline powders (> 1700 °C) can be fabricated in this way. However, the vitrified glasses from the above-mentioned vitrification technologies are normally agglomerated small particles, instead of a dense bulk. Hence, the remaining problem is to consolidate these glassy particles into bulk glasses without changing their properties. Therefore, consolidation of the already vitrified glassy powders is one critical step for high melting glass preparation. For the establishment of the basis of such a method, the feasibility, understanding and optimization of the consolidation process will be studied in this work using SAL glass as model glass.

Sintering technology has been used for the consolidation for the SAL glassy powder in this work. For simplicity, milled SAL glassy powders from crucible melting and quenching are directly used as the starting material as if they were obtained from preceding vitrification technologies. The temperature range for consolidation will be investigated from 100 K above T_g (glass transition temperature) to 100 K below the melting temperature of the SAL glass (1650 °C[22]). Since the working temperatures in sintering can be much lower than the working temperature in crucible melting, the viscosity of the SAL glasses can be very high. As the densification rate decreases with increasing viscosity[6], a compensating method for higher densification rate will be developed: a vacuum heating combined with a consequent capsule-free Gas Pressure Sintering (GPS) process. The applied gas pressure should not be too high, to avoid changing the structure but sufficient to accelerate the densification rate. This process is termed as Gas Pressure Vacuum Viscous Sintering (GPWS) in this work.

The first challenge in this work is to find the suitable sintering parameters such as sintering temperature, dwelling time, particle size and the gas pressure for the densification process. Therefore, theoretical investigations based on sintering theory and numerical simulations will be carried out before experimental trials. In this case, the viscosity-temperature relationship of the model glass plays a fundamental role according to the viscous sintering theory. Therefore, the determination of viscosity-temperature relationship is of significant importance. A here developed viscous stretching method will be presented and applied for the measurement of viscosity at low to middle temperature range. On the other hand, the viscosity at high temperature region will be estimated via a Finite Element Method (FEM) model, with which the understanding of mass transportation (diffusion and convection) and viscous behavior of the glass will be present as well. In addition, surface tension and diffusion coefficient will be possible to obtain in this FEM model.

Except for the densification, the second challenge in this work belongs to the possible generation of inhomogeneities during the consolidation. Inhomogeneities, such as crystallization, phase separation, bubbles, absorption groups and striae will be examined in GPWS SAL glasses sintered at different working conditions. For understanding the generation of these inhomogeneities and avoiding them in the future, the original of these inhomogeneities will be discussed.

Finally, the feasible and optimized working conditions for consolidation of SAL model glass will be present such that full densification is achieved without generating new inhomogeneities. The requirements for the preceding vitrification process will also be concluded. With the successful of this work, a big step would be made heading forward to the enlightening future that the temperature limit will be significantly extended for glass preparation from crystalline powders.

Chapter 1 Introduction

1.1 SiO_2-Al_2O_3-La_2O_3 glass host for Rare Earth dopants

Rare earth modified silicate glasses were known for their ability to generate colors in glasses[23]. Nowadays, they are widely used in high power lasers[7 - 11], nonlinear optics[12], ultrafast fiber oscillators[13] and optical sensing[14] due to their unique optical and magnetic properties[15]. Versatile lasing wavelengths[15, 16] (Figure 1) can be obtained by doping different active RE ions[9, 10] such as Yb^{3+}, Nd^{3+} and Er^{3+}. However, only small amount[17,18] of RE can be high-dispersively doped in the silicate or phosphate glass without clustering. According to the study from Shelby[18], direct binary RE oxide-silica glass systems show a broad region of immiscibility from less than 1 mol% to 20 mol% of RE oxide. Therefore, a ternary silica glass system is necessary, in other words, one additional co-dopant is required. Alumina as co-dopant in RE doped silica glass has been well studied by Shelby[18] and shows a good glass formation ability. For this reason, alumina is used as the co-dopant in our RE doped silica glass. Among all RE identities, Lanthanum has the widest glass formation region due to its minimum in cation field strength[18], which is represented by Z/r^2, where Z and r are the ionic charge and the ionic radius, respectively. It should be noticed that in Figure 1 Lanthanum is not in the list which indicates that no available optical transition for lanthanum ions exists in this region, so it appears "passive" when compared to the other "active" RE ions with optical transition such as Yb^{3+}, Er^{+3}, Tm^{3+} etc. However, Lanthanum oxide doped aluminosilicate glass (SAL) has high refractive index, density, elastic modulus, hardness[19] and a great chemical durability[20] and hence manifests as an optimized glass host for doping with active RE ions. Additionally, considering the compatibility of RE

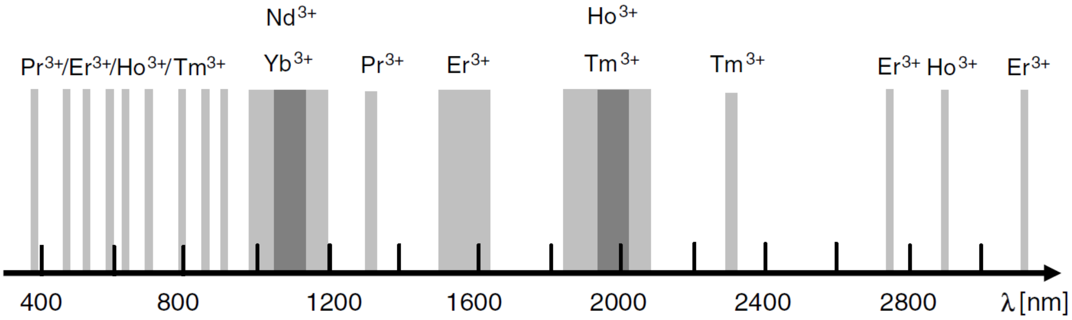

Figure 1. Accessible (absorption/emission) wavelengths by rare earth dopants [10]

elements, it should be also feasible to substitute partially the lanthanum oxide by active RE oxides, e.g. Yb^{+3}. The passive SAL glass hosts and the Ytterbium doped SAL glass (Yb-SAL) are therefore chosen as the model glass for the study in this work.

1.2 Compositions for the model SAL glass

Figure 2 shows the glass formation region of the SAL glass system. To achieve the highest compatibility for stacking into silica glass tubes during fiber drawing, a high concentration in SiO_2 is preferred. Thus 70 mol% SiO_2 is chosen according to Figure 2.

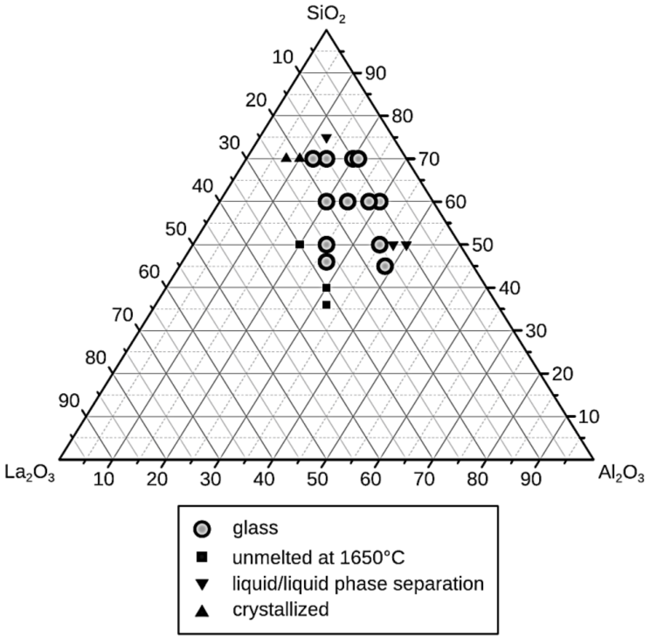

Figure 2. The glass forming region of SiO_2-Al_2O_3-La_2O_3 glass system (mol%) [22].

In addition, high amount of Al_2O_3 is preferred to improve the solubility of RE ions. It is also known that alumina could partially act as a network modifier[20], which degrades the connectivity of the glass network. This results in lowering liquidus temperature of the glass melt. In addition, the Al_2O_3 dopants higher the solubility of La in silica glass. According to glass forming region of SAL glass in Figure 2, 20 mol% of Al_2O_3 is the highest obtainable amount, so the composition for model SAL glass is chosen to be 70 SiO_2 –20 Al_2O_3 –10 La_2O_3 (in mol%) corresponding to the upper right corner of the SAL glass formation region. This composition has already been fabricated in IPHT Jena [21] by melting and quenching (crucible melting) technology. Due to the compatibility between RE elements[15], the La_2O_3 concentration in the model SAL glass can therefore be substituted by active RE dopants, such as Yb_2O_3 which is referred to Yb-SAL glass in this work.

1.3 Fabrication of high melting SAL glass

The high liquidus temperature (viscosity at about 10^4 Pas) of SAL and Yb-SAL glasses results in a high "melting" temperature for fabrication. Shelby[18] has demonstrated that the liquidus temperature will increase with increasing RE amount in RE aluminosilicate ternary glass systems. It is reported that the lanthanum concentration is limited to 30 mol%[22] in the SAL glass system due to the maximum melting temperature allowed by the platinum crucibles of about 1700 ℃ (Figure 2). Since it is first used in 1871[23], the high purity glassmaking has been enabled by using the platinum crucible melting and quenching technology of crystalline powders. However, adequate low viscosity is required for a subsequent casting process, which limits the working temperature above the liquidus point. Besides, this limitation generates inhomogeneity of striae during casting in molds. Platinum intrusions[24] near platinum melting point is always challenging in this technology. An alternative way to fabricate bulk material at a temperature below the melting/liquidus point is sintering.

1.4 Sintering technology

Sintering is a thermal activation process that bonds contacting particles together into a bulk object. The driving force is the reduction of the surface energy in the system from a thermodynamic point of view. The activation energy for a diffusion process is generally much lower than the activation energy for melting; therefore, sintering instead of direct melting is beneficial in fabrication of bulk material with high melting temperature, such as SAL glass system.

1.5 Viscous sintering

Since glass is amorphous, there are no grain boundaries between particles. Compared to the sintering of crystalline powders, the densification rate and grain growth behavior in glass sintering are largely determined by its viscous flow[28]. Therefore, it is also termed as viscous sintering, where viscosity plays an important role. Figure 3 shows the difference in the coalescence of particles in sintering of crystalline powders (Figure 3A and Figure 3B) and in viscous sintering (Figure 3C), respectively. Instead of direct

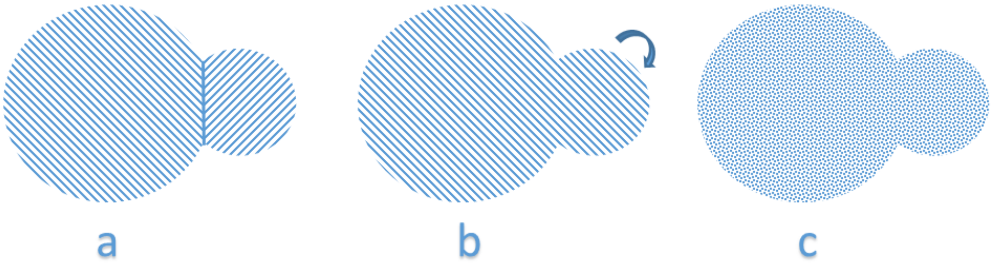

Figure 3. Particle coalescence in sintering: grain boundary between crystalline particles (a), grain growth by grain rotation of small particle (b), coalescence of amorphous particle without grain boundary (c).

coalescence as in viscous sintering, the crystalline powders with different orientations have to rotate before they coalesce which consumes extra energy. According to Boccaccini and coworkers[25], the viscous behavior of glass particles results in extra ability in sintering by shear strain. This could also be used to heal flaws in bulk glasses.

The drawback of viscous sintering as compared to the crystalline sintering is the lack of pore - grain boundary interaction that is an important action to bring the internal pores out of the sintered body. As a result, the pores with entrapped low diffusive gases, gases from decomposition, degassing or desorption will stay in the glass body. Once the gases are low diffusive, they are only able to flow up by buoyance force under damping force determined by viscosity, which increases significantly with decreasing temperature. So bubbles are often encountered in glass sintering particularly at lower temperature range.

1.6 Vacuum sintering

Vacuum sintering utilizes pumping system to maintain low atmospheric pressure in the sintering chamber. This is helpful to avoid entrapped gases in sintered glass and remove desorption gases from the surface of the glass powder. This helps to achieve full densification in viscous sintering, where bubbles are usually problematic. The pressure will be maintained below 0.1 mbar in our sintering furnace when “vacuum” is mentioned. Because of the existence of gas decomposition from raw powder, it is beneficial to apply vacuum to clean this potential entrapped gas in the final glass bulk.

1.7 Pressure-assisted sintering

For the purposes of collapsing vacuum bubbles as well as accelerating densification rate, external pressure has been used to assist the sintering of SAL glass. With external pressure, the densification becomes faster since the external pressure applies additional driven force except for the capillary force[26]. It is necessary to apply external pressure to compensate losses in the densification rate due to the lower sintering temperatures. It also enables the use of large particles instead of nanoparticles in sintering. The external pressure also reduces the final pore size in the final stage of sintering as compared to the pressureless sintering, resulting in lower porosity, wear losses and friction coefficient[27]. For this reason, pressure assisted sintering has been applied in fabrication of materials where strong mechanical strength is needed[28]. Table 1 shows some pressure application technologies for sintering and their typical working parameters. According to their stress states, three different types of pressure assisted sintering processes are available: with uniaxial stress, isostatic stress and shear stress.

Table 1. Pressure assisted sintering procedures and their typical working conditions for graphite die.

	Maximum Temperature	Maximum Pressure	Primary Stress	Dwelling Time
	°C	MPa		min
Hot Pressing(HP)	1000	50	uniaxial	~60
Hot Isostatic Pressing (HIP)[26]	2200	300	hydrostatic	~60-120
Gas Pressure Sintering (GPS)	2200	10	hydrostatic	~60
Spark Plasma Sintering (SPS)[28]	2200	100	uniaxial	~10
Hot Extrusion[28]	2200	50	shear	~1

1.8 Uniaxial hot pressing

The uniaxial Hot Pressing (HP) applies vertical stress through two up and down punches with powder compaction in between (Figure 4). The powder compaction encounters not only vertical but also radical pressure against the die wall, in which shear

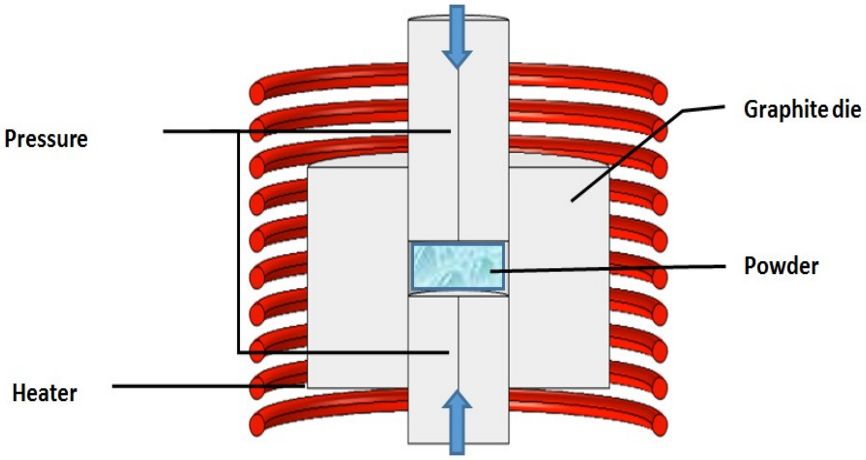

Figure 4. Scheme of uniaxial Hot Pressing (HP) with graphite dies for glass powder sintering.

stress is generated and is proportional to the applied pressure. The shear stress present in HP sintering is beneficial to the bonding between particles as well as to rupture any possible prior particle boundary precipitation, which otherwise may weaken the strength of the sintered material[29]. The problem of this technique always arises from the compact contaminations and the unequal vertical and radial pore compression.

Another pressure-assisted technique using a similar setup is known as Spark Plasma Sintering (SPS)[30]. The SPS supplies rapid heating by pulsed direct current (DC) ranging from milliseconds to seconds with 10-1000 amperes. In addition, GPa range of pressure is applied. Rapid densification is then achieved; however, the temperature distribution is not uniform inside the powder compacts.

1.9 Hot isostatic pressing

The Hot Isostatic Pressing (HIP) utilizes hydrostatic pressure from liquids or gases up to 300 MPa. In HIP, pore compression is isotropic, therefore an isotropic shrinkage will be expected after sintering, which means that the geometry can be maintained. Unlike the direct application of mechanical pressure in HP, the application of gas/liquid pressure as external pressure in HIP requires additional preparation steps. According to the different kinds of preparation processes, they are termed as capsule and capsule-free methods (Figure 5). The capsule method places powder in a container made of soft metal or glass. The container is then heated up and evacuated to remove all gases and volatile contaminations, before it is sealed and transferred to the HIP consolidation processing.

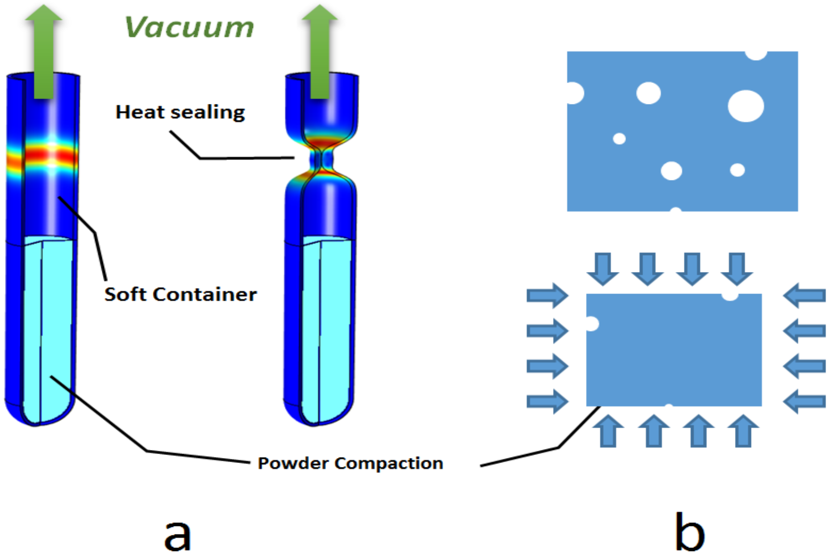

Figure 5. Sample preparation for HIP with capsule method (a) and capsule-free method (b)

The capsule-free method firstly sinters powder compaction at a very low pressure until isolated pores are formed. Then a low amount of penetration gases is applied to generate hydrostatic pressure to close isolated pores inside the compaction. The maximum pressure available in HIP is lower than that in HP. However, the impurities from the pistons in HP can be avoided in HIP.

Gas Pressure Sintering (GPS) is a variation technology of HIP that works usually below 100 bar (10 MPa). Except for accelerating densification and pore elimination in sintering, the GPS technology has also been used for sintering ceramics with similar gases in composition. Nitrogen was used in sintering Silicon nitride[31], so that the decomposition of silicon nitride is suppressed[32].

1.10 Working gas and its pressure

It is important to use a kind of gas with sufficient size in molecule dimensions so that its permeability in glass is very low. Otherwise, penetration of the gas takes place and the external pressure fails to apply. The chemical reactivity to the sintering glass can be chosen according to different applications. In our case, the inert gas argon is chosen. Although the densification rate increases with increasing external pressure, it is also known[33] that both the ionic diffusion and the fluidity of liquids decreases with increasing pressure. In other words, the homogenizing process will be hindered if too high pressure is applied. Figure 6 shows the calculation of the obtainable final relative density in pressure assisted sintering according to various particle sizes. It demonstrates

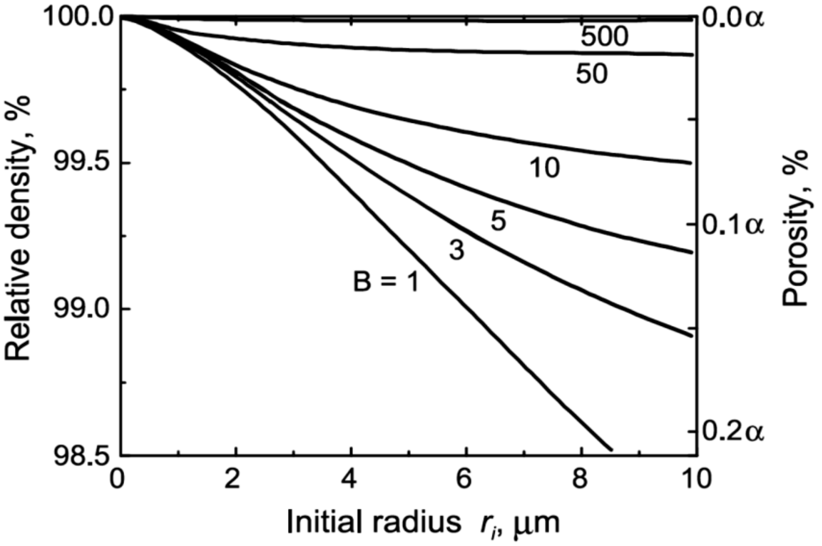

Figure 6. Pressure effect on final densification. B is pressure in unit of bar and r is pore size. [26].

that by using 500 bar the final density is only increased by 0.1 % compared to 50 bar if 10 µm starting particles are used. In other words, 50 bar is adequate to achieve a 99.8 % relative density.

Chapter 2 Principle of glass sintering theory

2.1 Development of sintering theory

Although sintering has been used to strengthen clay and pottery in fire since thousands of years according to the discovery by archeological artifacts[34], its scientific study had just begun in the early 1900s. The documentation of first empirical observation about sintering pottery and simple metals can be found generally before 1700, and after that lots of trial experiments in sintering had begun. This period of trial with some quantitative detail in processing lasted for about two hundred years until the first development of qualitative sintering models in 1945. In 1900s the concept of surface energy[35;36] and the atomic theory for mass transport mechanisms were critical steps for the development of sintering theory. Since then, many models and mechanisms have been developed: such as dislocation models[37-40], diffusion models[41-45], concurrent dislocation and diffusion models[46-49], viscous sintering model[,4,50-55]and microstructure model[56-63] which is based on sintering of a compact of tetrakaidecahedron (Figure 7) grains.

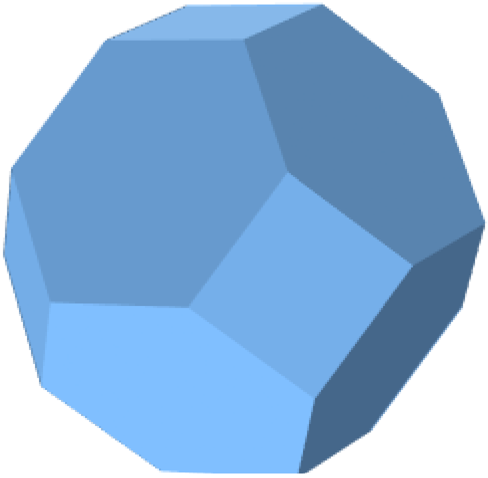

Figure 7. The tetrakaidecahedron grain structure contains 14 faces.

All these models are listed at Table 2. The analytical models that were introduced above provide qualitative understanding of sintering due to their simplicity in geometry. Quantitative predications of real powder sintering can be given by numerical modeling with rate equations provided by analytic models. The empirical models are also very useful, such as Herring's scaling law[26], which summarized the relation between sintering time and particle size. Until now, there is no single theory that is able to describe both the densification and the evolution of microstructure in sintering due to the practical complexity. Therefore, the modern theories of sintering are presented by separate approaches. Some of them are given in empirical equations for specific sintering or others are given in a semi-empirical way via statistical methods.

Table 2. Sintering models[66,67 and 68]

Approach		Characteristic/Applied field	Limitations
Analytical Models	Dislocation Model	Kinetic, plastic flow, initial stage in sintering when dislocations are present, metals, ionic compounds.	Not for ceramics, complement to diffusion model
	Diffusion Model	Kinetic, thermal activated transportation of mass and vacancies in all stages of sintering	complement to dislocation model
	Viscosity Model	Kinetic, phenomenological model used widely in computer simulation for glass and polymers	No fundamental explanation
Microstructure Model		Microstructure evolution, intermediate and final stage	Non-kinetic
Numerical Model		Without simplified geometry assumptions	Numerical methods required
Herring's Scaling laws		Prediction of particle size and sintering time	Self-similarity assumption
Statistical Models		Using statistical methods in analyzing sintering	Semi-empirical analysis
Empirical Models		Empirical derived equations for specific specimens	Mathematical fit, non-physical

2.2 Modern sintering theory

2.2.1 Thermodynamic explanation of sintering

Sintering is an irreversible process where the excess surface energy is consumed by densification and grain coarsening processes (Figure 8). Taking particles of sizes from 100 nm to 1 µm, the typical values of specific surface area is about S = 1 - 10 m^2/g, with a surface energy in the range of 1 – 4 J/m^2 for most glasses and ceramics[64]. The resulting specific surface energy is about 1 – 40 *J/g*. Although it is small compared to the enthalpy of chemical reactions (>1 *kJ/g*), it is still enough to drive densification process in sintering. However, not all of the excess surface energy can be consumed by densification; a certain part is "wasted" by grain coarsening. The term "grain coarsening" or "grain growth" is used to describe the increase in size of grains while decreasing in quantity during sintering. Therefore, densification and grain coarsening consume

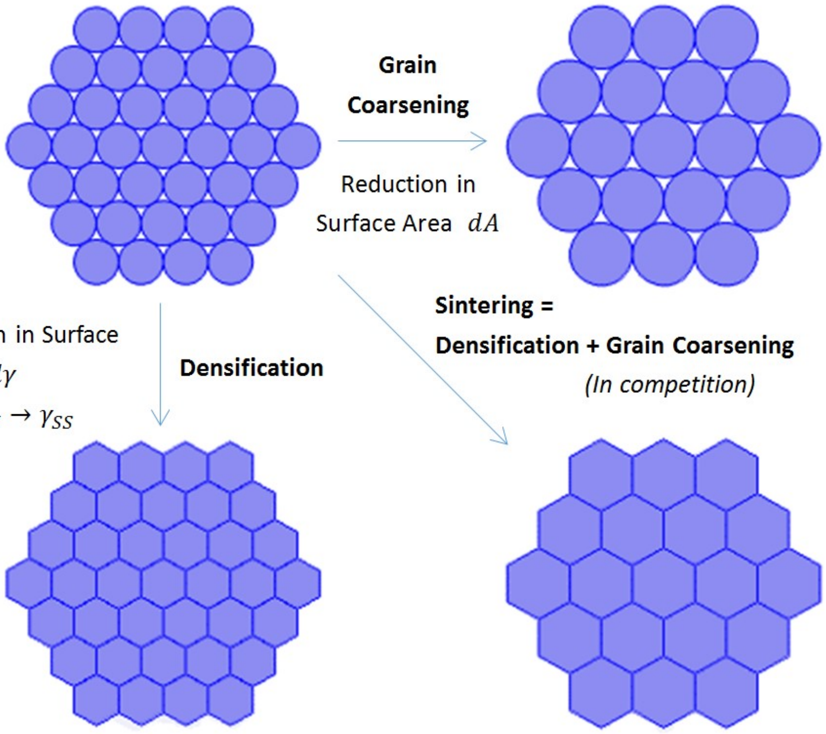

Figure 8. Sintering is represented by the combination of densification and grain coarsening processes. $dA, d\gamma, \gamma_{SV}, \gamma_{SS}$ are the change in surface areas, change in surface energy, solid-vapor interfacial energy and solid-solid energy respectively.

excess surface energy in competition. Since sintering usually occurs at a constant temperature and pressure with mass conservation, a comprehensive thermodynamic equation for the change of excess surface energy dG in both processes is given in Eq. (1)

$$dG = d(\gamma A) = \gamma dA + A d\gamma \tag{1}$$

where γ is surface energy and A is surface area. $\gamma\, dA$ represents the grain coarsening process with decrease in surface area ($dA < 0$) while $Ad\gamma$ stands for densification by changing solid-vapor interface to solid-solid interfaces. In other words, grain boundaries (solid-solid interface γ_{SS}) are created in densification so $dA_{SS} > 0$ while solid-vapor surface (γ_{SV}) are annihilating so $dA_{SV} < 0$. Assuming that the systems contain only two kinds of surfaces (solid-solid and solid-vapor), the change of free energy at constant temperature and pressure could be expressed alternatively by

$$dG = \gamma_{SV} dA_{SV} + \gamma_{SS} dA_{SS} \tag{2}$$

Hence sintering begins when $dG < 0$ and stops when $\gamma_{SV} dA_{SV} = -\gamma_{SS} dA_{SS}$, which means the creation of solid-solid interface (densification) equals to

$$\Delta A_{SS} = -\Delta A_{SV} \frac{\gamma_{SV}}{\gamma_{SS}} \tag{3}$$

2.2.2 Driving force

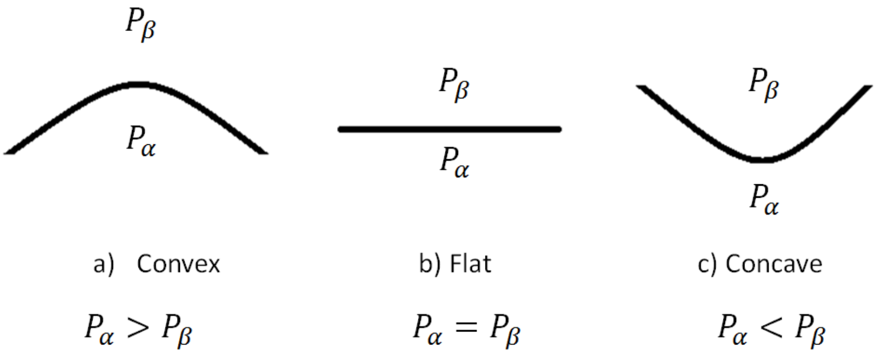

Figure 9. Additional pressure generated by curved surfaces. (a) by convex surface (b) by flat surface and (c) by concave surface looking from the α phase.

Curved interfaces cause additional pressure as compared to flat interfaces according to its average curvature: convex or concave (Figure 9). This additional curvature induced pressure ΔP, which is given by the Young-Laplace Equation[65] as shown in Eq.(4):

$$\Delta P = \gamma K = \gamma\left(\frac{1}{r_1} + \frac{1}{r_2}\right) \tag{4}$$

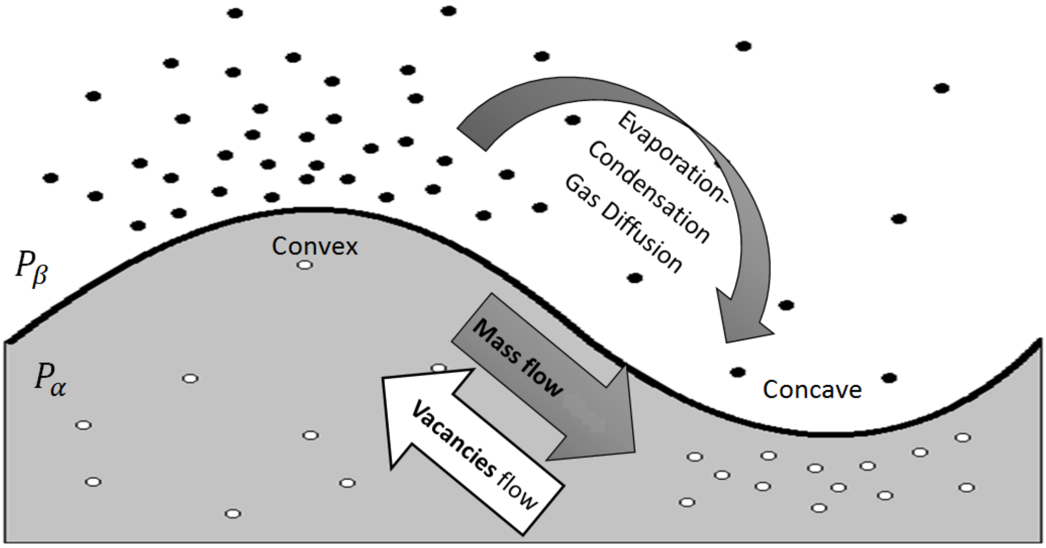

Figure 10. Mass flow caused by curved surfaces during sintering.

It delivers several MPa pressure with radii of curvatures in the micrometers scale. The neck region between neighboring particles is concave while the particle surface is usually convex as shown in Figure 10. Assuming that α and β are two phases of a single component in equilibrium; they are separated by a curved surface with curvature K. If the temperature is constant, the infinitesimal and reversible change of chemical potential between two phases in equilibrium follows:

$$d\mu_{\alpha} = d\mu_{\beta} \tag{5}$$

$$V_{m\alpha} dP_{\alpha} - S_{\alpha} dT = V_{m\beta} dP_{\beta} - S_{\beta} dT \tag{6}$$

where μ is chemical potential, V_m is molar volume, P is pressure and T is temperature. The subnotes are indicating different phases. Since $dT = 0$, Eq. (6) breaks down to

$$V_{m\alpha} dP_{\alpha} = V_{m\beta} dP_{\beta} \tag{7}$$

By minus $V_{m\alpha} dP_{\beta}$ from both sides of Eq. (7) [67], one gets

$$V_{m\alpha} d(P_{\alpha} - P_{\beta}) = (V_{m\beta} - V_{m\alpha}) dP_{\beta} \tag{8}$$

Substituting Young-Laplace Equation: $P_\alpha - P_\beta = \gamma K$ into Eq. (8) [67],

$$dP_{\beta} = \frac{\gamma V_{m\alpha}}{V_{m\beta} - V_{m\alpha}} dK \tag{9}$$

Eq. (9) is obtained. Considering a change of pressure from a flat surface P_{flat} to pressure P_β due to the change of curvature of interface from 0 to K, integrating Eq. (9),

$$\int_{P_{flat}}^{P_{\beta}} dP = \frac{\gamma V_{m\alpha}}{V_{m\beta} - V_{m\alpha}} \int_{0}^{K} dK \tag{10}$$

$$P_{\beta} - P_{flat} = \frac{V_{m\alpha}}{V_{m\beta} - V_{m\alpha}} \gamma K \tag{11}$$

we get Eq.(11)[67]. Similarly, minus $V_{m\beta} dP_\alpha$ on both sides of Eq. (7), one obtains

$$P_{\alpha} - P_{flat} = \frac{V_{m\beta}}{V_{m\beta} - V_{m\alpha}} \gamma K \tag{12}$$

If α phase is the condensed phase and β is the vapor phase, which means $V_{m\beta} \gg V_{m\alpha}$, Eq. (12) [67] breaks down to Eq. (13) [67].

$$P_{\alpha} = P_{flat} + \gamma K \tag{13}$$

Viewing from the side of condensed phase α, Figure 10 has depicted convex regions (K > 0), concave regions (K < 0) and a flat transient surface (K = 0). From Eq. (13), the pressure is higher in condensed phase near the convex region than in concave region. Therefore, a pressure gradient is built up inside the condensed phase pointing from convex to concave, which results in mass flow in the same direction. Also the vapor pressure is modified by the surface properties. Under the same condition: $V_{m\beta} \gg V_{m\alpha}$, it follows $V_{m\beta} - V_{m\alpha} \approx V_{m\beta}$, therefore Eq. (11) breaks down to

$$P_\beta - P_{flat} = \frac{V_{m\alpha}}{V_{m\beta}} \gamma K \tag{14}$$

If β is the vapor phase following the ideal gas law, this gives

$$V_{m\beta} = \frac{RT}{P_{flat}} \tag{15}$$

where R is gas constant. Substituting the expression of $V_{m\beta}$ in Eq. (15) into Eq. (14), one obtains

$$P_\beta = P_{flat}(1 + \frac{\gamma K V_{m\alpha}}{RT}) \tag{16}$$

Eq. (16) and Eq. (13) are the most fundamental equations for explanation of driving forces in sintering. From Eq. (16), the vapor pressure is higher above the convex surface while it is lower above the concave surface. Therefore, a similar pressure gradient is also able to build up pointing from the area above a convex surface to the area above concave surfaces. Under these pressure gradients, the difference in curvature over the whole surface will be vanishing. Consequently, a surface with uniform curvature is obtained. Alternatively, the vapor phase can be considered as consisting of a large amount of vacancies. The same rule can be applied to the vacancies in the condensed phase, which says a vapor pressure gradient exists inside the material with the opposite direction to the mass flow (Figure 10).

2.2.3 Sintering types

According to their working phases, there are three types of sintering: solid state sintering, liquid state sintering and viscous sintering. Solid state sintering provides the tailoring ability, which is widely used in sintering small ceramic and metal components with complicated geometry. The rigid grain cores are maintained and the bonding occurred by surface and boundary diffusion in solid state sintering. Therefore, the geometry of the green particle compaction can be preserved quite well with suitable procedure parameters and hence further machining is not necessary. Liquid phase sintering provides higher density and densification rate than solid state sintering. It is widely used in metal sintering where liquid phase spreads out into the boundary tunnels, causing lower porosity and enhanced densification rate. The viscous sintering is suited for amorphous material such as glasses and polymers. The densification rate depends on particle size, pore size and viscosity. Since grain boundaries are, absent in amorphous material, mechanisms such as grain boundary diffusion and pore-grain boundary migration are dismissed.

2.2.4 *Mass transport mechanisms*

Although several models have been introduced in the development of analytic sintering models, the physical fundamental of mass transport of matter is diffusion. The mass transport mechanisms are closely associated to point defects such as vacancies, solutes or impurities as well as dislocations, grain boundaries, phase boundaries and surfaces. The energy taken to stimulate atoms from surface defects is usually lower than in the bulk. Therefore, surface diffusion is faster than grain boundary diffusion, which is higher than the lattice diffusion. Therefore, surface diffusion dominates the initial stage of sintering. The grain boundary diffusion is normally one order of magnitude higher than that of lattice diffusion. Although the defects provide highways, there are still chances for atoms to diffuse across the interior, such as evaporation-condensation via the vapor phase and grain boundary diffusion via the interior. Figure 11 and Table 3 summarize different kinds of mass flows and how the defects are assisting diffusion. However, at disorder structures such as glasses, the concept of defects is no longer useful. The diffusion in glass is manifested by diffusion of network modifiers and gas molecules in a rigid glass network, which will be discussed in the further sections.

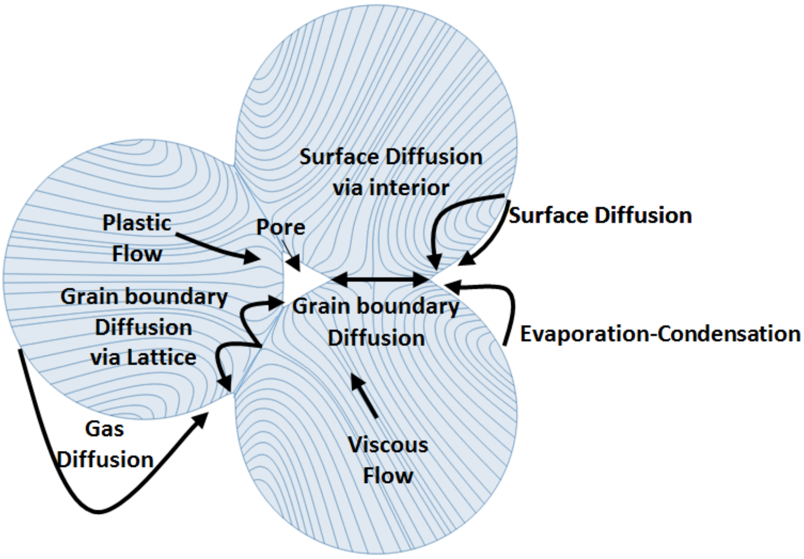

Figure 11. Material transport mechanisms during sintering (spheres) in the initial stage, the streamline represents the viscous fluid field in viscous sintering.

Table 3. Mass transport mechanisms in sintering[66,67 and 68].

Transport Mechanism	source	sink	notice
Surface diffusion	convex surface	concave surface	along the surface
Surface diffusion via Lattice	convex surface	concave surface	through interior
Gas diffusion	convex surface	concave surface	through vapor for longer distance than mean free path
Evaporation-condensation	boundary transition zone	concave surface	through vapor for distance shorter than mean free path
Volume diffusion	boundary transition zone	concave surface	across the interior
Grain boundary diffusion	lattice	concave surface	along grain boundary
Grain boundary diffusion via Lattice	lattice	concave surface	through interior
Viscous flow	lattice	lattice	collective motion of unit structure
Plastic flow	lattice	lattice	dislocation

2.2.5 Sintering stages

Sintering is divided into three stages in developing analytic densification models: the initial stage, intermediate stage and final stage. In the initial stage, the assumption of monosize sphere compact is made with loose pack (Figure 12a) that corresponds to roughly 64 % of theoretical density. The inter-particle necks grow up from the particle point contact via surface diffusion. In this stage the neck radius *X* grows up to *a*/3, where *a* is the particle radius (Figure 12b). There is nearly no shrinkage (3 % at most) in this stage and the density is below 70 %. Densification is not of too much importance in the initial stage of the sintering. Instead, taking *X/a* as sintering degree for neck growth, the time evolution of neck growth in this stage of sintering is presented in Eq. (17)

$$\frac{x}{a} = \frac{1}{a^k}\left[G \cdot M(T) \cdot t\right]^m \tag{17}$$

where *t* is time, *k* and *m* are radius and time dependent indices representing the sensitivity of sintering degree in dependence on particle size and time. *M(T)* is the mobility term for atoms and vacancies under the gradient of chemical potential arising from curvature. *G* is a geometry constant. From Eq. (17) the sintering degree in initial stage is proportional to the mobility term to the power of *m* and inversely proportional

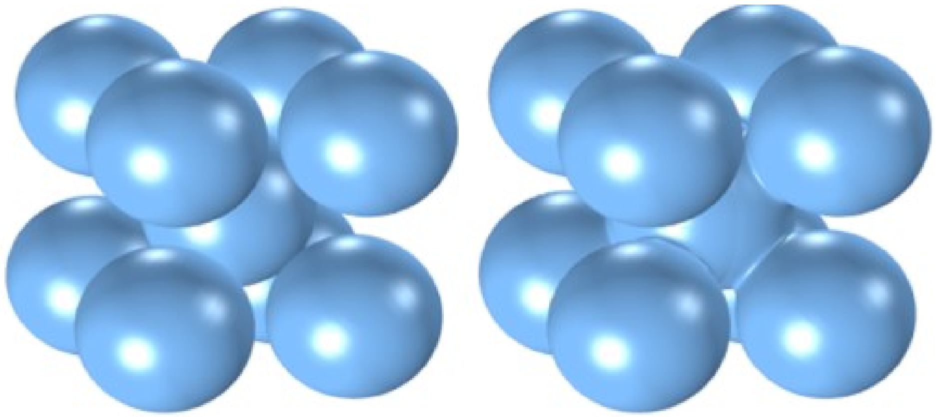

(a) Loose Pack *(b) Initial Stage*

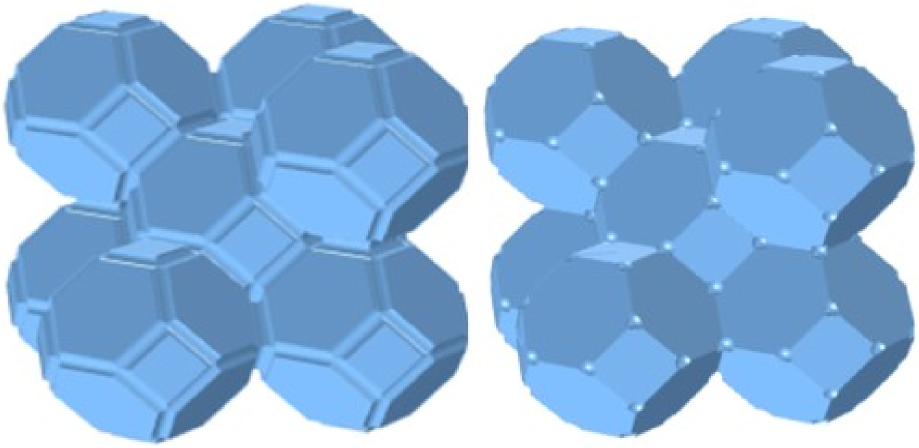

(c) Intermediate Stage *(d) Final Stage*

Figure 12. Scheme of different sintering stages for monosize spheres compaction.

to particle size to the power of *k*. These facts are summarized in Table 4.

In the intermediate stage of sintering, the inter-particle contacting area enlarges and becomes flat during neck growth. The neck size in this stage begins from *a*/3 to *a*/2 where about half of the pores are closed. In pace with the continuous enlargement, the particle shape changes from sphere to polygon, such as tetrakaidecahedron in Figure 12c. It is a stage dominated by densifying bulk transport mechanisms from about 70 % to 92 %, while the non-densifying surface transport mechanisms are inactive. One exception is the plastic flow, as a bulk transport mechanism; it is inactive due to the annihilations of defects. As a result, volume diffusion and grain boundary diffusion are the two dominant mechanisms for crystalline sintering while viscous flow governs the viscous sintering in both of the intermediate and final stage. For crystalline material, the densification rate, which is defined by $(1/\rho)d\rho/dt$, has been developed for this stage by Coble[58] in his kinetic model of compact of tetrakaidecahedron grains:

Table 4. Mechanisms of mass transport for neck growth in the initial stage of sintering.[66,67 and 68]

Mechanism in initial stage of sintering		m	k	M(T)	G
Surface transportation (non-densify)	Surface diffusion	1/7	0.57	$V_m\gamma_{SV}\frac{D_S}{RT}$	$56\delta_S$
	Surface diffusion via interior	1/5	0.60	$V_m\gamma_{SV}\frac{D_V}{RT}$	20
	Gas diffusion	1/5	0.60	$V_m\gamma_{SV}\frac{D_g}{RT}\frac{PV_m}{RT}$	20
	Evaporation-condensation	1/3	0.67	$\frac{PV_m\gamma_{SV}}{RT}\frac{\sqrt{M/2\pi RT}}{\rho^2}$	6
Bulk transportation (densify)	Volume diffusion	1/4	0.75	$V_m\gamma_{SV}\frac{D_V}{RT}$	80
	Grain boundary diffusion	1/6	0.67	$V_m\gamma_{SV}\frac{D_{GB}}{RT}$	$96\delta_{GB}$
	Viscous flow	1/2	0.50	$\frac{\gamma_{SV}}{\eta}$	3/2
	Plastic flow	1/2	0.50	$D_V\gamma_{SV}\frac{B}{RT}$	9π

D_S, D_V, D_g and D_{GB} are diffusion coefficients of surface, volume, gas and grain boundary diffusion, respectively.
δ_S and δ_{GB} are the thickness of the surface layer and grain boundary, respectively.
γ_{SV} and P are solid-vapor surface energy and vapor pressure of a flat surface, respectively.
M, B, ρ and V_m are molar weight, Burgers vector, density and molar volume, respectively.
η, R and T are viscosity, gas constant and absolute temperature, respectively.
(These calculations are based on two sphere models.)

$$\frac{1}{\rho}\frac{d\rho}{dt}=\frac{1}{a^k}G\cdot M(T)\cdot\phi^{\frac{k-1}{2}}\cdot V_m P_e \qquad (18)$$

where ϕ is the stress intensification factor and P_e is the effective sintering stress. The stress intensification factor ϕ is the ratio of the effective stress at the particle interface to the applied stress; it is an important parameter for pressure-assisted sintering. The geometry factor G is based on detail particle geometry. For amorphous material, the densification rate has been studied by Scherer[53] and could be expressed in the form of Eq. (18). The typical value of the mobility term *M(T)*, the effective sintering stress P_e and the geometry factor G for tetrakaidecahedron crystalline grain are shown in Table 5. G_0 is a constant that is determined by detailed geometry model used in the intermediate stage of viscous sintering, which is shown further in this chapter. P_i is the pressure of the entrapped gas in isolated pores in the final stage. The grain coarsening process in the initial stage is neglected due to the small inter-particle contact area.

However, in the intermediate stage, the grain coarsening by coalescence of smaller particles has been accelerating significantly due to the enlargement of the inter-particle contact area. In addition to grain growth, the pores are smoothing, becoming tubular along the grain edges and building an open channels network. With the grain coarsening process is going on, the pore diameter decreases. In the meanwhile, grain edges are elongated so as the pore length. This gradually leads to longer and thinner pores until the criterion of Rayleigh instability is fulfilled $l \geq \pi d$, where l is the pore length and d is the pore diameter. The pores are not able to maintain tubular anymore and eventually the channels pinch off and isolated pores are formed.

Table 5. Mass transportations in densification in intermediate and final stages of sintering[66, 67 and 68].

Transportation mechanism		***M(T)***	***k***	***G***	$\boldsymbol{P_e}$
Intermediate Stage of sintering	Volume diffusion	$\frac{D_V}{RT}$	2	40/3	$\frac{\gamma_{SV}}{r}$
	Grain boundary diffusion	$\frac{D_{GB}}{RT}$	3	95/2	$\frac{\gamma_{SV}}{r}$
	Viscous flow	$\frac{1}{\eta}$	1	G_0/V_m	$\frac{\gamma_{SV}}{r}$
Final stage of sintering	Volume diffusion	$\frac{D_V}{RT}$	2	40/3	$2\gamma_{SV} - aP_i$
	Grain boundary diffusion	$\frac{D_{GB}}{RT}$	3	15/2	$2\gamma_{SV} - aP_i$
	Viscous flow	$\frac{1}{\eta}$	1	$3/4V_m$	$2\gamma_{SV} - aP_i$

In the final stage, the sintering process is corresponding to the last 8 % of theoretical density. The target is to eliminate the residual isolated pores. These pores are no more open to the external surface and might be filled with the atmosphere gases or decomposition gases. Hence, in the final stage, the densification process slows down and merely stops. Then its competitor – the grain coarsening process, will consume larger parts of available surface energy. As a result, the grain coarsening process achieves the highest rate and becomes dominant in the final stage. The pores in this stage could be divided into two groups: attached and unattached pores to the grain boundary. The attached pores are formed during the intermediate stage. They are able to migrate together with the grain boundaries while the spontaneous grain coarsening process occurs to reduce the total grain boundary area. The residual unattached pores originate mostly from the starting particles or from the decomposition of gases. They will stay in the body thus; they are not able to get out via grain boundary movements.

If these pores are entrapped with high diffusive gases, they could be closed after the entrapped gases diffused out. Otherwise, these pores will never be closed in normal sintering.

2.3 Viscous sintering

2.3.1 Theory of glass sintering

The base of all viscous sintering models is the idea from Frenkel's work[6], in which he states that the dissipation energy of the viscous flow equals to the energy gained by the reduction of interfacial area. With dedicate simplification in geometry of the fluid field for different stages of sintering, the dissipation energy term is calculated.

In the initial stage, Frenkel[6] has assumed uniform uniaxial fluid field towards the neck in his two spheres coalescence model, which is equivalent to a cylinder flow. The expression of rate of dissipation energy $\dot{I}$ per unit volume is derived from the stretching of a viscous cylinder with one side fixed:

$$\dot{I} \qquad at = 3\eta(\frac{1}{l}\frac{dl}{dt})^2 \tag{19}$$

where η is viscosity and l is the length of the cylinder. The dissipated energy in Eq. (19) must be equal to the rate of work from the surface tension $\gamma dA/dt$, where γ is surface energy and A is the surface area. As a result, the sintering degree that is defined by the ratio of neck radius X to particle radius a, is given in Eq. (20)

$$(\frac{x}{a})^2 = \frac{4\gamma}{a\eta}t \tag{20}$$

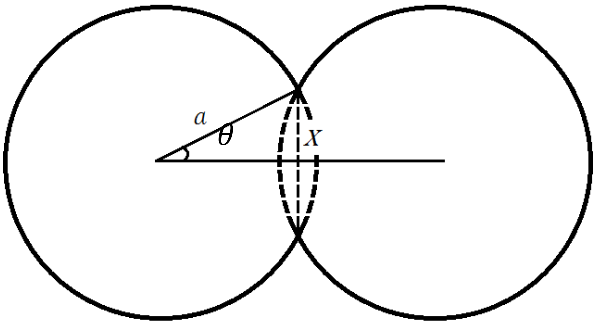

Figure 13. Frenkel's two sphere model for the initial stage of sintering. a is particle radius, X is neck radius and θ is the opening angle for the neck.

where γ is surface energy and t is time. Eq. (20) is an approximation in which the opening angle θ (Figure 13) is small, therefore its availability is limited to small neck size, where $X/a < 1/3$.

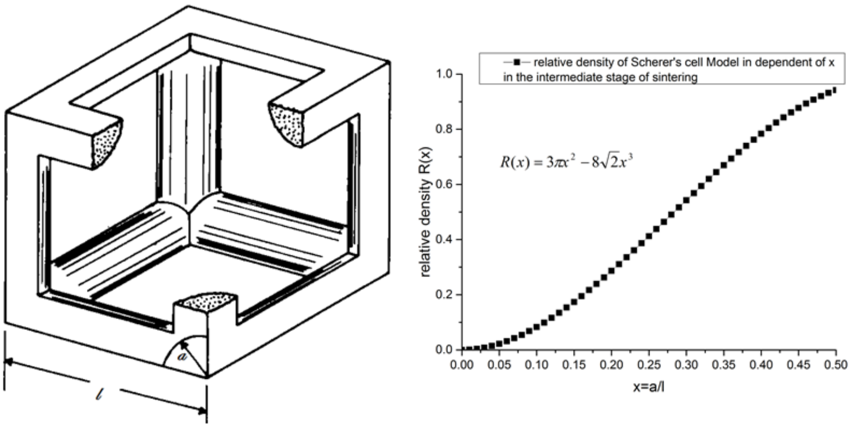

(a) (b)

Figure 14. Scherer's Cell Model (a) for the intermediate stage of sintering. l is the length of the cubic cell unit, a is the radius of cylinder representing the particle radius and x is the ratio of a/l. The relative density (b) could be determined by x [53].

For the intermediate stage, Scherer[53] has introduced unit cubic cells constructed by 12 quarter cylinders (Figure 14a) for the calculation of the dissipation energy. During sintering, the lengths l of quarter cylinders decrease while the radius an increased such that the volume of the unit cell structure remains constant. A fraction variable $x = a/l$ has been defined by Scherer; the relative density R of the unit cell structure is given as

$$R(x)=\frac{\rho}{\rho_s}=3\pi x^2-8\sqrt{2}x^3 \qquad (21)$$

where ρ is density of the compact and ρ_s is the density of the solid phase. When $x = 0.5$, which means the cylinders are getting in contact, it transfers to the final stage of sintering. The corresponding relative density according to this cell model is $R(0.5) = 93.95\ \%$. Using the same cylindrical viscous dissipation from Frenkel's Eq. (19), Scherer has deduced the evolution of $x(t)$ over time in intermediate stage of sintering.

$$\frac{dx}{dt}=\frac{\gamma}{\eta(\sqrt{\pi}d+4a)} \qquad (22)$$

where d is the pore diameter, which is possible to measure with mercury porosimeter[54, 69] and a represents the particle radius. According to Scherer, the parameter l could be obtained from Eq. (23) by equating the area of a circle with diameter d to the area of squares with length $l - 2\pi$ on the opening cross sectional area of six faces of the unit cell (Figure 14a).

$$\pi d^2 \approx (1-2a)^2 \qquad (23)$$

Since $x = a/l$, Eq. (21) and Eq. (23) can be used to determine the values of a and l with known value of d and the relative density $R(x)$. Alternatively, Eq. (21) and the Equation (8) in Reference 53 are also available to obtain x, given the relative density and the specific surface area by BET[70] measurement. Combining Eq. (21) and Eq. (22) the densification rate could be obtained,

$$\frac{1}{\rho}\frac{d\rho}{dt}=\frac{\rho_s}{\rho}\frac{dR(t)}{dt}=\frac{\gamma}{2\eta(\sqrt{\pi}d_0+2a_0)}\frac{\rho_s}{\rho^{2/3}\rho_0^{1/3}}G(x) \qquad (24)$$

$$G(x)=\frac{\partial R(x)}{\partial x}=6\pi x-24\sqrt{2}x^2 \qquad (25)$$

where ρ_0 is the initial density, d_0 and a_0 are initial the pore size and the initial particle size respectively. Although the relative density is not linearly proportional to $x(t)$ as shown in Figure 14b, its slope $G(x)$ in Eq. (24) deviates only a bit and thus could be considered as constant. Taking Eq. (24) that the densification rate is proportional to surface energy and inversely proportional to viscosity, the initial pore and particle size as well as the cube root of initial density is available. Furthermore, Scherer has also studied the effect in densification rate by different distributions of the pore size[55] and the effect of using other unit cell structures such as tetrahedral, octahedral, cubic and inverse tetrahedral unit cells[71]. The deviation found by Scherer in densification rate is relative small, given the initial pore diameter, particle size, initial density or specific surface area[71].

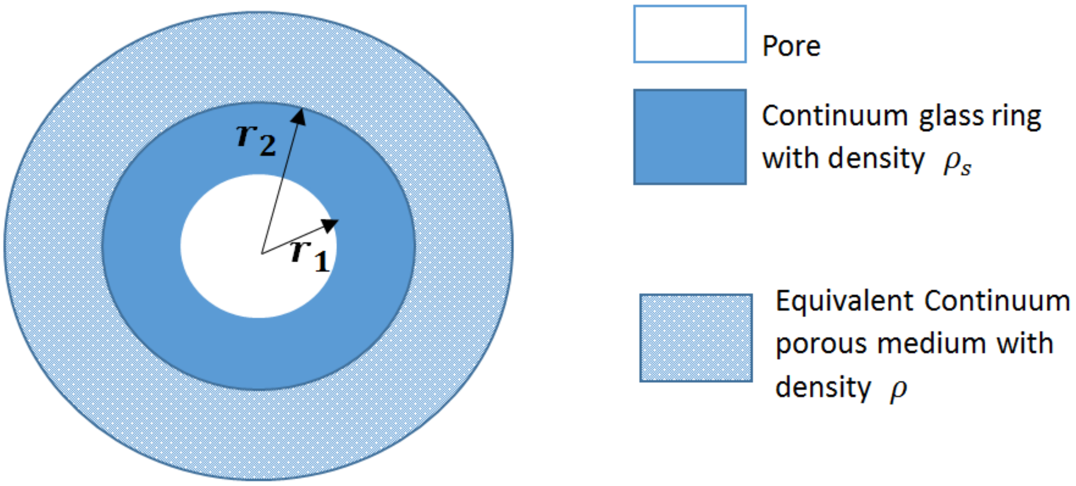

Figure 15. Spherical pore model for final stage of sintering. The radius r_2 is determined by equating the density within r_2 to the density of the powder compact. r_1 is the pore density.

$$\frac{\rho}{\rho_s}=1-\left(\frac{r_1}{r_2}\right)^3 \qquad (26)$$

In the final stage of sintering, Mackenzie and Schuttleworth[37] have assumed spherical pores surrounded by two shells (Figure 15). This model replaces the material outside r_2 with an equivalent continuum including the rest pores. When external pressure is applied, an effective pressure on the surface of r_2 shell could be equivalently calculated as a function of relative density (stress intensification factor $\phi(\rho)$ mentioned in last section). The radius r_2 is determined by such condition that the density inside the r_2 shell equals to the density of the compact outside r_2.

According to incompressible flow condition, if the radial strain rate is $d\varepsilon/dt$ in the r_2 shell, the other two perpendicular principle strain rates are $-\frac{1}{2}d\varepsilon/dt$. The rate of dissipation energy of this fluid field per unit volume is:

$$\frac{dE_d}{dt} = 3\eta(\frac{1}{l}\frac{dl}{dt})^2 \tag{27}$$

It has the same form as Eq. (19). By equating this equation to the rate of work done by surface tension, Mackenzie and Schuttleworth have derived the radial velocity of the collapsing of the r_1 shell

$$v_1 = -\frac{\gamma}{2\eta}\frac{\rho_s}{\rho} \tag{28}$$

as well as the densification rate

$$\frac{1}{\rho}\frac{d\rho}{dt} = \frac{3}{4\eta}(\frac{\rho_s}{\rho} - 1)\frac{2\gamma}{r_1} \tag{29}$$

In general, the densification rate for viscous sintering from intermediate stage to final stage could be given by Eq. (24) and Eq. (29). Assuming the pore size is proportional to the particle size in Eq. (24), a general expression of densification rate could be obtained

$$\frac{1}{\rho}\frac{d\rho}{dt} \propto \frac{\gamma(T)}{\eta(T)\alpha} \tag{30}$$

where a is particle size. Here the surface energy is assumed independent on temperature and the viscosity-temperature relation is given by the Vogel-Fulcher-Tammann Equation[72] (VFT),

$$\log_{10}\eta(T) = A + \frac{B}{T - T_c} \tag{31}$$

where *A, B* and T_0 are VFT fitting parameters. To achieve high densification rate, according to Eq. (30), using small particles or high temperature (low viscosity) accelerate the sintering rate.

2.4 Pressure-assisted sintering theory

The acceleration effect of external pressure could be obtained by modifying Eq. (29) in the final stage of sintering,

$$\frac{1}{\rho}\frac{d\rho}{dt} = \frac{3}{4\eta}(\frac{\rho_s}{\rho} - 1)(\frac{2\gamma}{r_1} + \phi(\rho)P_{ext}) \tag{32}$$

where $\phi(\rho)$ is the stress intensification factor and P_{ext} is the external pressure. The stress intensification factor relates the external pressure to the effective pressure that has been applied on the r_2 shell in Mackenzie and Schuttleworth‘s model (Figure 15). Thus, it should depend on porosity and shape of the pore (dihedral angel). For viscous sintering, it simply depends on the porosity and the pores are usually assumed spheres in the final stage of sintering. Arzt[73] and Coble[74] have proposed a relation of ϕ to the relative density

$$\phi(\rho) = \begin{cases} \dfrac{(1-\rho_0)^2}{\rho(\rho-\rho_0)^2}, & (\rho \le 0.9) \\ \dfrac{1}{\rho}, & (\rho > 0.9) \end{cases} \tag{33}$$

where ρ and ρ_0 are the relative density and initial relative density of the compact. When $\rho < 0.9$ it corresponds to the initial and intermediate stage of sintering while $\rho > 0.9$ corresponds to the end of intermediate as well as the complete final stage.

Figure 16 shows the curve of ϕ vs. ρ according to Eq. (33). One can see that at the beginning of the initial stage where the neck begins to grow the effective pressure can be thousand times higher than the applied pressure. This contributes to the small contacting area in the initial stage of sintering. Then it is approaching unity by entering the final stage and becomes unity when full densification is achieved. Most of the sintering time in pressure-assisted sintering is spent on the 8 % of density in the final stage and therefore Eq. (32) dominates. Since the driving force has been replaced by

$$\frac{2\gamma_e}{r_1} = \frac{2\gamma}{r_1} + \phi(\rho)P_{ext} \tag{34}$$

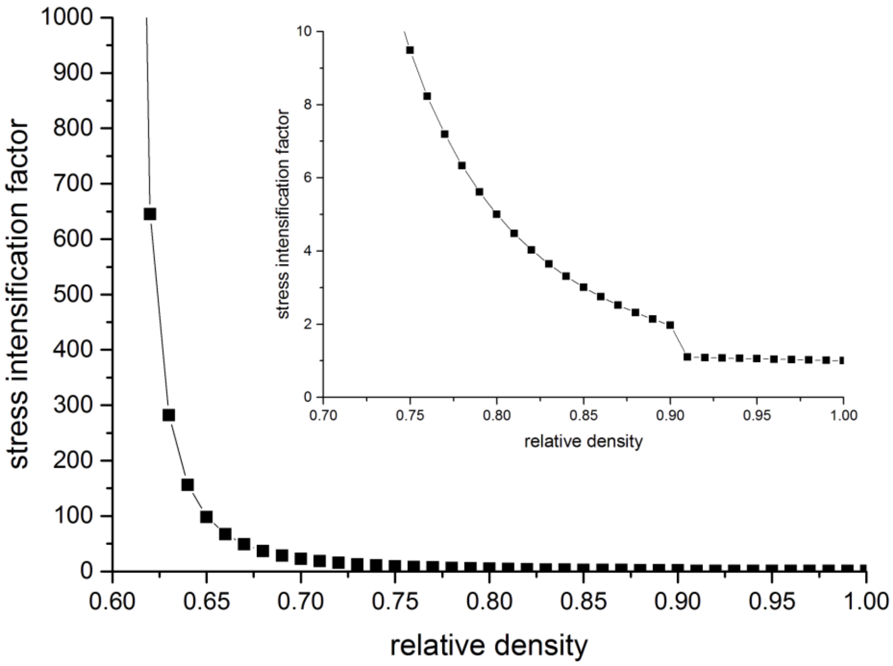

Figure 16. Approach of Stress intensification factor ϕ via relative density proposed by Arzt[73] and Coble[74] for pressure-assisted sintering. The small figure is a zoom of the large figure.

in pressure-assisted sintering, an effective surface energy can be defined

$$\gamma_e = \gamma + \frac{r_1}{2}\phi(\rho)P_{ext} \tag{35}$$

Eq.(32) then becomes

$$\frac{1}{\rho}\frac{d\rho}{dt} = \frac{3}{4\eta}(\frac{\rho_s}{\rho} - 1)\frac{2\gamma_e}{r_1} \tag{36}$$

which has the same form as Eq. (29) derived from the pressure-less sintering. By replacing surface energy γ with effective surface energy γ_e under external pressure, the densification rate (Eq. (24)) derived from intermediate stage as well as the neck growth rate (Eq. (20)) derived from the initial stage could still be applied.

2.5 Diffusion of network modifiers in glass

Glass is known for a behavior as Newtonian viscous flow[75] at elevated temperature. As seen from Table 4 and Table 5, the transport terms *M(T)* are proportional to the diffusion coefficient except for viscous sintering, which is inversely proportional to a fluid property – the viscosity. One can deduce the collective diffusion coefficient using Stokes-Einstein relation,

$$D_\eta = \frac{k_B T}{6\pi r\eta} \tag{37}$$

where D_η is the collective diffusion coefficient derived from a spherical group with radius r moving in velocity v and experience friction force $6\pi r\eta$ in viscous liquid with low Reynolds number. This diffusion coefficient could be very different from the conventional tracing diffusion coefficient. Glass has its dedicated mass transportation behavior via collective diffusion. Before going into detailed discussion, the glass should be limited to oxide glass.

The diffusion coefficient derived from viscosity is effectively the result of collective movement of basic unit structures instead of single atoms. For example, the basic unit structure in silica glass is a silica tetrahedral $SiO_{4/2}$. According to Zachariasen's random network theory[76], these tetrahedra are connected at four corners to form a 3D network in a highly disorder fashion while the same tetrahedra are linked in a high order in crystalline silicate. The high disorder in glass network is manifested in the variability in the Si-O-Si angle of adjacent tetrahedra, which ranges from 120 ° to 180 °. Additionally, two rotations are also allowed either around the point occupied by linking oxygen or along the axis occupied by the linking oxygen and silicon. Therefore, it is no longer suitable to use the concepts of point defects or boundary defects in crystals to picture the diffusion behavior in a glass network. Instead, the picture of diffusion in glass is described by the transport of particles such as cations, anions, water, impurities or gases through available interstices in the rigid glass network as shown in Figure 17.

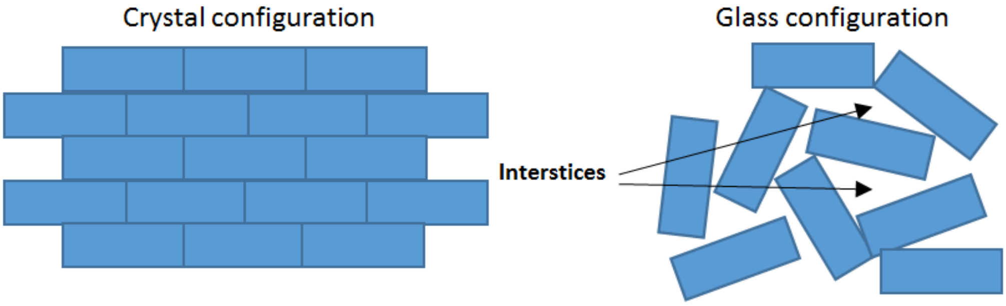

Figure 17. Schematic of interstices in the configuration of glass (right).and comparison to the highly order configuration in crystal (left) with the same unit structure.

According to Stanworth[77], the ionic bond strength is lower than that of covalent bonds, the network modifiers are the most active cations in the glass network for diffusion. Figure 18 shows results of a study of tracing isotope diffusion in both alkali silica glass and quartz. As the self-diffusion of network former Si in glass network is at

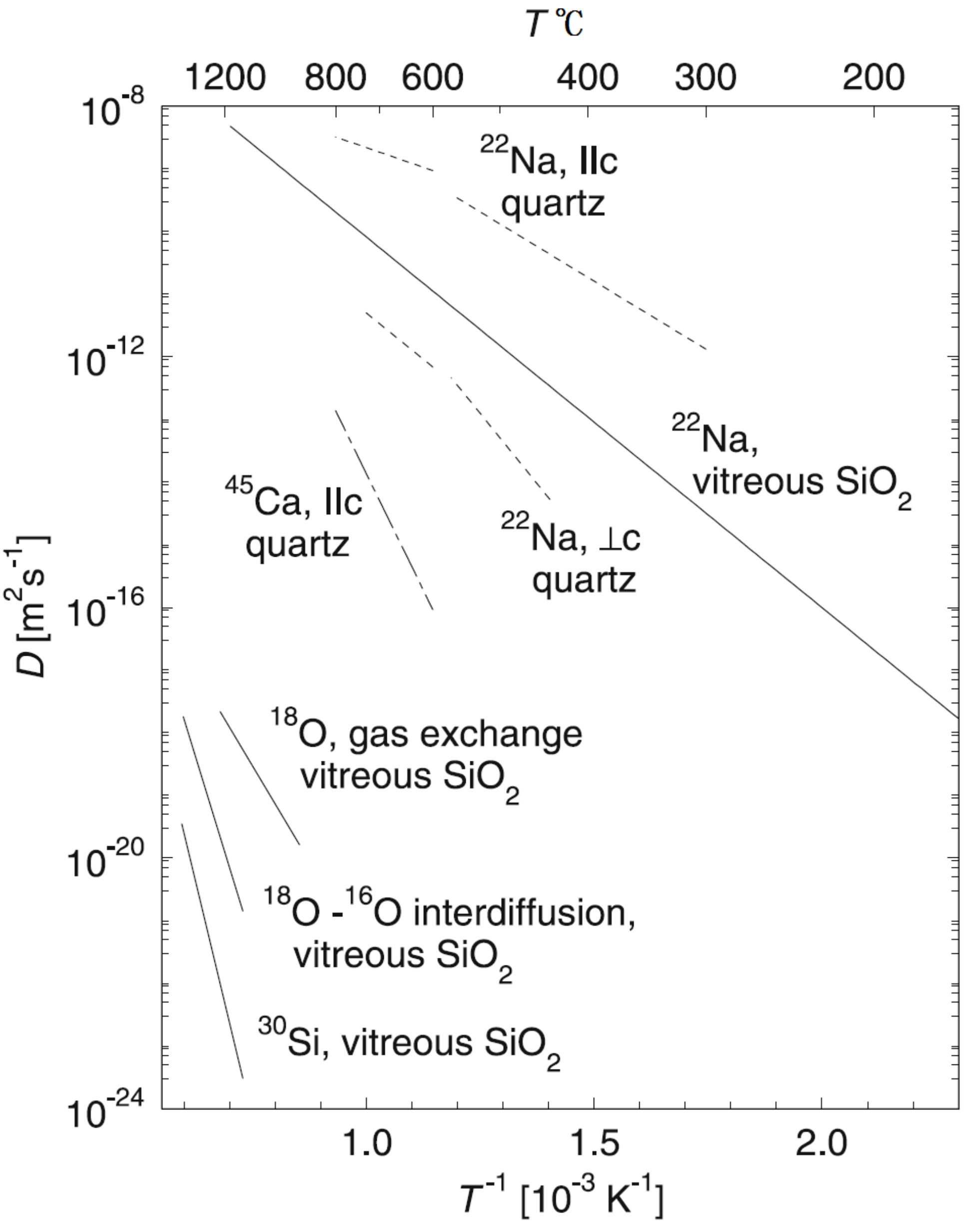

Figure 18. Diffusion coefficients of network formers and modifiers in vitreous silica and the same cation diffusion in quartz [78].

least 10 orders of magnitudes slower than the diffusion of network modifier cations Na^+ and Ca^{2+}, the glass network is considered rigid and the self-diffusion of the network former is not of interest. For this reason, most of the diffusion data presented in literature refers to diffusion of modifier cations, such as Na^+ and Ca^{2+} diffusion measured by ionic conduction experiments[78], in which the diffusion coefficient of the conducting ion, the network modifier, is related via Nernst-Einstein equation[44]. Ionic diffusion behavior in glass has been used in ion exchange, which is able to alter the near surface properties of glass, such as chemical strengthening[72], modulating refractive index[79] and electric conductivity variation.

2.6 Gas diffusion and permeation in glass

Other diffusion behaviors occurring in glass network are the gas diffusion and permeation[80]. They are related via the study of gas permeation through membrane[78]:

$$K = DS \tag{38}$$

where K is permeability, D is diffusion coefficient of gas species and S is solubility. This equation is based on the assumption in dilute solutions so that Henry's law[80] determines the concentration of gas on the surface by the product of vapor pressure and solubility $c = SP$, where P is vapor pressure of solved gas species. The diffusion of a gas molecule takes the path through interstices of glass network. As shown in Figure 19, the gas permeability decreases in the order $He > H_2 > Ne > N_2 > O_2 > Ar > Kr$. The diffusion behavior of a network modifier determines the homogeneity of the final glass (elimination of cords and striae via diffusion). On the other hand, the diffusivity, solubility and permeability of gases affect the bubble behavior in glass homogeneity.

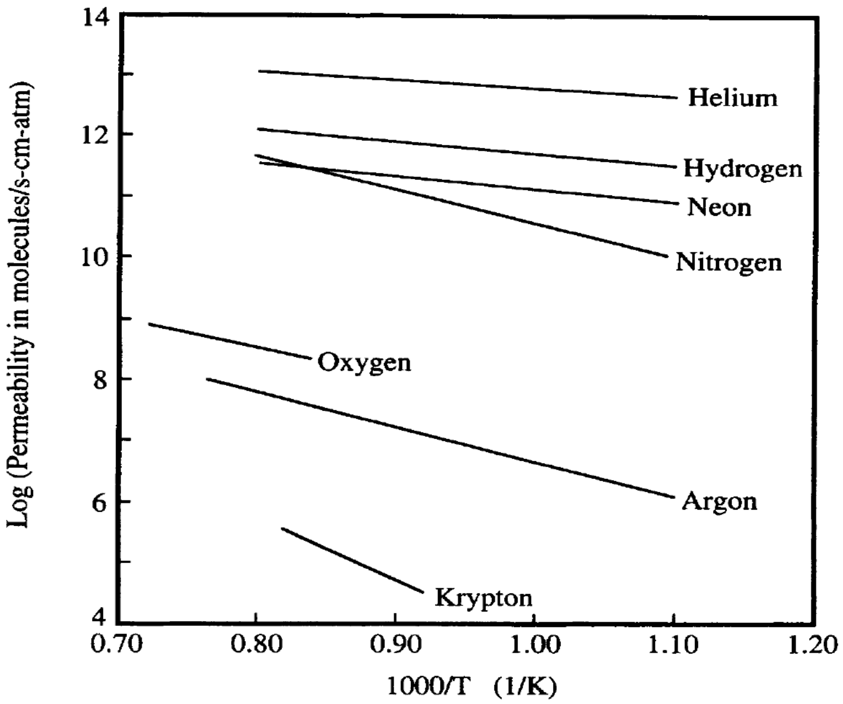

Figure 19. Permeability of different gases through vitreous silica [80].

Chapter 3 Experimental methods

3.1 Characterization methods for glass samples

3.1.1 Spectroscopy (UV/Vis/NIR)

The spectroscopy measures absorbance spectra of a medium through which an incident beam may suffer absorption and scattering losses (Luminescence is neglected for SAL glass). This spectrum covers wavelengths including ultra violet (UV), visible (VIS) and near infrared (NIR) range. In the UV range, the minimum absorbance is provided by Rayleigh scattering[81], which is inversely proportional to fourth power of wavelength. Other UV absorption can be arise from electron defects[82], such as single electron defects and oxygen deficiency in silica glass. The VIS range is usually corresponding to the exited electron state of some cations[83], such as Fe^{2+}, Fe^{3+}, Yb^{2+} e.g., which generates colored glasses. Except for absorption, scattering from particles may also contribute to the absorbance spectrum, such as Mie scattering[84].

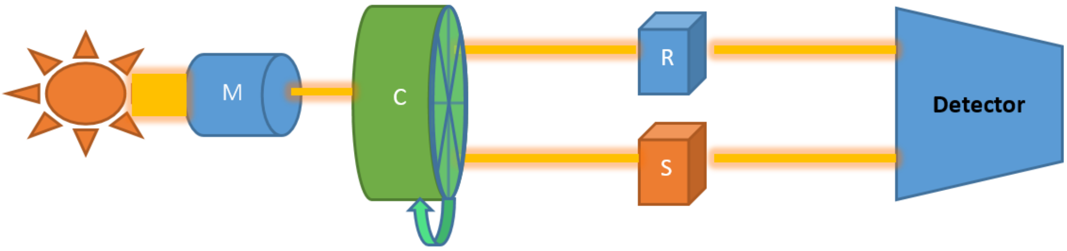

Figure 20. Schematic of absorbance spectrum setup. **M**: Monochromator, **C**: Beam chopper, **R**: reference, **S**: Sample.

Polished SAL glasses are measured using the spectrometer Lamda 900 (PerkinElmer) in the wavelength range from 200 nm to 3300 nm. The monochromatic light is separated alternatively to the reference and sample holder via a beam chopper as shown in Figure 20. The intensity is used to calculate absorbance A as given in Eq. (39)

$$A = -\log_{10}\frac{I}{I_0} \tag{39}$$

where I and I_0 are the intensity of the beam after and before passing through the medium. With the setup without anything in the reference holder, the resulting absorbance A includes actually the reflection losses. To improve this, a reference glass with the much less thickness should be placed in the reference holder. The resulting absorbance A contributes only to absorption and scattering. This measurement is carried out in Lamda 900 with wavelength steps of 0.5 nm and the integration time of 500 ms.

3.1.2 *Fourier Transform Infrared spectroscopy*

As a complementary spectrum characterization method, the Fourier Transform Infrared (FTIR) spectroscopy provides absorption spectra in the range of the middle infrared region 5000 cm^{-1} ~ 400 cm^{-1} (2 µm – 25 µm). The MIR spectrum reveals absorption groups in silica glasses[85], where the vibrational and associated vibrational-rotational modes[86] appear. Here also, 1 mm polished SAL glass slices have been prepared and measured with a Nicolet iS10 FTIR spectrometer. In our study, the FTIR spectrum is used to trace the OH groups in SAL glass.

3.1.3 *Microscopy*

The Zeiss Axioskope microscope is employed in this work with the following objectives as shown in Table 6. Despite the aberration[87] of the entire optical system, the resolution of light is given by the Abbe equation[88]:

$$d = \frac{\lambda}{2NA} \tag{40}$$

Table 6. Microscopy objective parameters

Magnification	Numeric Aperture	Camera Resolution	Eye Resolution
		µm/pixel	µm
2.5x	0.075	4.02	3,67
10x	0.2	1.04	1,38
20x	0.4	0.52	0,69
50x	0.5	0.21	0,55
100x	0.75	0.10	0,37

where λ is wavelength of the light, which is assumed to be 550 nm (green light) here, NA is the numeric aperture[89] of the objectives with air as the environment. Therefore, this microscopy provides theoretical maximum resolution of 0.37 µm using 100x objective. In other words, bubbles or defects smaller than 370 nm are not resolvable in this optical system. Except for the normal brightfield microscopy, there are two additional modes available: the darkfield microscopy and differential interference contrast (DIC) microscopy.

The darkfield microscopy illuminates light from the bottom; only scattered light is collected into the image plane. This is advantageous to observe transparent species embedded in another transparent medium by making better contrast with its surroundings. For example very fine inclusions or very small bubbles scatter are observable by darkfield microscopy. DIC microscopy is used to get information about the optical path length[89] of the sample by applying two orthogonally polarized coherent light sources and recombining them again before observation. Its contrast is proportional to the optical path length gradient in the shear direction, where normally the edge and lines are situated. A virtual 3D image is received but not physical reliable, so it needs a physical reference to distinguish the concave region from the convex region. In addition, if the thickness of the sample is homogeneous, DIC microscopy supplies the difference in refractive indices.

3.1.4 X-Ray Diffraction

The X-Ray diffraction (XRD) is one of the few methods, which are able to determine the structure of a material in the range of angstroms. It is widely used in identifying crystals with sharp scattering signals at specific diffraction angles determined by Bragg's law:

$$n\lambda = 2d\sin\theta \tag{41}$$

where n is an integer, λ is the wavelength of the incident X-ray (Cu-K_α at 0.1540562 nm and Cu-K_β at 0.1544398 nm as the source), d is the distance between two scattering centers and θ is the diffraction angle. Polished glass pieces (1 mm thick) are measured by a diffractometer PANalytical X'Pert Pro from 20 ° to 70 °(2θ), with step angle of 0.0263 °.

From the random network theory proposed by Zachariasen[90], silica glass is made of random-orientated interconnected silica tetrahedrons in random directions. Warren[91] has established a model, which has successfully interpreted the XRD diffraction pattern for silica glass, by regular-defined distribution of surrounding atoms within the range of 5.2 Å ($2\theta \approx 17$ °) and continuous distribution of surrounding atoms for those out of this range. It means that the silica tetrahedron and its nearest neighbors have no significant differences in arrangement of the crystalline form of SiO_2. The distribution of bonding lengths leads to a broadening of the signal at glasses. So the XRD data in this work will be mainly presented with 2θ larger than 20 °. By measuring the broadening of the diffraction peak in XRD data, the particle size could be also determined. The extent of broadening is given by Scherrer equation[92]:

$$d = \frac{0.9\lambda}{B\cos\theta} \tag{42}$$

where B is the broadening of the XRD diffraction peak (FWHM) in radians, d is diameter of crystal particle, λ is the wavelength of the incident X-Ray, 0.9 is the typical value for the so called shape factor and θ is the diffraction angle. With this technique, crystallization in glass could be estimated.

3.1.5 *Atomic Force Microscopy*

Atomic Force Microscopy (AFM) provides very high resolution for surface topology imaging in nanometer scale for surface (X-Y direction) and angstrom for Z-direction, which is about thousands time smaller than the optical diffraction limit as shown in Eq. (40). The AFM for topological measurement has normally two operating modes: to obtain measured variable (height) in constant intensity of control signal or to obtain the necessary intensity of control signal to maintain the same measured variable. Figure 21 shows the latter mode for topological imaging measurement by scanning X-Y at a constant relative height h between the sample surface and the sensing tip The sensing tip is connected to a cantilever, which acts as a detector for the change of height. After scanning the sample surface line by line, the whole topological AFM image is constructed. Tiny bumps or pores can be observed and distinguished physically in the AFM images for just tens of nanometers difference in height.

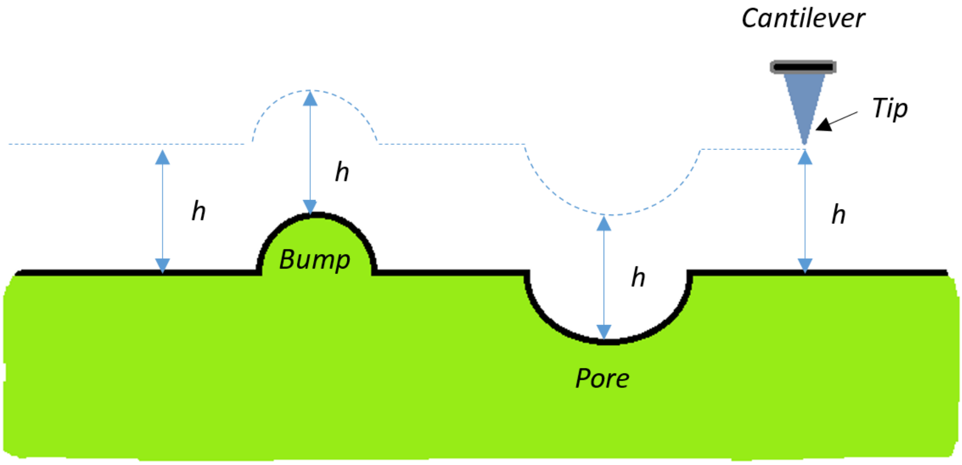

Figure 21. Schematic of AFM setup for topological surface scanning. h is the relative height from the tip to the sample surface.

3.1.6 Electron Microscopy

Electron microscopy utilizes a focused and accelerated electron beam (0.2 – 40 kV) to bombard the surface of a sample, ejecting primarily the secondary electrons (SE, < 50 eV), backscattered electrons (BSE, with the energy roughly corresponds to the incident electrons) and the characteristic X-Ray from the inner electrons. The electron microscopy device used in our work is JEOL JSM-6300F.

The secondary electrons (SE) are created, if the electrons due to the inelastic interaction between the incident beam and the outer electrons of the specimen near the surface are collected. The SE image can provide even higher resolution reaching 3 nm at 15 keV. The magnitude of the signal of SE depends mainly on the angle between the incident beam and the specimen. Besides, those collectable secondary electrons are locating on several nanometers from the surface, so the SEM is employed for high-resolution surface topography. The resolution of this SEM reaches 3 nm at 15 keV.

The backscattered electrons (BSE) arise from the elastic scattering of the incident beam on the nucleus, in which the scattering angle is strongly depending on the atomic number of the element as well as its electron numbers. Therefore, the information of the element can be deduced in a deeper layer from the surface (about several micrometers). Together with the SE image, the surface topography and the corresponding concentration are available.

The characteristic X-ray radiation is a signal resulting from the interaction of the incident beam and the inner electrons. If the incident beam has ejected an inner electron, a vacancy is generated. After some relaxation time, an outer electron will fill in the vacancy and emits an X-ray photon of characteristic energy according to the energy difference of the participating subsells. By detecting the energy of these emitted X-ray radiation via X-ray spectrometry (Bruker XFlash 5010), the emitting element can be identified. The collecting time is about 500 seconds. Depending on its working modes, the method provides minimum sensitivity of about 0.1 wt% for energy dispersive X-ray (EDX) spectroscopy and 0.01 wt% for the wavelength dispersive X-ray (WDX) spectroscopy.

3.1.7 Differential Thermal Analysis

Differential thermal analysis (DTA) is used to obtain information about phase changes in the sample material. Both the SAL glass powder as well as the inert reference material, Al_2O_3 powder in our case, are heated up at 5 K/min in the same temperature program reaching about 1300°C in the different furnace chambers. The difference in temperature is recorded. Since the reference powder is inert, if the SAL glass powder undergoes endothermic phase transitions, such as glass transition, melting, sublimation or endothermic chemical reactions, its temperature will be “delayed” as compared to the temperature of the reference powder. On the other hand, the temperature of the SAL glass powder will increase faster in the heating cycle if exothermic phase transition occurs, such as crystallization or exothermic chemical reactions.

With such thermoanalytical technique, the temperature for degassing and cleaning the glassy powder without any significant change of the phase can be determined. Furthermore, the glass transition temperature as well as the crystallization temperatures may also be found. It is also useful to determine the temperature for the first stage of GPWS, which will be introduced in the following section. The investigations were carried out in Netzsch STA 409C with about 100 mg of glass powders at a heating rate of 10 K/min to about 1400 °C. According to the instrument setup, the exothermic process has peaks downwards to the negative while the endothermic process has peaks upwards.

3.2 Sample preparation for GPWS

Glassy powders are obtained from milling the fritted SAL glass (Figure 22) and sinter it in GPWS. As for the sample preparation for GPWS, it takes two steps: the green body formation and the GPWS sintering.

3.2.1 Green body formation

Green body formation is a process to pack loose glass powders into a temporally solidified compact via heat treatment slightly above glass transition temperature (T_g) or under external high pressure at room temperature (in GPa level). The green body formation helps to achieve a higher initial density and increase the necking rate in the initial stage of sintering.

The SAL glass melt is prepared by conventional melting-and-quenching technology[93]. A mixture of 400 g crystalline powders: SiO_2 (99.8 mol%, Bremthaler Quartzmehl A1), $Al(OH)_3$ (CHP 340) and La_2O_3 (99.999 mol% Auer Remy) has been used to prepare SAL glass and Yb_2O_3 (99.999 mol% Auer Remy) for Yb doped SAL glass. They were melted at the temperature of 1650 °C for 3 hours in Pt covered crucible

Figure 22 Left: Glass melting in Pt crucible, Right: Fritted glass beans after dried from water [93].

with Pt cover (Figure 22 left). The melt is then cast directly into water, forming various sizes (mm range) of fritted glass (obtained by casting glass melt into water) beans (Figure 22 right). These glass beans are then milled in a ball-milling machine with rotation speed of 300 U/min for 5 minutes repeating 5 times. The glass powder is then sifting with 200 µm filter and 100 µm filter in succession. Those powders remaining on the top of the 200 µm filter will be sent back to the ball mill and the milling and sifting process has been repeated until all the glass powder is below 200 µm. As a result, glass powders with two different ranges are obtained in serials of 0 - 100 µm and 100 – 200 µm in diameter, respectively. The particle sizes are mainly distributed at 45µm and 105

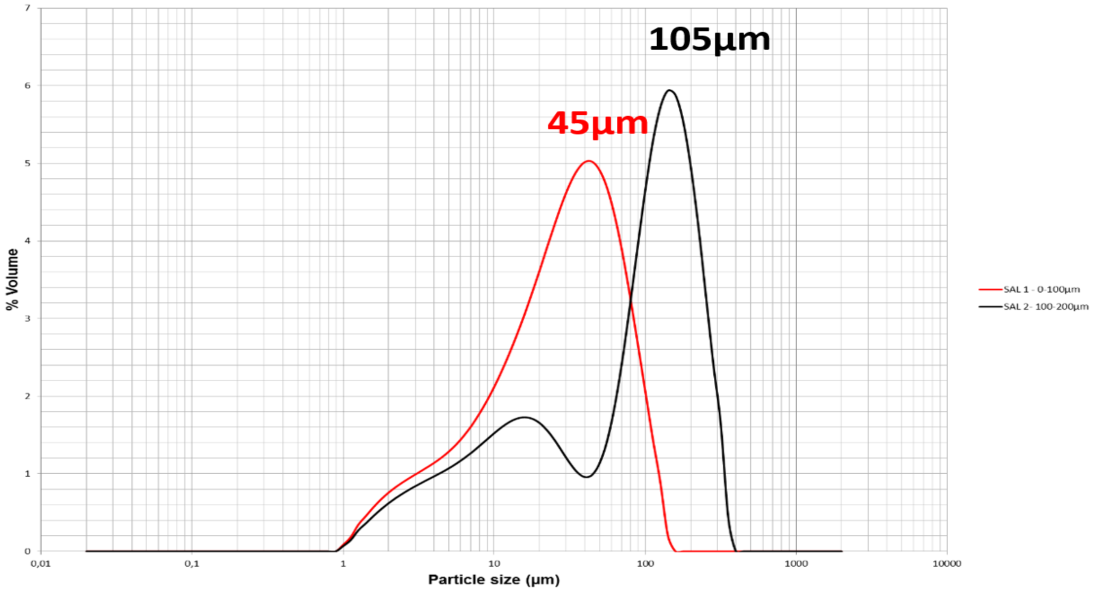

Figure 23. Size distribution of glass powder by laser scattering analyze. Measured by Dr. Gaëlle Delaizir 'SPCTS laboratory France.

µm, respectively according to the size distribution measurement (Figure 23) by laser scattering analyze (Mastersizer 2000 Malvern). The 0 - 100 µm powders has been used to achieve a higher densification rate in sintering according to sintering theory. Figure 24 shows the SE image of the milled glassy powder which are mostly of 45 µm in

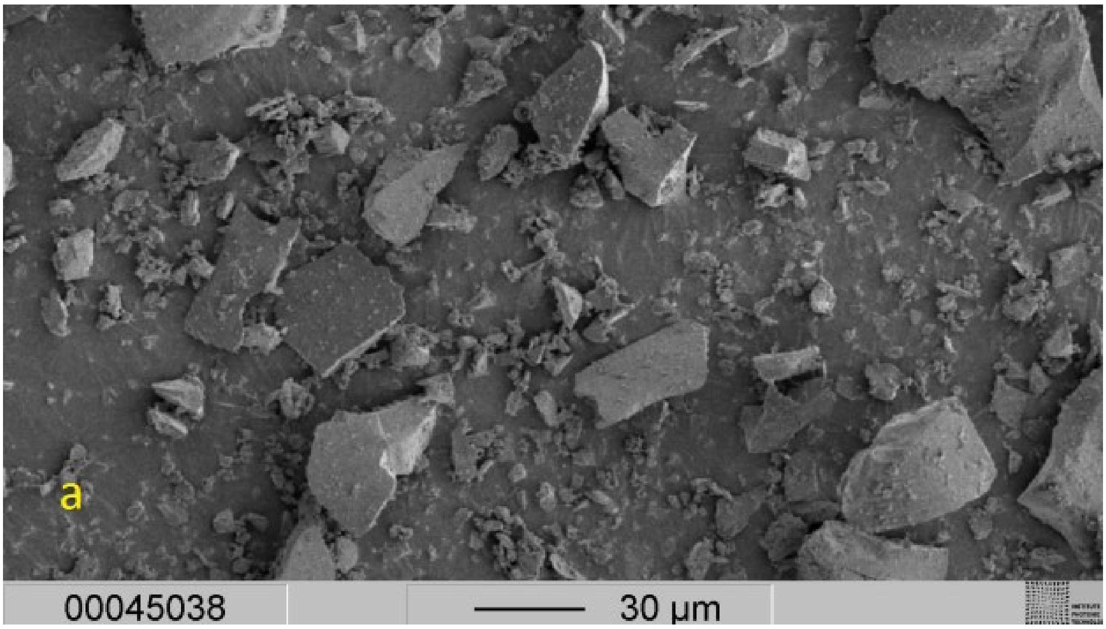

Figure 24. SE image of milled SAL glass powder after sieved by 100 µm sieve.

diameter as well as some of few micrometers. These starting glass powders (Figure 25a) are then filled in silica glass tubes, a subsequent temperature treatment at 950 °C for 1 hour in air followed. The final cylindrical compact with a diameter of 13mm (Figure 25b) was formed as green body, which is then cut into 1 mm height pieces before sent to the gas sintering furnace in a glassy carbon crucible (Figure 25c).

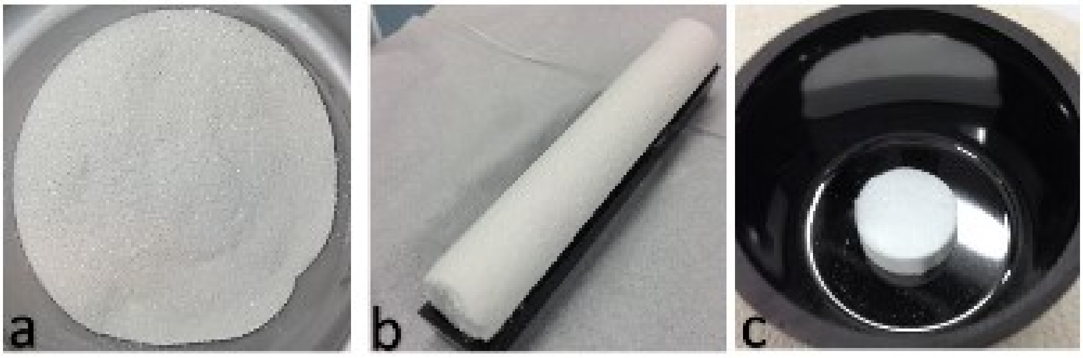

Figure 25. a) Milled and filtered SAL glass powder b) SAL green body formed in a silica glass tube. c) SAL green body in glassycarbon crucible for GPWS.

3.2.2 GPWS procedure

The GPWS process has been designed with three stages: P1, P2 and P3 as shown in Figure 26, beginning with a vacuum stage (P1) for degassing and reducing the environmental pressure. Before it turns to the second stage for application of external gas pressure, the pores are required to be isolated. Therefore, sufficient time will be taken in this stage before going to the next stage. According to the DTA result as shown in Figure 27, 1000 °C is suitable because the endotherm softening process begins slowly. Therefore, 1000 °C is used for such a long time treatment in the P1 stage. In addition, 800 °C is also chosen for the cleaning process before GPWS begins due to the fact that no obvious endothermal or exothermal process occur. This pre-cleaning procedure will be introduced later. In the second stage (P2) of GPWS, the pressure is applied with the temperature is increased as well. The heating rate is 20 K/min while the pressure rate is

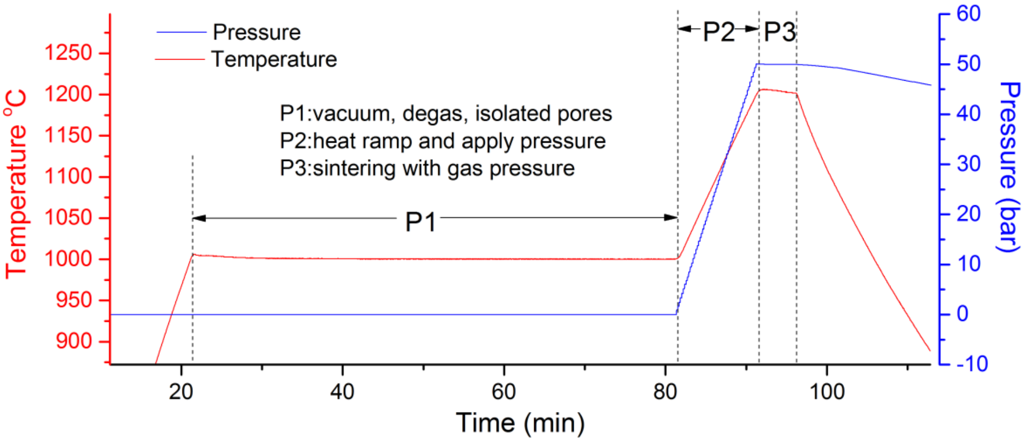

Figure 26. Typical stages of temperature and pressure in GPWS.

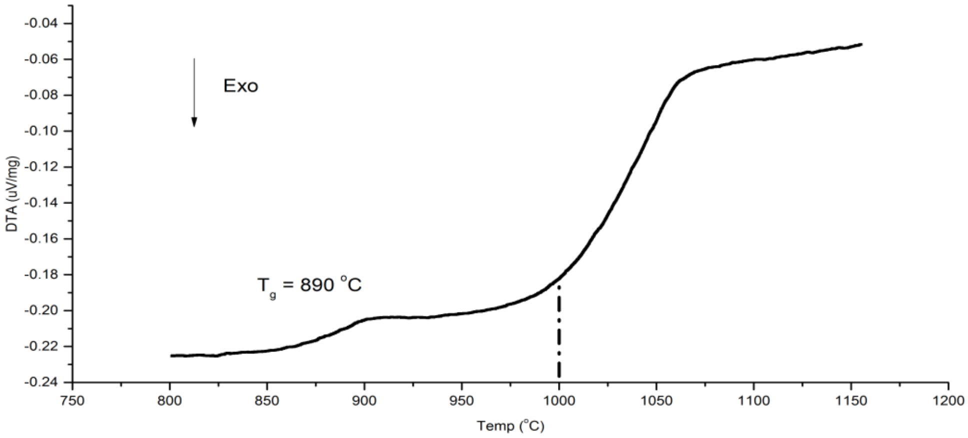

Figure 27. DTA measurement of SAL glass powder.

set to according to the temperature rate. The third stage (P3) is the working stage at the desired temperature and pressure. The dwelling time, temperature and pressure mentioned in this work are referring to this stage.

Furthermore, before the first stage of GPWS is started, the GPS furnace utilizes a vacuum program with green-body at room temperature for 6 hours in order to evacuate the adsorbed gases such as air and surface water. After that, a further vacuum process is set at 800 °C for another 6 hours. Figure 28 demonstrates the green body tablet in different stages of sintering. For the cleaning and the initial stage of sintering, the SAL glass maintains the form of a green body as in Figure 28a. After the end of the first stage of GPWS, which is corresponding to the end of intermediate stage of sintering, the SAL glass tablet has a smooth and closed surface as shown in Figure 28b. In Figure 28c, the sintered SAL glass is shown and its cut and polished slice with 1mm thickness is shown in Figure 28d, which is used for characterization of inhomogeneity.

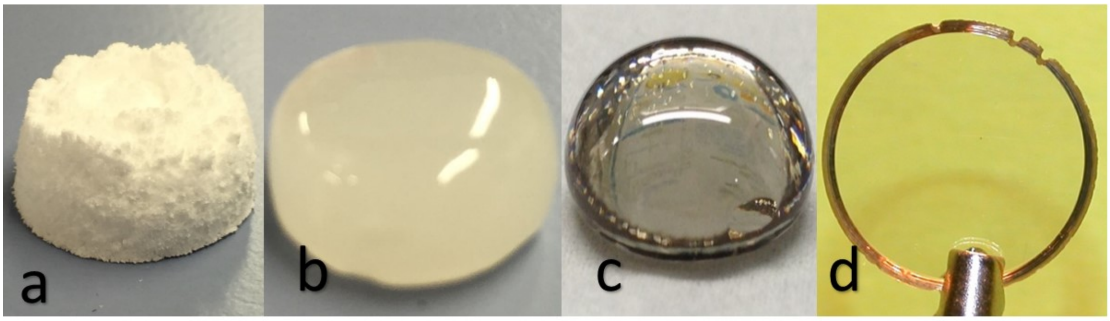

Figure 28. a) SAL green body in the initial stage of sintering. b) SAL green body in the intermediate stage of sintering. c) Glass droplet after GPWS. d) 1 mm thick SAL slice cut and polished from the GPWS SAL glass.

Chapter 4 Foundation of FEM models

Analytical theories introduced in Chapter 2 are very helpful to understand the mechanisms of the viscous behavior of glass at high temperature under external pressure. The densification rate of some examples with ideal geometries, such as spherical particles, tetrakaidecahedron grains or cubic hollow cells were given by the analytical models. However, for practical cases with non-ideal geometries, numerical simulations are necessary in order to compare to the experimental results. Here we have built three FEM models which provide good comparisons to the experimental results. With these results, the magnitude of some parameters, such as viscosity, surface tension, diffusion coefficient and the temperature fluctuation in the furnace have been estimated.

4.1 FEM model for diffusion and convection

This model has been used to simulate the mass transportation of Al and La groups in the GPWS SAL glasses. It helps to understand the formation of striae and to estimate the diffusion coefficient and viscosity of glass at high temperature according to the experimental results. According to the theory of diffusion in glass (chapter 2.7), the Al^{3+} groups and La^{3+} groups are considered as diffusers in the silica glass network in the form of collective motions, which means single or several units of Al tetrahedra or La octahedra diffuse in group. Such a transport behavior is described by the convection-diffusion equation with constant diffusion coefficient, without sources or sinks and the flow is incompressible:

$$\frac{\partial c}{\partial t} = D\nabla^2 c - \boldsymbol{v} \cdot \nabla c \tag{43}$$

where c is the concentration of the species (Al or La groups), D is diffusion coefficient and $\boldsymbol{v}$ is the velocity field of the flow. Eq. (39) is a mass conservation equation that has applied Fick's law, which is adequate for dilute solvent. La_2O_3 can be considered dilute since its concentration is 10 mol%. Al_2O_3 has higher concentration of 20 mol%; however, its influence on refractive index is only one third of that from La_2O_3. Therefore, it is still acceptable if only refractive index will be concerned. The working furnace is able to maintain a temperature difference of ±10 K at 1400 °C in the chamber, so the diffusion coefficient can be taken as constant in this case. The velocity of the glass flow is calculated using incompressible Navior-Stokes equation[94]

$$\rho(T)\frac{\partial \boldsymbol{v}}{\partial t}+\rho(T)\cdot(\boldsymbol{v}\cdot\nabla)\boldsymbol{v}=\nabla\cdot(-p\boldsymbol{I}+\eta(\nabla\boldsymbol{v}+(\nabla\boldsymbol{v})^{T}))+\boldsymbol{F} \tag{44}$$

where $\rho(T)$ is temperature dependent density of the glass melt, T is temperature, p is the external pressure, $\boldsymbol{I}$ is unit matrix, η is viscosity and $\boldsymbol{F}$ is the volume force. This is an equation for momentum conservation of the fluid. The convective flow is driven by the perturbation of density due to temperature inhomogeneity under gravity field. In other words, the fluid parcel with higher temperature maintains a lower density, which flows up while the cooler parcel flows down, as its density is higher. The density of the glass is given by

$$\rho(T)=\frac{\rho_0}{1+\alpha_V(T-T_{ref})} \tag{45}$$

where α_v is the volume expansion coefficient, T_{ref} is reference temperature and ρ_0 is the density at reference temperature. In order to generate convections, a temperature field with initially 10 K higher at the bottom of the sample was set (according to the manufacture). Equation for heat transfer in fluids[95] is applied

$$\rho(T)C_p\frac{\partial T}{\partial t}+\rho(T)C_p\boldsymbol{v}\cdot\nabla T+\nabla\cdot\boldsymbol{q}=q_0 \tag{46}$$

Here C_{p} is heat capacity at constant pressure, $\boldsymbol{q}$ is heat flux and q_0 is the source term, which is 0 here. Since the temperature field is only for generating a perturbation of 10 K in the glass melt, so the absolute value of heat capacity and heat conductivity are not necessary to be accurate. Typical values of aluminosilicate glasses are used in the simulation for the heat transfer module.

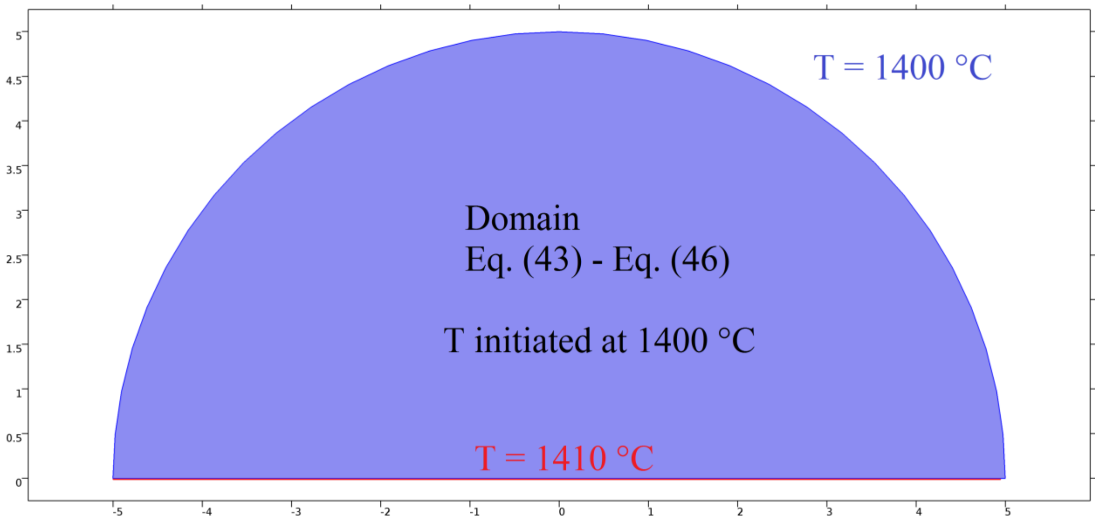

Figure 29. Schema of the simulationo domain of SAL glass droplet at 1400 °C. The unit for the axis is mm.

The equations from (39) to (42) are applied in the domain of a glass droplet in a 2D surface in COMSOL[96] Multiphysics® as demonstrated in Figure 29. The initial temperature of the glass melt is 1400 °C while the bottom temperature is kept 1410 °C. The temperature of the external environment is also kept 1400 °C. The refractive index will be calculated from the concentration of La_2O_3 and Al_2O_3 according to reference 21. As to compare to the experimental results, the norm of gradient of refractive index will also be calculated. This is used to interpret the striae we see through the glasses. It is based on the assumption that the eyes are sensitive to gradient of the refractive index. Table 7 has listed all the parameters used in the simulation at 1400 °C. The linear thermal expansion coefficient at 1400 °C to 1750 °C is $11.5\times10^{-6}\ K^{-1}$ which is obtained from a similar SAL glass composition in reference 102. Such linear thermal expansion coefficient corresponds to a volume expansion coefficient of about $34.5\times10^{-6}\ K^{-1}$, which is the value used in the variation in density.

Table 7. Parameters set to the simulation model at 1400 °C.

physical quantity	variable	value	unit	notice
Density at reference temperature	ρ_0	3171	$kg{\cdot}m^{-3}$	
Reference temperature	T_{ref}	1300	K	
Volume expansion coefficient	α_v	34.5×10^{-6}	K^{-1}	Ref. 102
Diffusion coefficient of Al^{3+} specie	D_{Al}	5.5×10^{-12}	m^2/s	Estimated from FEM
Diffusion coefficient of La^{3+} specie	D_{La}	4.0×10^{-12}	m^2/s	Estimated from FEM
Viscosity	η	0.2	Pa·s	Estimated from FEM
Thermal conductivity	k	1.3	$W{\cdot}m^{-1}K^{-1}$	General[97]
Heat capacity at constant pressure	C_p	800	$J{\cdot}kg^{-1}K^{-1}$	General[98]

The WDX scanning data from a low temperature sintered GPWS SAL glass sample (HIP11/1100 °C/50 bar/30 min) were taken as the initial concentrations in this model, which are 19.865 mol% Al_2O_3 (mean) with a standard deviation of 0.142 mol% and 9.441 mol% La_2O_3 (mean) with a standard deviation of 0.281 mol%, respectively. These values are doubled as initial values in the FEM calculations since the Al^{3+} and La^{3+} are assumed as diffusers.

4.2 FEM model for viscous deformation

Another important parameter for sintering is the surface tension at high temperature, which is proportional to the driven force of the sintering process. Another FEM model has been developed by using only Eq. (44) for the determination of surface tension under fluid flow. This model utilizes the fluid field equations to describe the deformation of glass domain under gravity as body force. The surface tension has been set on the glass/gas boundaries and the force balances have been kept. It depicts a glass droplet deformation under its own weight and the geometry of the glass/gas boundary is determined by the surface tension after long enough time. Since the viscosity at high temperature is low (0.2 Pas at 1400 °C), it takes a few seconds before the geometry achieves equilibrium. The practical dwelling times are within several minutes, so they are much more than sufficient. By manually limiting the variation of bottom diameter, the glass droplet can always come to its equilibrium geometry shape very fast. In this case, the initial geometry of the glass is not important anymore, only the total volume of the glass droplet matters. Hence, the initial condition for this model has been set to a cylinder with diameter equaled to the bottom diameter of the experimental glass droplet and its height is determined by the volume conservation (Figure 30).

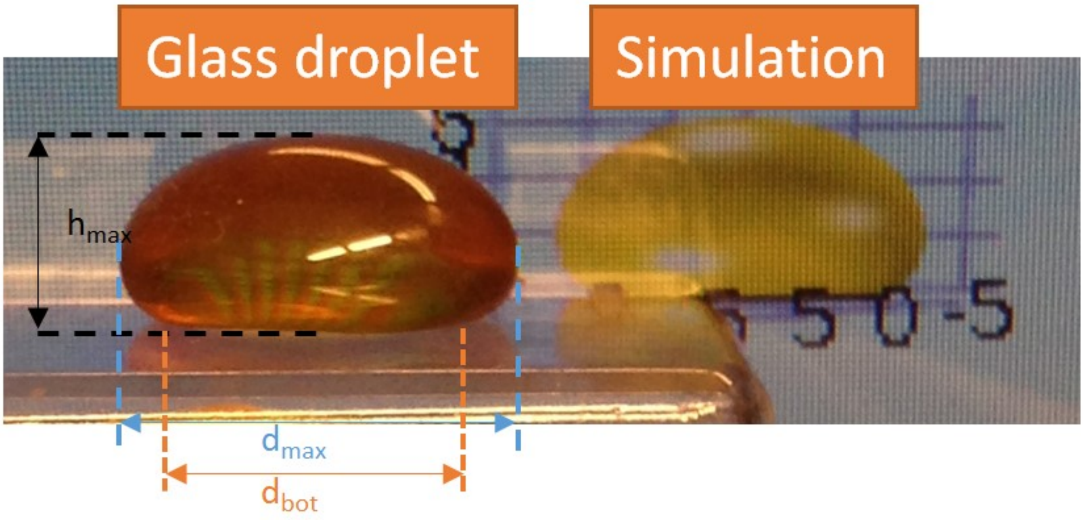

Figure 30. Comparison of experimental glass droplet after sintering and the FEM simulation results. The bottom diameter d_{bot} has been used as the diameter of the initial cylinder in the model. The maximum height h_{max} and the maximum diameter d_{max} will be compared to determine the surface tension.

4.3 FEM model for inhomogeneous bubble compression

This model is similar to the last one, using also the fluid filed equation from (44). The only difference is the inhomogeneous viscosity distribution. Homogeneous hydraulic pressures were assumed inside the bubble and outside the glass region. The surrounding glass is assumed as incompressible flow with inhomogeneous viscosity as shown in Figure 31. The viscosity varies in different regions at different angles. The external pressure is set constant at 50 bar while the bubble pressure is set constant at 1 bar. Initially, perfect spheres are formed both for the outer and inner surfaces. A viscosity

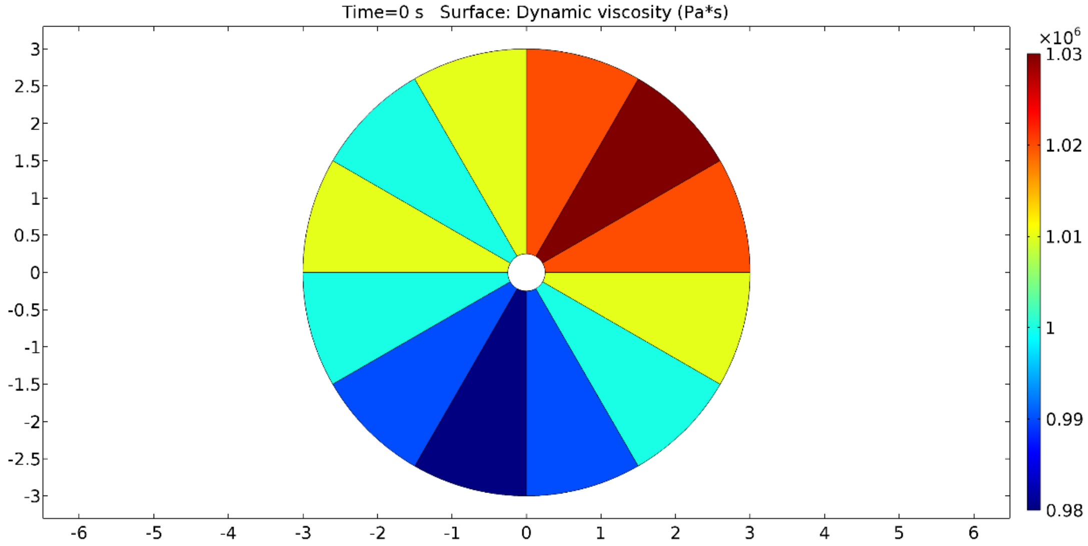

Figure 31. Bubble compression model with inhomogenous viscosity regions. The external pressure is set to 50 bar while the inner pressure in the bubble is set to be 1 bar. The color bar on the right hand side represents the viscosity at Pas.

variation of from 0.3 % to 30 % was added to a mean viscosity of 10^6 Pas. Figure 31 shows the case with 3% variation in viscosity. The calculation times were set to 0.6 s and 0.9 s, which result in the same diameters as observed in the bubble compression experiments with 50 bar and 100 bar, respectively. This was used to achieve comparable sizes of bubbles to the experiment without the necessity to be precise in viscosity because viscosity governs the time it takes to achieve “equilibrium” geometry.

Chapter 5 Determination of working parameters

This chapter first finds out the viscosity, surface tension and diffusion coefficients and then applies them to determine the range of working parameters, such as temperatures, pressures and dwelling times. It is carried out using the analytical models from pressure-assisted viscous sintering theory introduced in chapter 2.

5.1 Determination of viscosity

According to the viscous sintering theory in chapter 2, the sintering behavior (with or without pressure) such as necking rate in the initial stage, the densification rate in the intermediate and final stage as well as the compression of bubbles in the very final stage, are strongly influenced by viscosity. In order to find out suitable experimental parameters for temperature, pressure and particle sizes, the determination of viscosity for SAL glass is of significant importance.

We have here[99] developed a method for viscosity measurement in tube furnace and denominated it the Viscous Stretching Method (VSM).This method determines viscosity-temperature profile via analyzing the after stretched diameter profile, given that the temperature distribution and the load are known. The rate of stretching is constant. This is demonstrated in Figure 32. The tensile stress can be related to the rate of stretching with viscosity as the coefficient in the form of Eq. (47)[100].

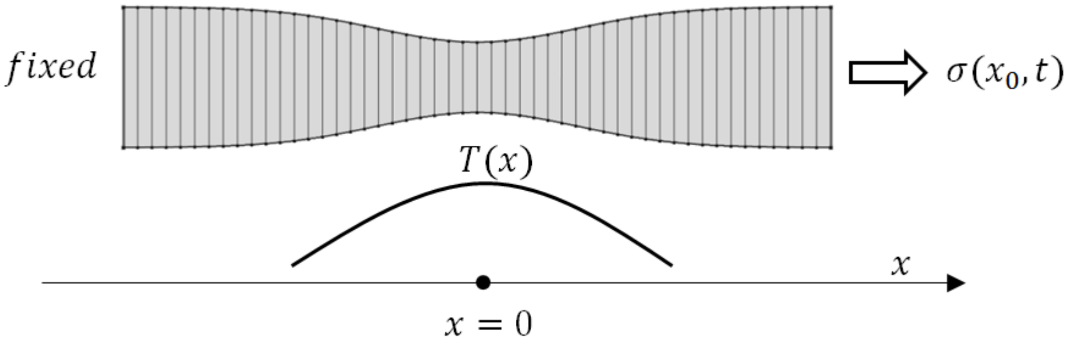

Figure 32. Schema of glass rod stretched from one side at normal temperature distribution T(x). σ is the stress of load.

$$\sigma(t) = 3\eta(T(x,t))\frac{d\varepsilon(x,t)}{dt} \tag{47}$$

where ε is strain, σ is stress, η is viscosity, x is axial position and T is temperature. Based on the Newtonian flow condition, viscosity is only a function of temperature, which is assumed to be homogeneously distributed in each cross section but differently distributed in the axial positions. For incompressible flow, the stress and strain are defined as

$$\sigma(x,t) = \frac{F(x,t)}{A(x,t)} \tag{48}$$

$$\frac{d\varepsilon(x,t)}{dt} = -\frac{1}{A(x,t)}\frac{dA(x,t)}{dt} \tag{49}$$

where F is the load of stretching and A is the cross sectional area. It is assumed that the acceleration of stretching is so slow, the force applied on the ends of the rod are basically balanced. Thus, the load applied on each section is the same, which means *F(x,t)* can be simplified to *F(t)* in Eq.(48). Substituting Eq. (48) and (49) into (47), we obtain

$$\frac{dA(x,t)}{dt} = \frac{-F(t)}{3\eta(T(x,t))} \tag{50}$$

Subsequently, stretching a cylinder with diameter from A_0 at time 0 to *A(x,t)* at time t, Eq. (51)*(*19*)* can be obtained by integrating Eq. (50)

$$A_0 - A(x,t) = \int_0^t \frac{F(t)}{3\eta(T(x,t))} \tag{51}$$

The integration on the right-hand side is complex. If the temperature encountered by each axial section within a period of time t is almost constant – in other words, if the temperature is only a function of position, *T(x,t)* can be further simplified

$$T(x,t) \approx T(x) \tag{52}$$

Eq. (52) is a good approximation if the stretched length is small compared to the gage section or if the temperature fluctuates so slightly in the axial direction that the corresponding variation in viscosity is negligible. With this approximation, viscosity is no longer time dependent and, therefore, Eq. (51) can be reduced to

$$A_0 - A(x,t) = \frac{M}{3\eta(T(x))} \tag{53}$$

where $M = \int_0^t F(t)dt$ is the integration of load force F over time, which can be obtained

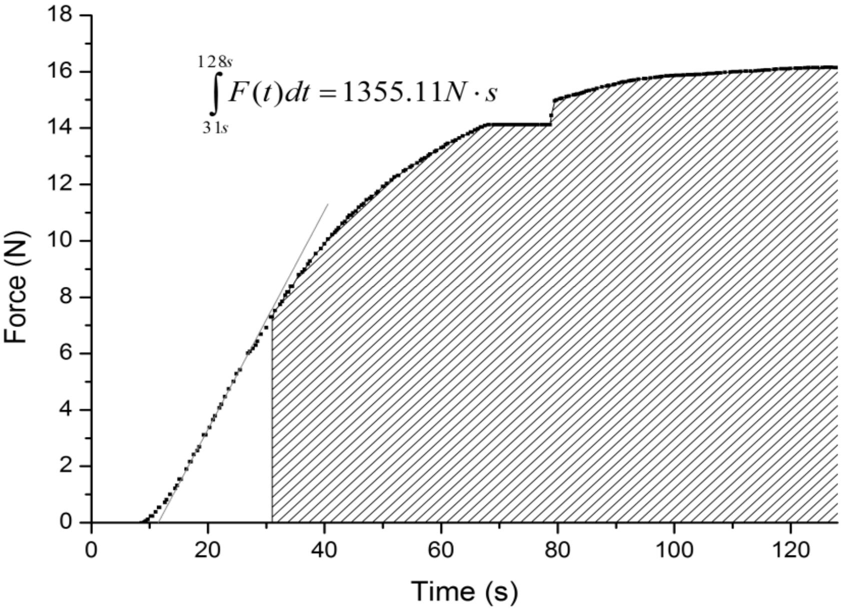

Figure 33. Load-time curve and its integration over the plastic strain area (shaded area) at 1400 °C at 1 mm/min. The bright area under the curve attributes to the elastic contribution at the initial stage of stretching.

experimentally. Figure 33 demonstrates one example of load-time curve obtained in stretching of a silica glass rod at 1400 °C at 1 mm/min. The detailed experimental setup

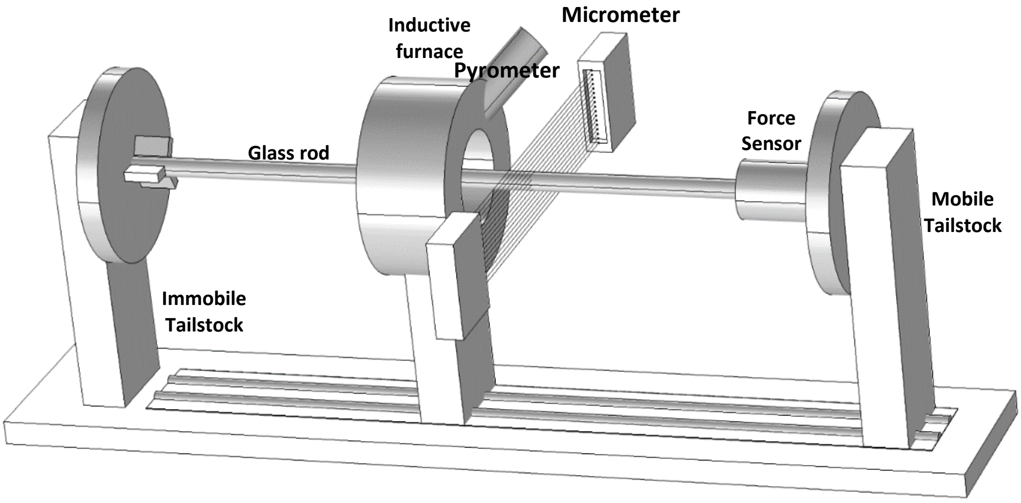

Figure 34. Schematic of the experimental setup for demonstration of the rod stretching method for temperature profile measurement.

is shown in Figure 34. The glass rod is stretched through an inductive furnace via a mobile tailstock with a force sensor connected in between. The Pyrometer and diameter measured by a micrometer. Therefore, viscosity profile can be obtained by

$$\eta(x) = \frac{M}{3(A_0 - A(x,t))} \tag{54}$$

However, not all the viscosity values obtained at the full x range are reliable due to the low precision in measurement of diameter changes at low temperature regions. The space resolution of the evaluated viscosity is limited by the assumption Eq. (52), which will decrease with stretched length. The relation of stretched and initial position can be derived using volume conservation[99]. Therefore, the space resolution is dependent on the position. Figure 35 demonstrates two curves of space resolution in different modes of furnace setup: fixed furnace and moving furnace at half of the stretching rate. In our case, the center of the furnace is of most interest; hence, a moving furnace setup will be beneficial. Except that, the stretched axial positions must be mapped back to the

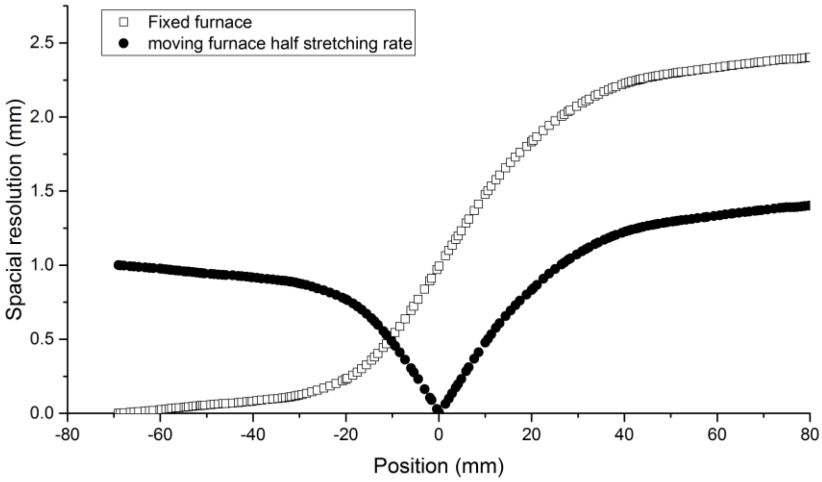

Figure 35. Spatial resolution of viscous stretching measurement at 1400°C with fixed furnace setup and moving furnace setup (half the stretching rate).

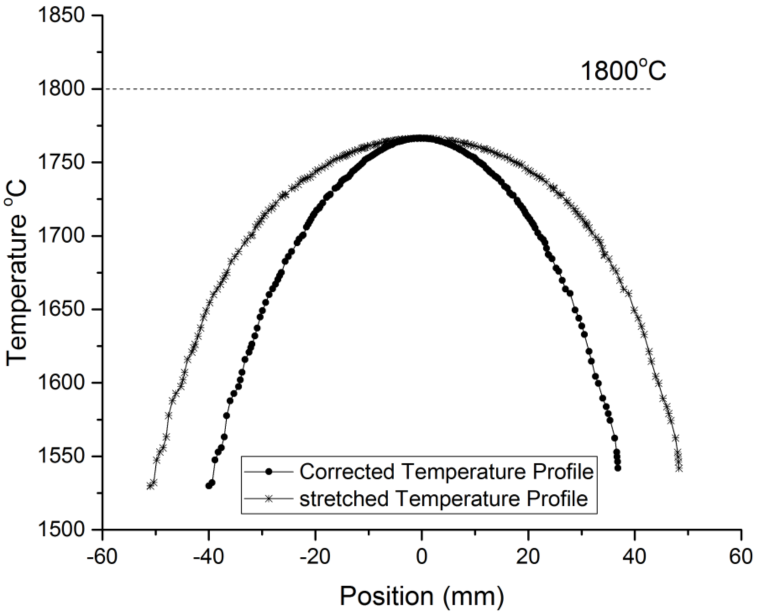

Figure 36. Temperature profile measured via the viscous stretching method using a 9 mm silica glass rod at 1800°C for the inductive tube furnace.

initial positions before the calculation of diameter change in data processing. Figure 36 demonstrates one example of measuring stretched and corrected temperature profiles of furnace with silica glass rods whose viscosity-temperature relationship is already known. This measurement is equivalent to viscosity measurement according to Eq. (53) in VFT form.

The lower range viscosity values (<1000 Pas) corresponding to high temperature range have been estimated via simulation of the homogenization process of Al_2O_3 and La_2O_3 concentrations. Consequently, the simulation results will be validated and

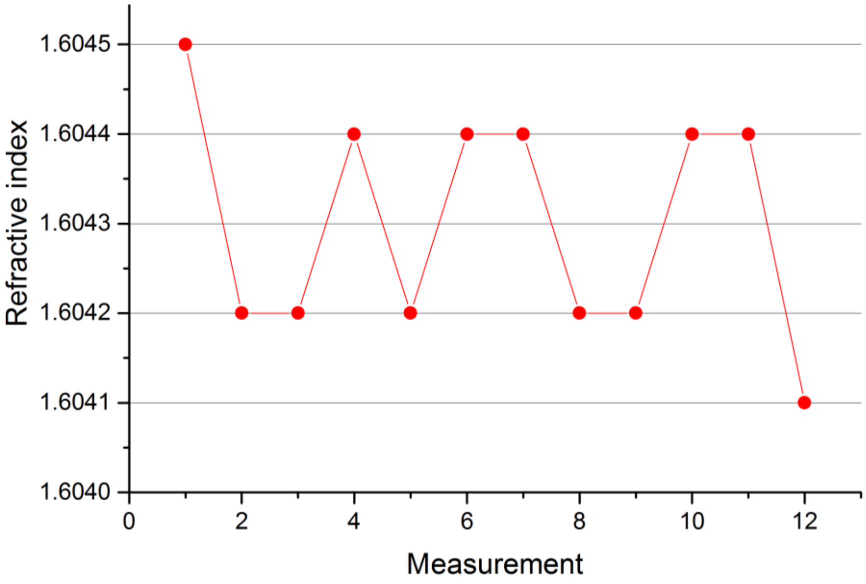

Figure 37. Refractive indices of GPWS SAL glass HIP46 (1400 °C/50 bar/180 min) at 12 different positions at 633 nm. (Prism coupler Metricon 2010)

compared to the refractive index measurement as well as the striae patterns photographed under illuminations of collimated light. A GPWS SAL glass sample (HIP46) sintered at 1400 °C for 180 min at 50 bar has been measured for its refractive index at 12 different positions as shown in Figure 37. It appears that the refractive index varies from 1.6041 to 1.6045 with a difference of about 4×10^{-4} after sintering at 1400 °C for 180 min. Striae can be observed in this sample under illuminations as demonstrated in Figure 38. These findings are compared to the simulation results by trying different values of diffusion coefficient for La^{3+} groups (e.g. La octahedra).

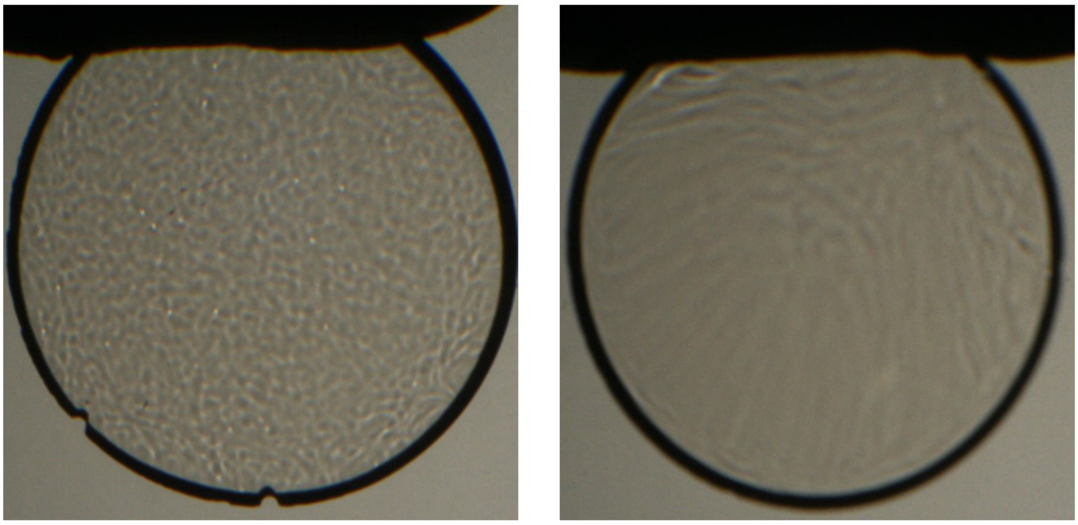

a) HIP49a 1400 °C/60 min b) HIP52 1400 °C/180 min

Figure 38. Refractive index fluctuation of polished GPWS SAL glasses sintered at 1400 °C for different sintering times. Diameter: 10 mm.

Since 1400 °C is far above T_g, the Stokes–Einstein relation should be applicable quite well. The diffusion coefficient for Al^{3+} group can be derived from Eq. (37) given their radius. The ionic radius of 4 coordinated Al^{3+}, 6 coordinated La^{3+} and O^{2-} are 39 pm[101], 104 pm[102] and 140 pm[101], respectively, which means a radii of 179 pm for an aluminum tetrahedron and 244 pm for a lanthanum octahedron, respectively.

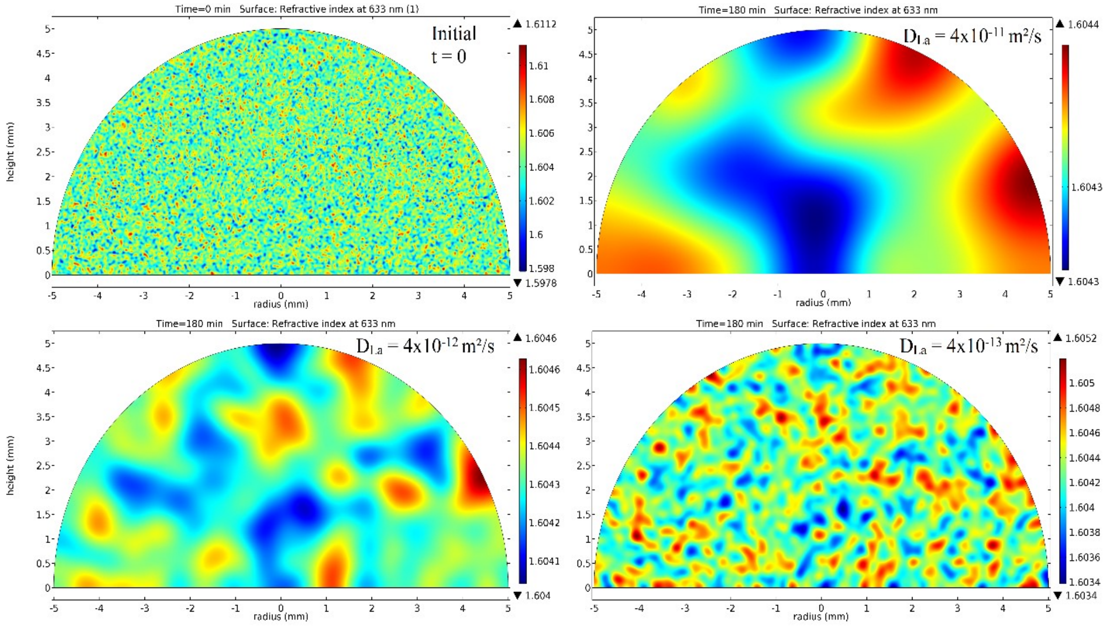

Figure 39. FEM simulation of refractive index of SAL glass after sintering at 1400 °C for 180 min with different diffusion coefficients for La species.

Figure 39 shows the simulation results of refractive index on SAL glass sample sintered at 1400 °C after 180 min at different diffusion coefficients. It is necessary to have a diffusion coefficient of 3-4×10^{-12} m^2/s to agree with the refractive index

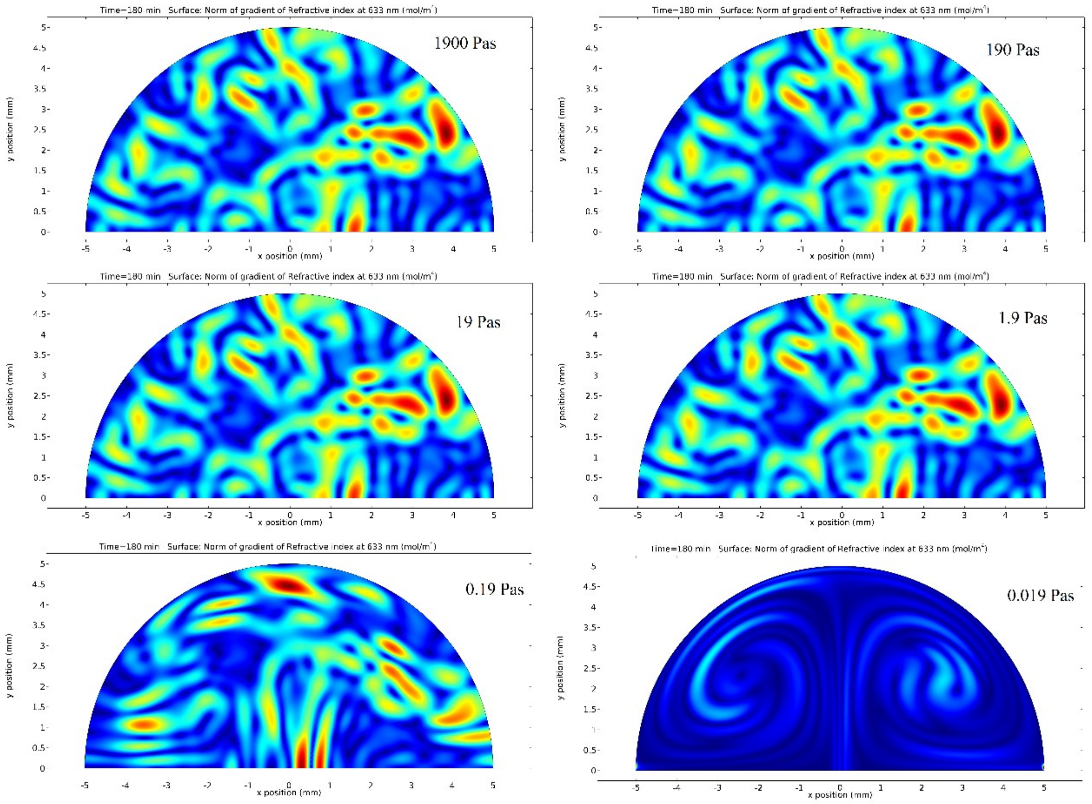

Figure 40. FEM Simulations of norm of gradient of refractive index of SAL glass sintered for 180 min with different viscosity values. Diffusion coefficient: 4x10^{-12} m^2/s.

measured in Figure 37. Figure 40 shows the same calculation with different viscosity values in magnitude of gradient of refractive index. No convection occurred when the viscosity stays above 0.19 Pas, which results in no long stream-like striae. These kind of striae are normally influenced by the convections. Those cases with viscosity higher than 0.19 Pas demonstrate patterns only by diffusion, which are curly. The HIP52 sample demonstrates stream-like patterns especially at the lower part of Figure 38. It can be deduced that the viscosity in this case must be close to or lower than 0.19 Pas. However, if the viscosity is too low (e.g. 0.019 Pas) the resulting patterns are perfectly stream-like, which is not the case observed in the experiment. Therefore, the viscosity can be estimated to be in the magnitude of 10^{-1} Pas at 1400 °C. Figure 41 shows the simulation results of norm of gradient of refractive index after a sintering at 1400 °C for 60 min and 180 min, respectively. Comparing the shape of patterns as well as their dimensions, these results are coincident to the experimental pictures as shown in Figure 38.

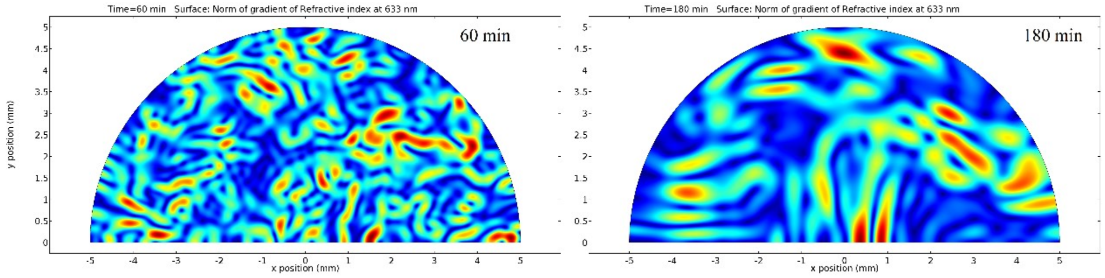

Figure 41. FEM Simulation of norm of gradient of refractive index of SAL glass sintered at 1400 °C for 60 min and 180 min, respectively. Viscosity: 0.2 Pas. Diffusion coefficient: $4\text{x}10^{-12}$ m²/s.

Together with the comparison of refractive index, both the diffusion coefficient and viscosity of SAL glass at 1400 °C have been estimated. Using Eq. (37), the radius of the diffusing La^{3+} group is then

$$r_{La} = \frac{k_B T}{6\pi\eta D_{La}} = 3060\,pm \tag{55}$$

which is similar to the size of about 6 La octahedra while the radius for Al group is 2250 pm, which is also the size of about 6 Al tetrahedra. From these numbers the collective motions of the La groups and Al groups are revealed. Finally, the magnitude viscosity of the SAL glass (in *Pas*) of our composition can be determined as

$$\log_{10}\eta = -11.447 + \frac{11251.464°C}{T(°C) - 402.896°C} \tag{56}$$

5.2 Determination of surface tension

The surface tension at high temperature has been determined via comparing the maximum heights and maximum diameters from the experiment and the FEM simulation as shown in Figure 30. Figure 42 demonstrates the evolution of the glass geometry at high temperature with surface tension of 0.37 N/m. The calculation is carried out at the viscosity of 1 Pas, which is a bit higher than the derived value at 1400 °C. Viscosity determines how fast the deformation of the glass under its own weight proceeds while surface tension determines the equilibrium shape of the final droplet. Figure 43 demonstrates the time-dependent variation of the maximum height and maximum diameter. The “equilibrium” geometry of the maximum height and diameter have been achieved in about 150 ms. Consequently, the time needed at 1400 °C for the similar evolution is less than 150 ms. Therefore, at 1400 °C with lower viscosity of about 0.2 Pas, the experimental dwelling time of 5 min is more than sufficient. Hence, by comparing these two geometry parameters the surface tension of the glass droplet is determined, which was found to be 0.37 N/m.

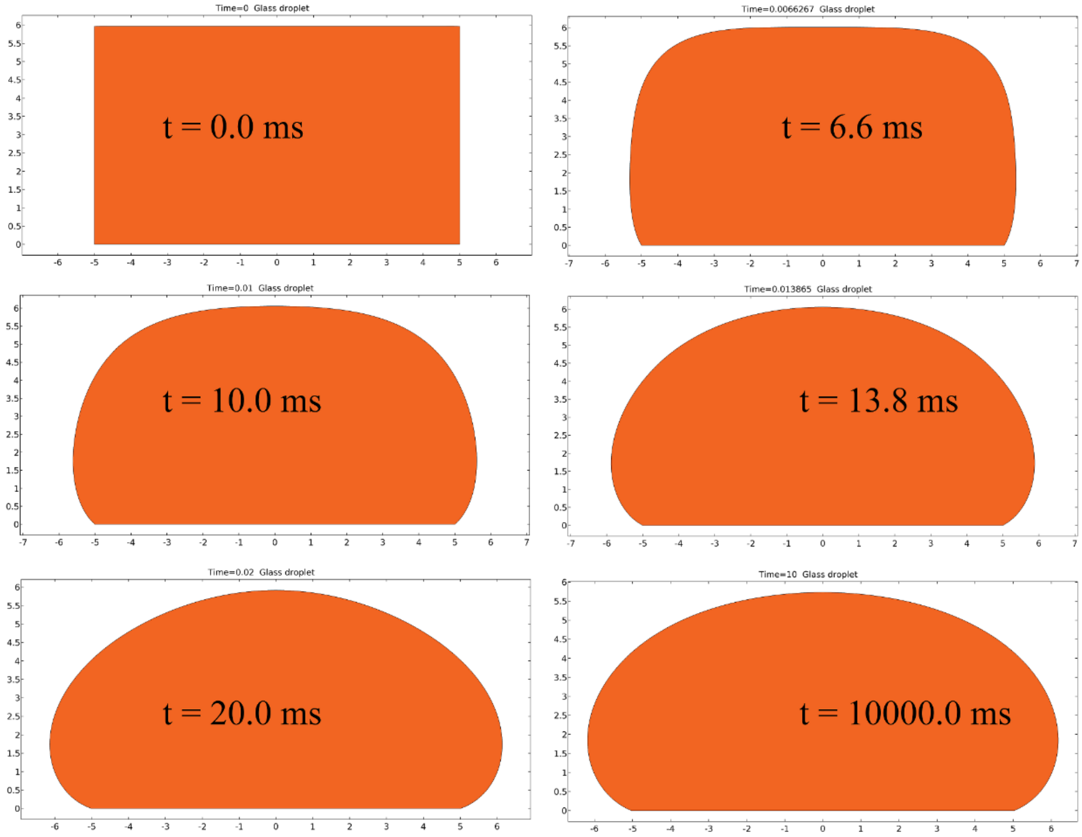

Figure 42. Evolution of glass geometry from a cylinder to a droplet under a surface tension of 0.37 N/m. Viscosity: 1 Pas, density 3200 kg/m^3.

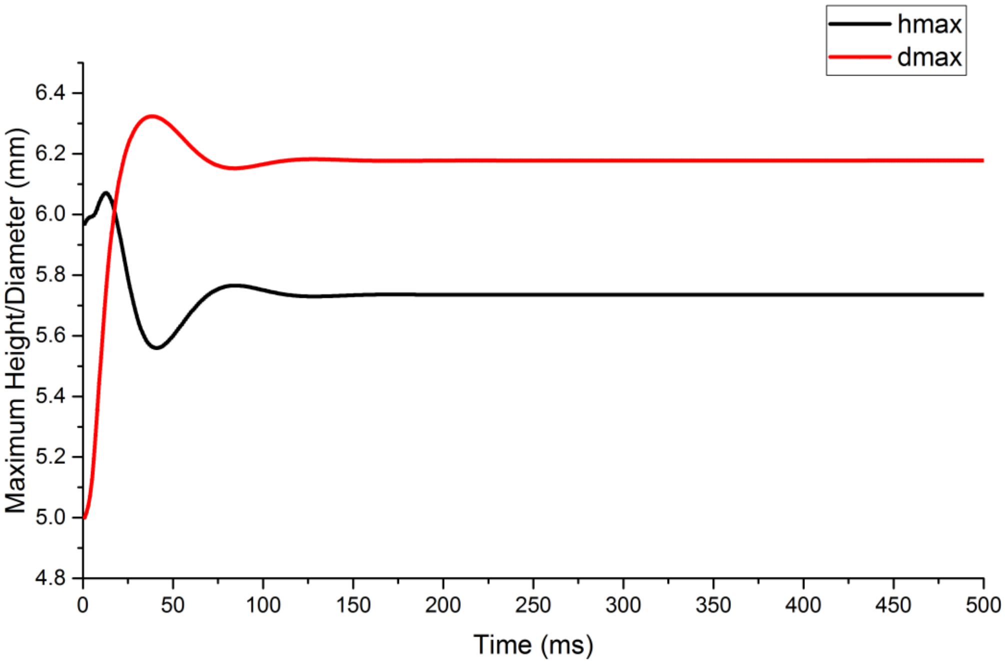

Figure 43. Evolution of maximum diameter and height of the glass droplet at 1 Pas with surface tension of 0.37 N/m.

5.3 Working temperature, pressure and particle size

From the theory presented in chapter 2, three factors are known to be able to influence the densification rate in sintering: the particle size, external pressure and sintering temperature. Their relative relations can be deduced from the viscous sintering theory with external pressure. Since the quenching and melting of SAL glass is known to be carried out at 1650 °C for 4 hours under normal atmosphere pressure, it will be taken as the reference working condition. It should be noticed that the atmosphere pressure is taken as zero point of the pressure through this paper.

First, the particle size will be estimated. The contributions of particle size and pressure to densification rate could be obtained using Eq. (30) with substitution of γ with γ_e. Here γ_e is no more constant (γ is still constant) but a function of external pressure. Since most of the sintering time spent in pressure-assisted sintering is the final stage, it is reasonable to approximate ϕ to unity. In order to achieve the same densification rate as reference (pressure-less), the parameters of an alternative pressure-assisted sintering should follow Eq. (55)

$$\frac{2\gamma}{r_1}+P_1=\frac{2\gamma}{r_2}+P_2 \tag{57}$$

where r_1, r_2, P_1 and P_2 are particle sizes and external pressures for the reference (case 1) and the pressure-assisted sintering (case 2), respectively. Since the external pressure in case 1 is 0 ($P_1 = 0$) meaning that the driving force for sintering is pure capillary pressure. The particle size in case 2 is assumed infinite ($r_2 \rightarrow \infty$) which means that the sintering is driven purely by external pressure. In this extreme case, Eq. (57) becomes

$$r_1 P_2 = 2\gamma \tag{58}$$

Figure 44 demonstrates the equivalent pressure in relation to the particle size in pressure-assisted sintering at constant temperature. It is found that using milled glass particles at 45 μm is equivalent to a sintering pressure of 0.16 bar. This is quite low due to the large dimension of the particle size. It would result in very low sintering rate in pressure-less sintering. However, if 50 bar of external pressure is applied, it is equivalently using 148 nm particles as starting material, which normally requires much more complicated preparations. Furthermore, if the 100 bar external pressure is applied, which is the maximum ability of our furnace; it is equivalent to using 74 nm particles as starting materials. Hence, an advantage of using easy preparing starting materials can be theoretically predicted. Also, an acceleration of about 50/0.16 ≈ 312 times higher sintering rate has been predicted from the calculation too. In other words, a 5

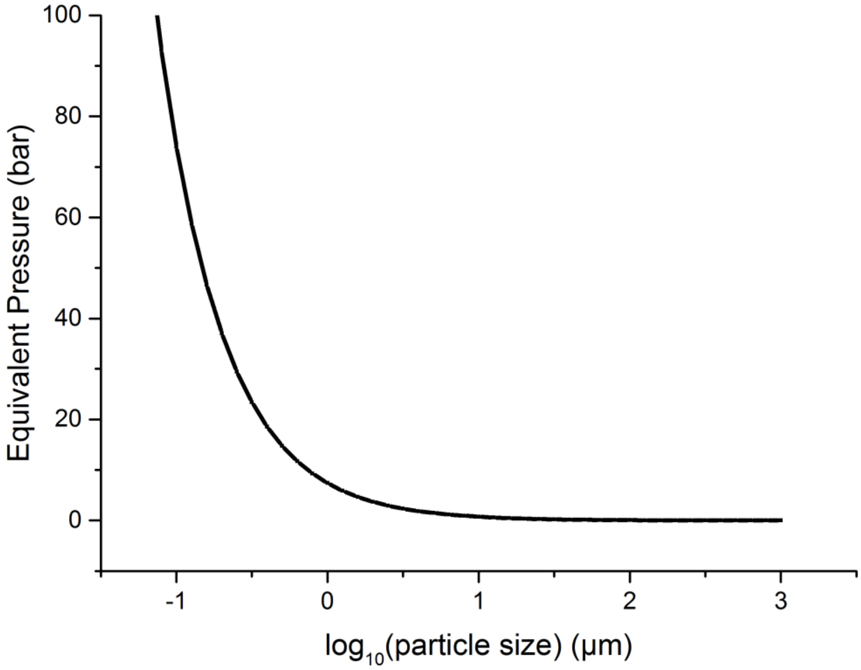

Figure 44. Equivalent pressure vs. particle size in pressure-assisted sintering to achieve the same densification rate. Surface tension: 0.37 N/m.

min sintering of 45 µm particles at 50 bar requires 10 hours at the same temperature and 0.16 bar to achieve the same degree of sintering.

The second relationship concerning the densification rate is the pressure-temperature relation at constant particle size. By assuming the VFT viscosity-temperature relation of Eq. (31), the temperature and pressure relation can be constructed via Eq. (30) with effective surface energy substituted. In order to achieve the same densification rate as the pressure-less sintering at temperature T_0 with particle size r_0, the reduced sintering temperature for pressure-assisted sintering with external pressure P_{ext} is

$$T = \frac{T_0 - T_c}{1 + \frac{T_0 - T_c}{B} \log_{10}(1 + \frac{P_{ext} r_0}{2\gamma})} + T_c \tag{59}$$

where T is the temperature needed in pressure-assisted sintering, B and T_c are VFT fitting parameters. Figure 45 has demonstrated one calculation instance for figuring out the temperature used in pressure-assisted sintering to achieve the same densification rate as in pressure-less reference sintering at 1650 °C with 45 µm particles at atmosphere pressure. The result shows that external pressure contributes to accelerate

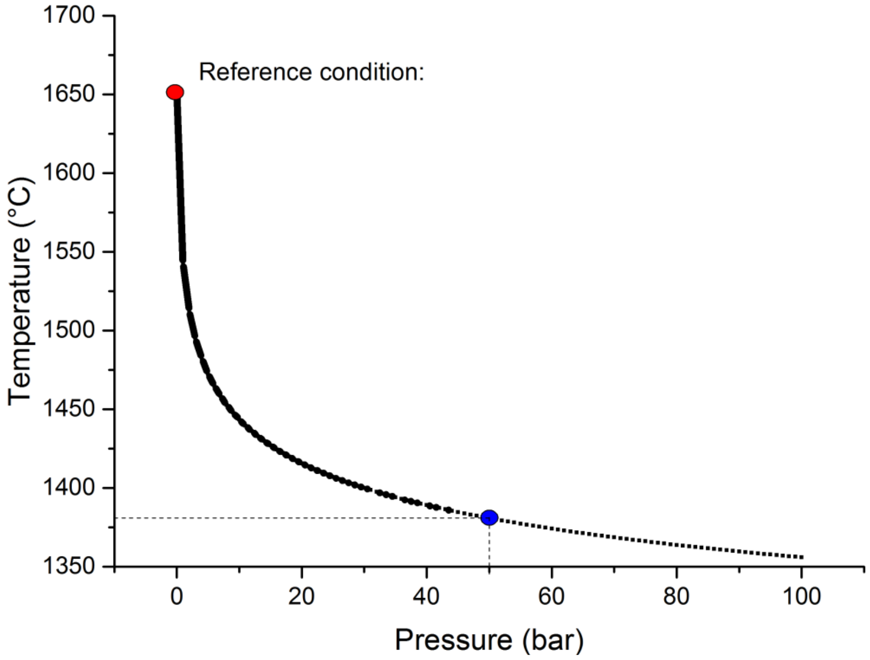

Figure 45. Temperature needed in pressure-assisted sintering to achieve same densification rate as in pressure-less sintering at 1650 °C in vacuum using 45 µm particles . The curve is calculated by the following parameters: B = 11251 °C, T_c = 403 °C, r_0 = 45 µm, T_0 = 1650 °C and γ = 0.37 N/m.

the sintering process, resulting in lower sintering temperature. By applying 50 bar, the sintering temperature has been efficiently reduced from 1650 °C to 1380 °C.

The final relationship is then the temperature-particle size relation. The alternative temperature T_2 that is necessary to achieve the same sintering rate as in the reference case (at T_1, with particle size a_1) can be obtained according to Eq. (30), which is shown in Eq. (60)

$$T_2 = \frac{1}{\frac{1}{T_1 - T_0} - \frac{1}{B}\log_{10}\frac{a_2}{a_1}} + T_0 \tag{60}$$

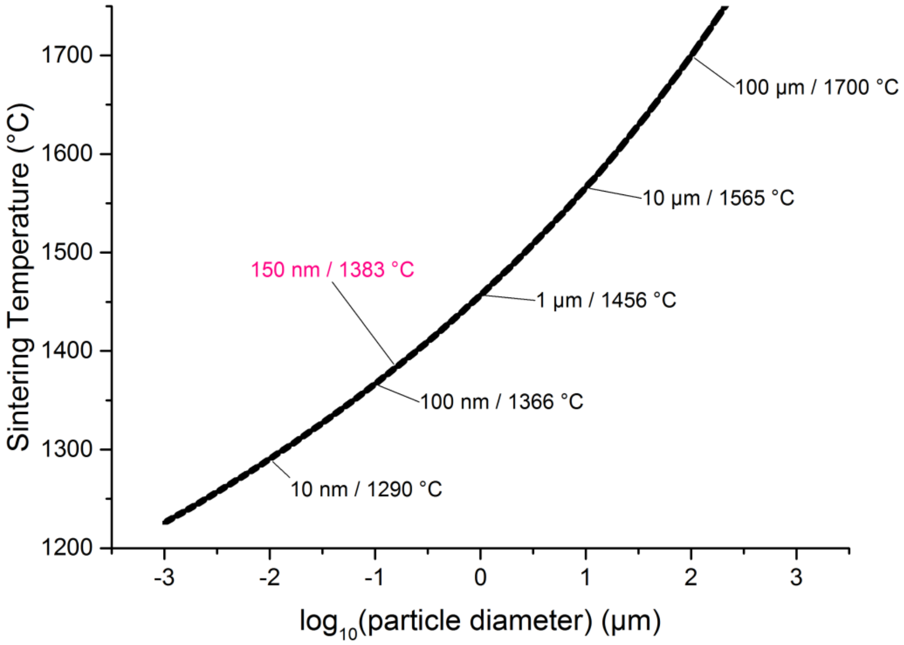

Figure 46. Equivalent Temperature-Particle size relation to achieve the same densification rate in viscous sintering. The curve is calculated by the following parameters: B = 11251 °C, T_c = 403 °C, r_0 = 45 μm, T_0 = 1650 °C and γ = 0.37 N/m.

where a_2 is the particle size in the alternative case. Figure 46 demonstrates one calculation of which sintering temperature should be used for glass particles with different sizes, to achieve the same densification rate. The result shows that with 150 nm particles, which is equivalent to about 50 bar as shown in Figure 41, the sintering temperature could be reduced from 1650 °C to 1380 °C using 45 μm particles. This means GPWS sintering at 1380 °C with 50 bar holds the same sintering rate as the melting and quenching at 1650 °C at atmosphere pressure.

In general, it has be revealed by the analytical and numerical calculations that 50 to 100 bar of external pressure plays a significant role in accelerating densification rate for sintering as well as reducing sintering temperature (200 K to 400 K from 1650 °C). Furthermore, the milling of the particles to a size of 50 - 100 µm is enough. No further preparation for finer particle is necessary. It can be concluded that the application of 50 – 100 bar is also efficient.

Chapter 6 Results and discussion

6.1 Densification below 1200 °C

In this section, the microstructure of GPWS SAL glasses sintered at temperatures below 1200 °C are investigated. Its densification behavior concerning pores, grains and phase boundaries is studied. The evolution of the microstructure will be compared to the sintering theory.

6.1.1 Pores and bumps

Figure 47 demonstrates the sintering stages of SAL glass in air at temperatures ranging from 950 °C to 1000 °C for 30 min, which means to be equivalent to the sintering in different dwelling times at the same temperature. Figure 47a shows the glass sample which is sintered at 950 °C with the lowest sintering rate, achieving a relative density of about 60 %. The dark area represents pores which are the majorities while the bright area represent the cross section of the necks connecting adjacent particles. This

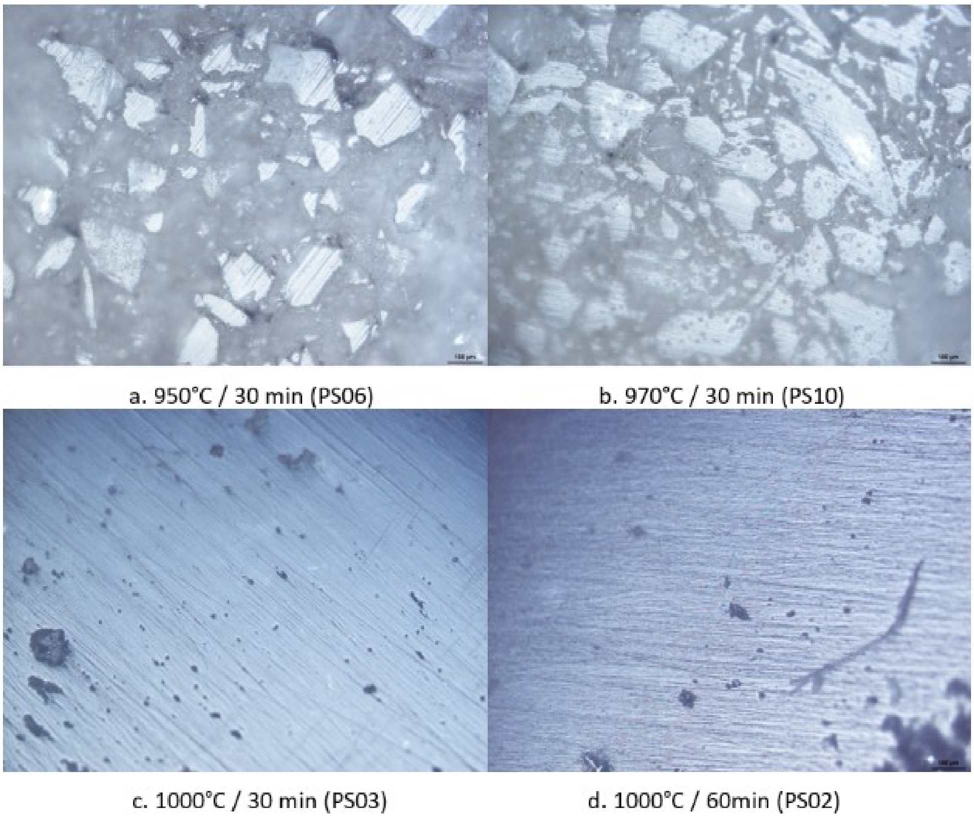

Figure 47. Bright field Microscopy of polished SAL glasses sintered in air at different temperatures 950 °C- 1000 °C for about 30 min.a) initial stage b) intermediate stage c) final stage d) 30 min after final stage. The dark area represents pores while the bright area stands for bulk.

topology belongs to the initial stage of sintering according to the sintering theory. Figure 47b shows the microstructure with a higher sintering degree, the pores become the minority but still connected to each other. This is corresponding to the description of the intermediate stage of sintering. Figure 47c shows another sintered green body at 1000 °C in 30 min. As the sintering temperature inceases, the micostructure developed further with most of the pores closed and isolated. It is the final stage of sintering. Figure 47d exhibits no big difference compared to Figure 47c even with a double dwelling time has been applied at the same temperature. Such a saturation indicates a much slower densification rate in the final stage of sintering which is coincident to the description of the sintering theory. Therefore, most of the sintering time for densification is spent in the final stage. The shape of pores appears non-spheric in samples sintered at 1000 °C for 1 hour due to the high viscosity.

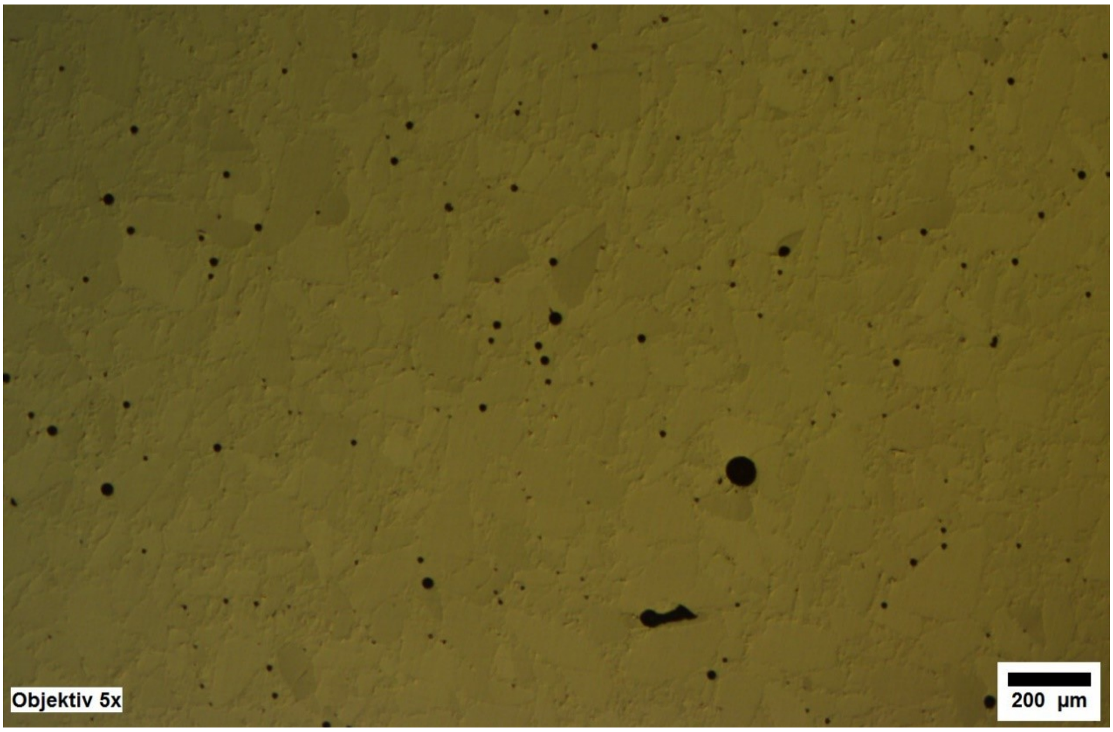

Figure 48. Differential Interference Contrast (DIC) Microscopy of polished SAL glass sintered (PS01) at 1000°C for 24 hours in air.

Figure 48 shows DIC microscopy of a SAL glass sintered for 24 hours at 1000 °C in air. The packing of the grains can be revealed in DIC microscopy due to their inhomogeneity in refractive index. The black spheres are pores, which have been confirmed by the observation of finer structures in deeper focus plane in bright field microscopy. This evidence agrees to the description in the microstructure model in sintering theory: most of the pores are formed along the grain boundaries in the transient from intermediate to final stage.

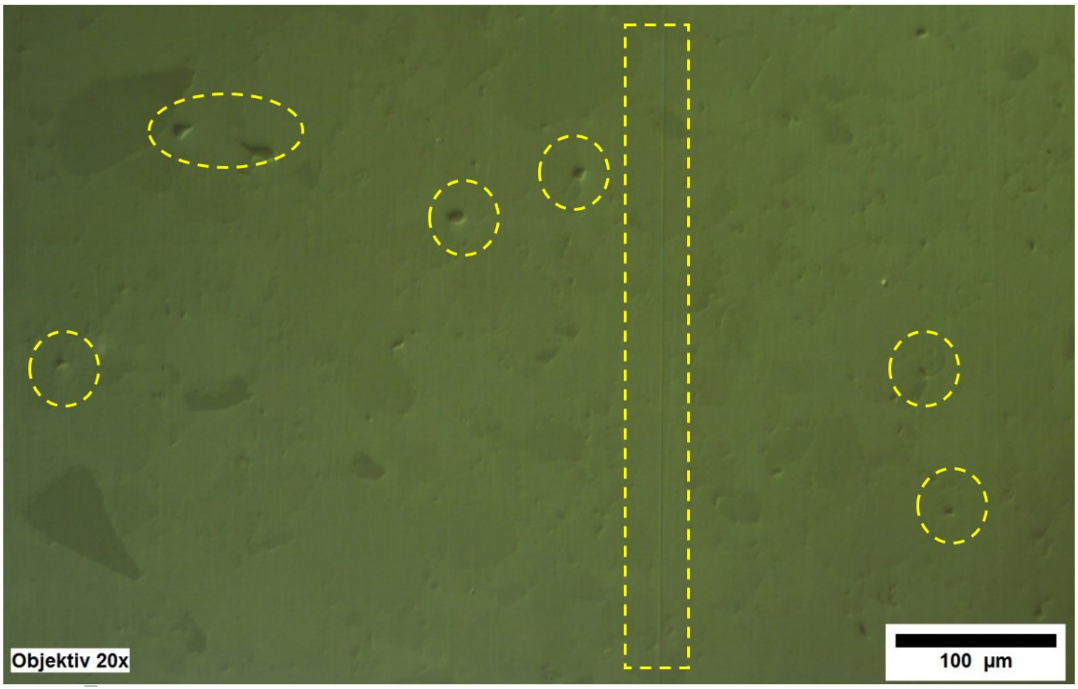

Figure 49. DIC microscopy of polished SAL glass (HIP_VAK) sintered at 1000 °C for 1 hour in vacuum (1- 2 mbar). Some of the suspecting pores as well as the scratch are marked with yellow dashed line.

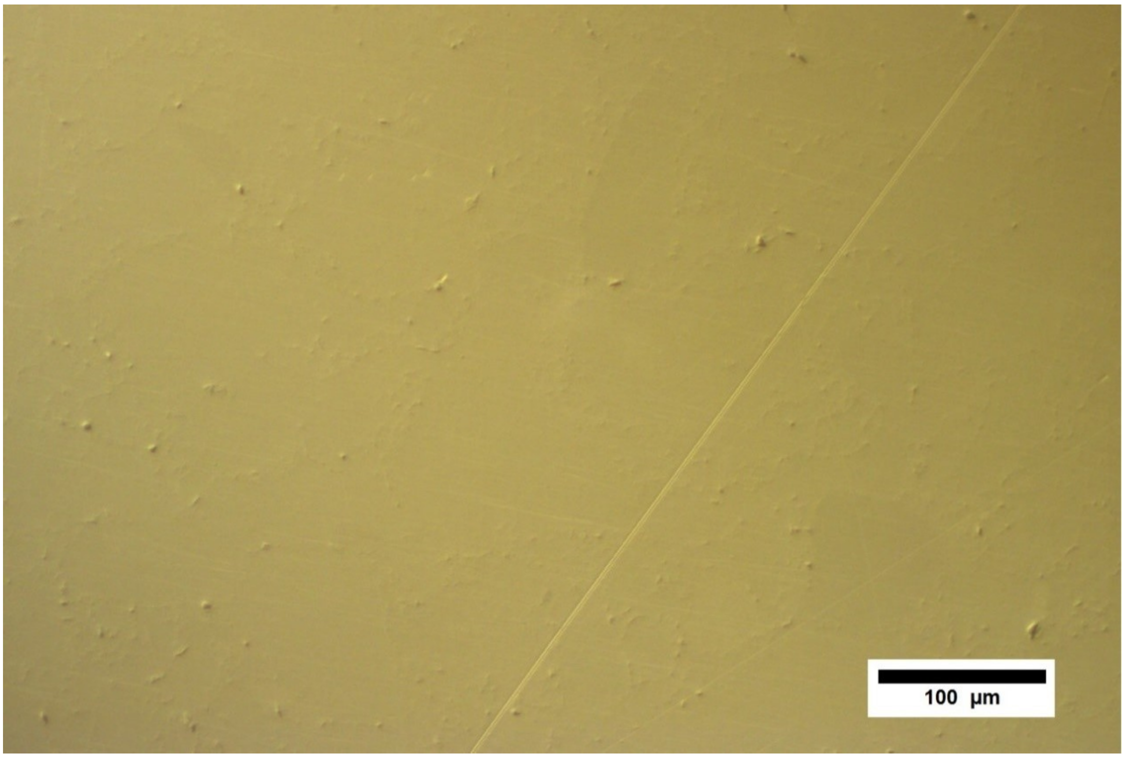

Figure 50. DIC microscopy (20 x) of polished GPS-SAL glass (HIP62) sintered at 1000 °C for 1 hour in 90 bar.

If the atmosphere is changed from air to vacuum for the same sintering process, the anticipated number of pores should be reduced. Figure 49 shows the DIC microscopy of SAL glass sintered at 1000 °C for 1 hour in vacuum. Since the convex or concave regions may not be distinguished in DIC microscopy as marked in Figure 49, a reference is needed to tell pores (concave) from bumps (convex). For this reason, the scratch (as concave surface) from polishing has been taken as a reference. In Figure 49 the scratch from polishing appears as a convex line (bump) which is opposite to the physical facts. Hence, the marked regions are actually bumps. Figure 49 is therefore an inverted picture in concave and convex regions. Figure 50 shows the GPWS SAL glass sintered at 90 bar at the same temperature in the Gas Pressure Sintering (GPS) furnace. It is corrected by using scratches as concave surfaces and appears similar to Figure 49. These bumps on sample surfaces differ from the glass matrix in mechanical strength in which the polishing process fails to smoothen them. These bumps have been confirmed using Atomic Force Microscopy (AFM) as shown in Figure 51, in which bright dots representing higher positions in Z direction are present along the boundaries.

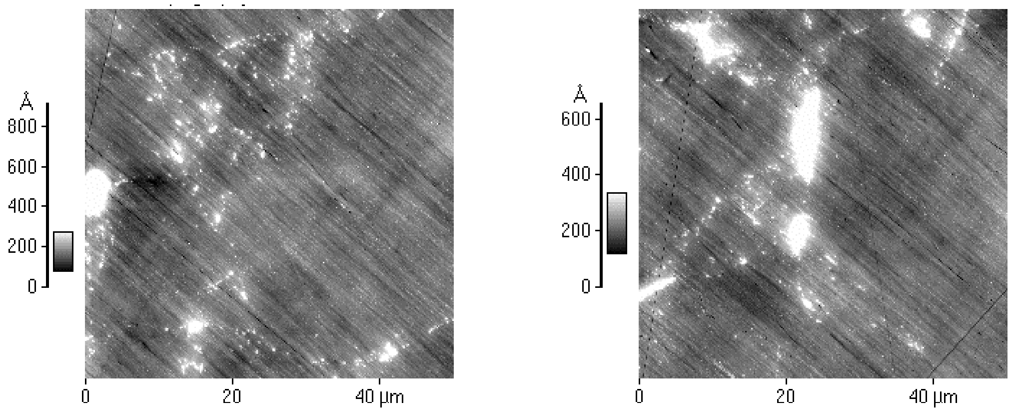

HIP62 (1000°,90bar,1h)
Topography, 0512G001.HDF

HIP62 (1000°,90bar,1h)
Topography, 0512G003.HDF

Figure 51. Atomic Force Microscopy (AFM) of HIP62 sintered at 1000 °C for 1 hour in 90 bar.

Finally, it can be concluded that no pores are found in GPWS SAL or vacuum sintered SAL samples at 1000 °C. In other words, entrapped gases are not observed in glasses sintered at the above conditions. The temperature and time for degassing in P1 of the GPWS procedure is efficient.

6.1.2 The boundary phase

Bumps were observed on the polished surfaces of GPWS or vacuum sintered SAL glass samples. However, their positions were not clearly revealed in microscopy. Figure 52 shows a Back Scattered Electron (BSE) microscopic image of one GPWS SAL glass after polishing. The grain boundaries were occupied by accumulated dark particles in dimensions of hundreds nanometers to a few microns. Such dark particles in BSE microscopy correspond to light elements, which might be silicon or aluminum according to our SAL composition. Figure 53 shows BSE micrograph at another

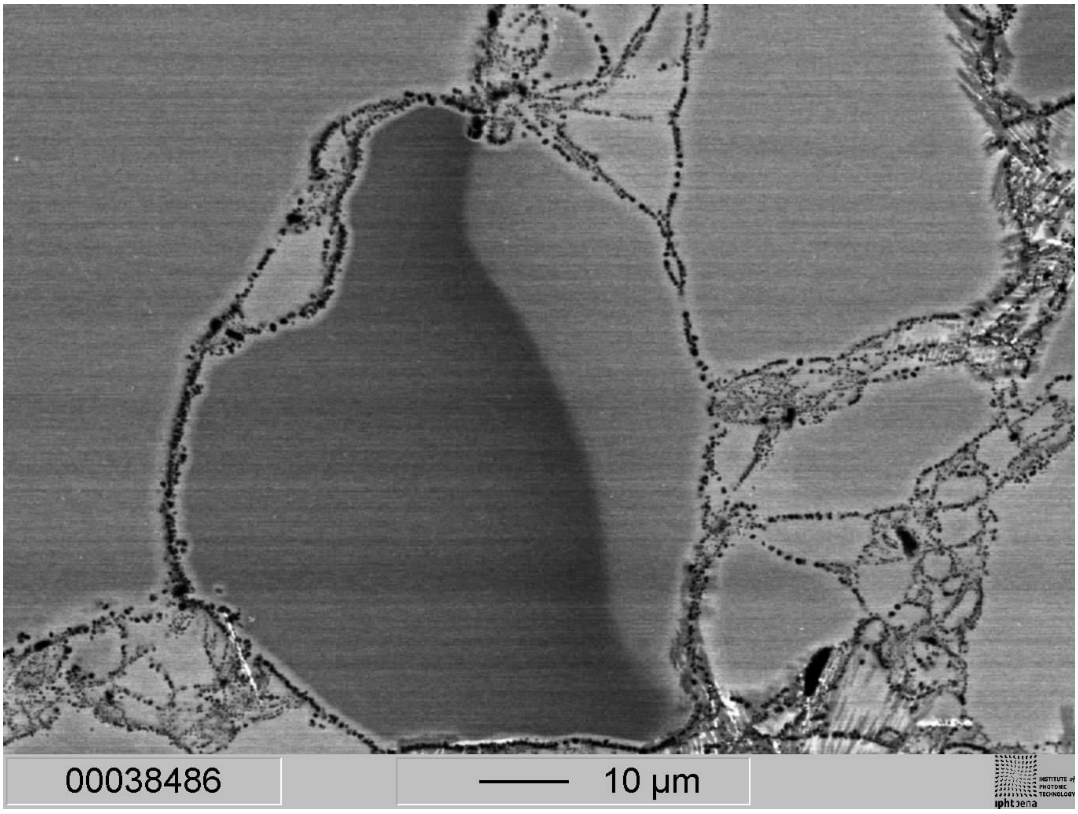

Figure 52. BSE micrograph of polished SAL glass (VSR02) sintered at 1000 °C for 50 hours in vacuum (< 1 mbar). The black grain boundaries consist of accumulated silicon-rich particles.

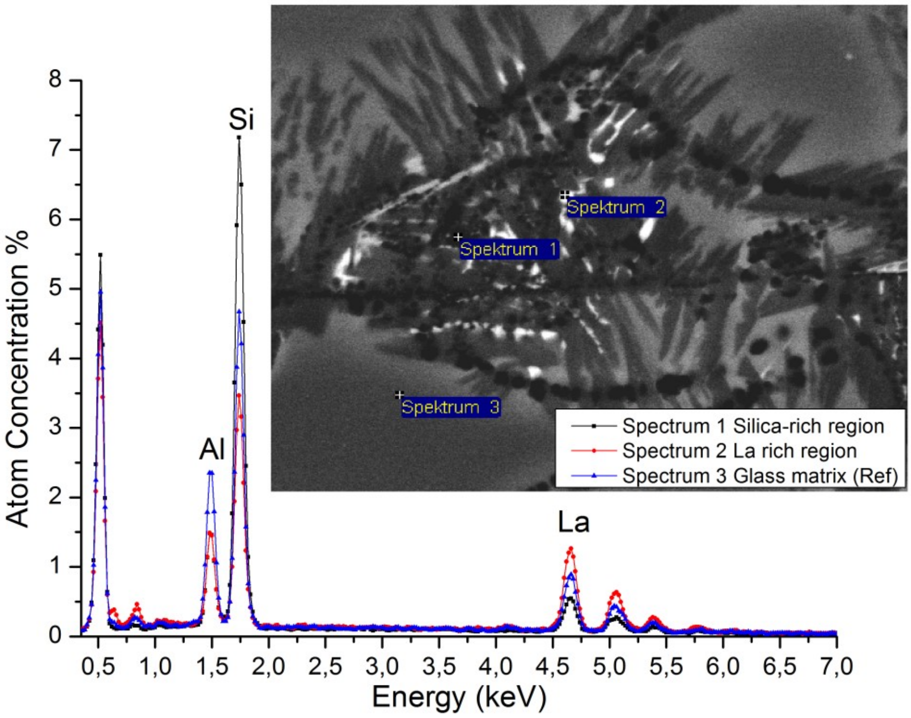

Figure 53. Energy Dispersive X-Ray spectrum and BSE micrograph of VSR02 (1000°C 50hour in vacuum).

position of the same sample as in Figure 52. Bright, intermediate and dark regions can be found in the BSE image. Figure 53 shows three Energy Dispersive X-Ray (EDX) spectra dedicated to bright, intermediate and dark regions. The dark region (spectrum 1) is very rich in silica (87 mol%, calculated from silicon concentration) as compared to the intermediate region for the glass matrix (spectrum 3, silica: 70 mol%). The bright region contains the most La, which is the heaviest element in SAL glass. From the great difference of silica concentration between spectrum 1 and spectrum 3, the black dots attribute to the silica rich phase. Additionally, the Al : La ratios in spectrum 2 and 3 are similar but are of great difference to spectrum 1. These imply that the dopants are relatively stable. Therefore, the boundary distributed bumps are silica rich grains. These grains can be used to explain the bumps found in AFM and DIC microscopy. Consider that the measurement spot for EDX is about 30 μm in diameter, which covers not only the dark but also the glass matrix region, the actual silica concentration in the dark boundary region is at least 87 mol%.

The source of these silica-rich bumps could be pure silica inclusions in the starting material, phase separation or crystallization. Since the glass transition temperature of silica glass is about 1200 °C, 1000 °C is too low for crystallization. In addition, such boundary phases were also found in GPWS SAL samples sintered at

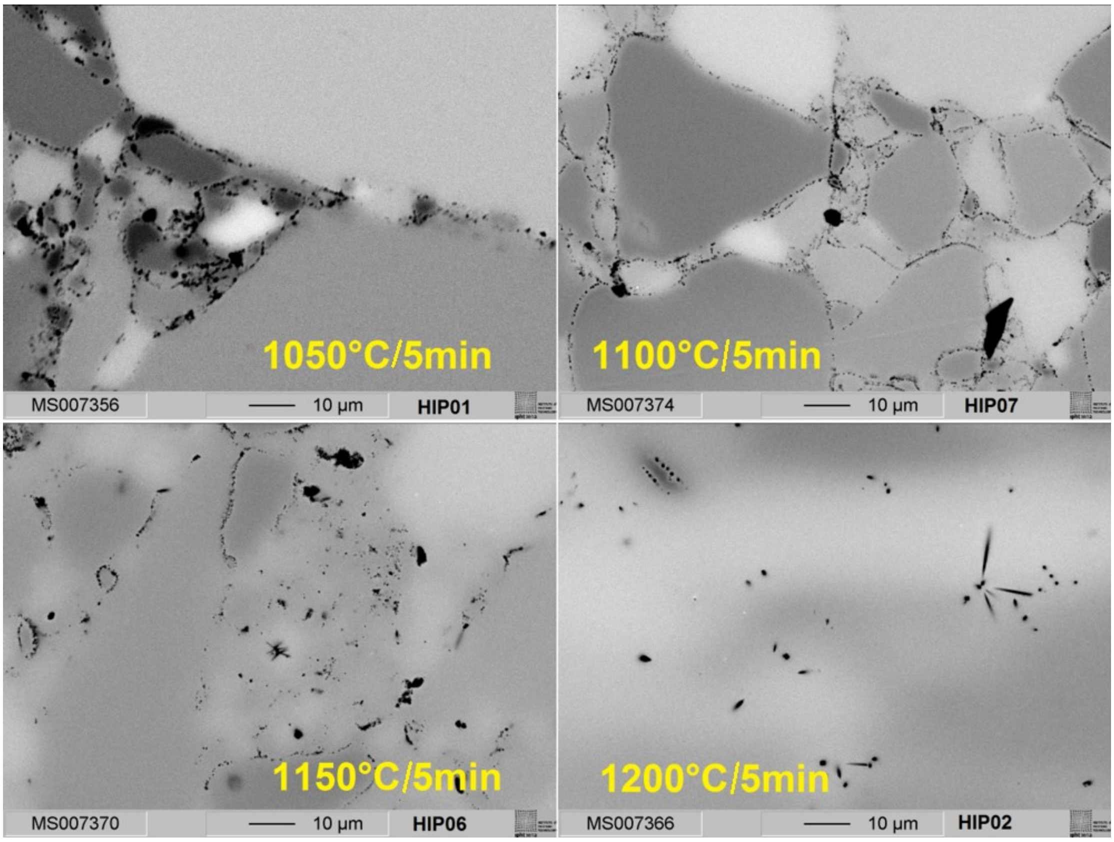

Figure 54. BSE micrograph of GPWS SAL glass sintered at different temperatures (1050 °C- 1200 °C) for 5 min in 50 bar. The boundary phase (silica-rich dots) is disappearing at elevated temperature.

1050 °C for only 5 min. The possibility of crystallization could be excluded. Figure 54 shows the development of these bumps at elevated temperatures for the same dwelling time. It demonstrates a tendency of reducing the amounts of bumps by increasing the temperature from 1050 °C to 1200 °C. This fact is against what should be observed at phase separation. In addition, the viscosity is still quite high (about 10^9 Pas); therefore, phase separation can also be excluded. In addition, the BSE image at 1200 °C in Figure 54 implies a melting behavior of these bumps at 1200 °C, which is normally the T_g of pure silica glass.

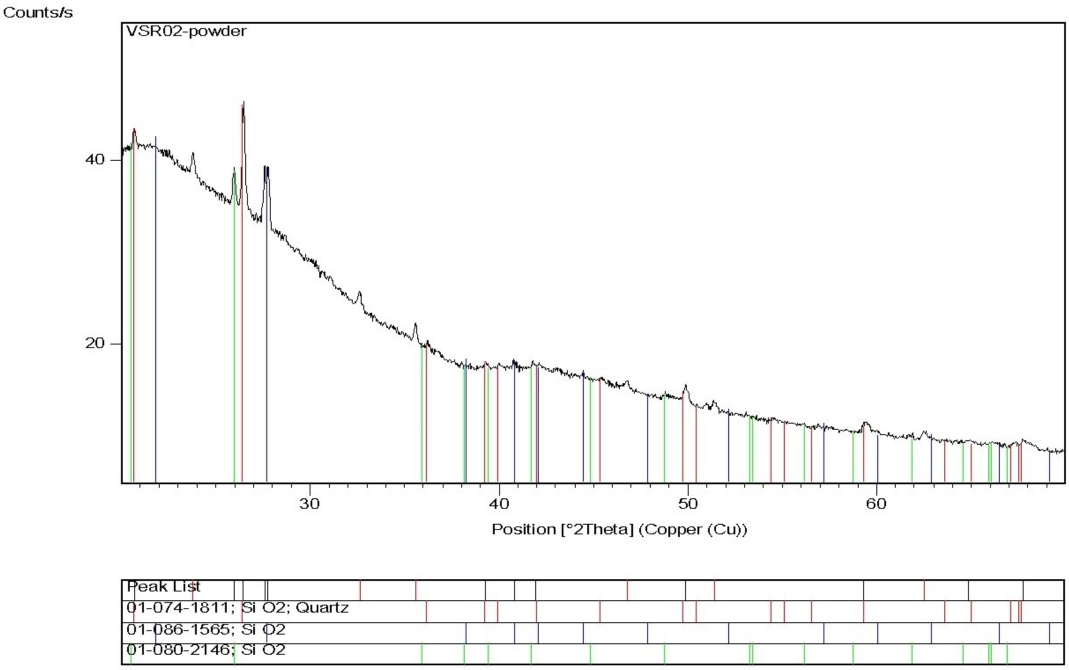

Figure 55. XRD pattern of starting particles for VSR02. (Sintered at 1000 °C for 50 hours in vacuum). Quartz has been found as minority in the glass matrix.

The remaining possible reason is silica rich inclusions. Figure 55 shows the XRD patterns of the starting powders in which quartz was found. This crystalline phase was not found in the frit SAL glass droplet before using the ball mills, which is made of Agate[103], a variety of silica, which is known for its very fine grains. Figure 56 shows the SEM and BSE microscopic images of the starting particles. The size distribution of the particles is so broad that it ranges from hundred nanometers to hundred micrometers.

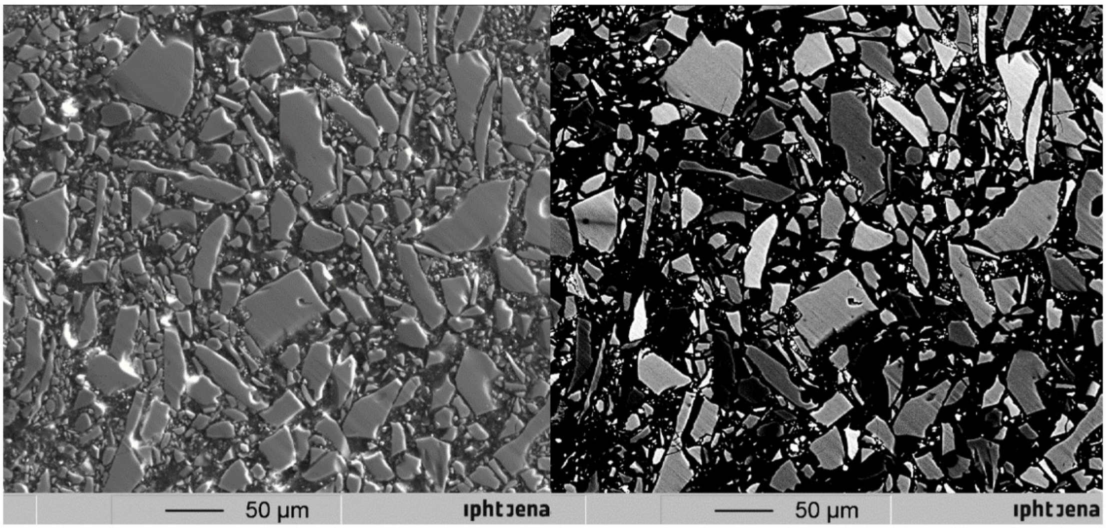

Figure 56. SE (left) and BSE (right) micrographs of starting particles filtered by a 100 µm sieve.

This confirms the source of the silica rich bumps contained in the starting powder. This also explains their accumulative distribution along the grain boundaries, which should not exist according to ideal glass sintering theory. Besides, the concentration of Lanthanum is quite different between particles according to the BSE picture, which indicates a poor homogeneity in La dopants.

6.1.3 *Inhomogeneity between grains*

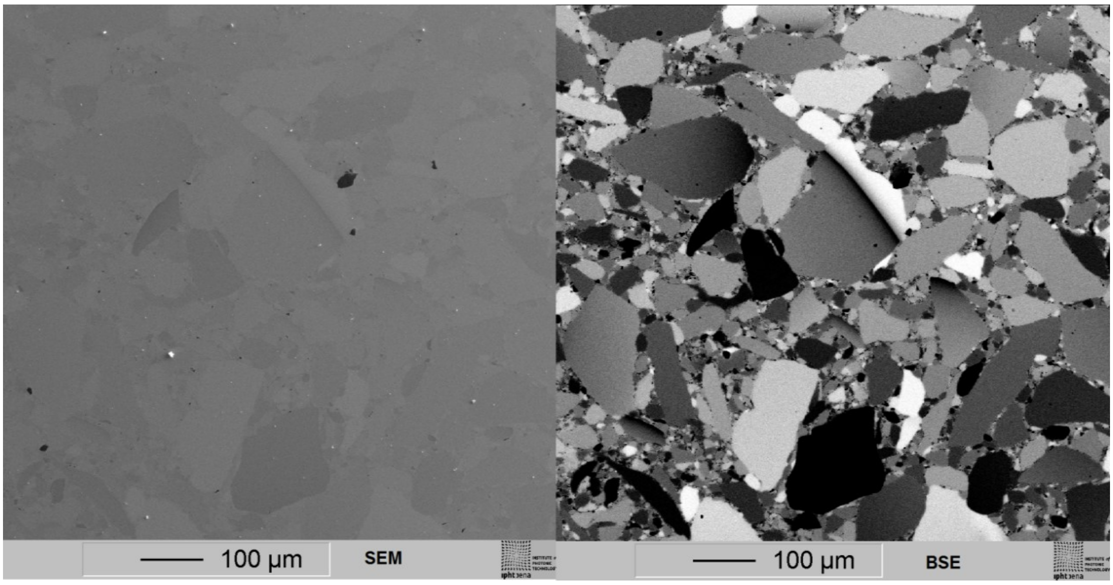

Figure 57. SE image (left) and Back Scattered Electron (BSE) Microscopy of polished SAL glass (HIP01) sintered at 1050 °C for 1 hour at 50 bar measured on the same position.

Except for the pores and bumps, compositional differences between particles have already been observed in Figure 56. Figure 57 exhibits both SEM and BSE microscopic images of one GPWS SAL sample, which is sintered at 1050 °C for 1 hour at 50 bar. In SEM microscopy, the compaction of grains is observable which is similar to the DIC microscopy. In BSE microscopy on the other hand, the contrast is just similar to the starting material as shown in Figure 56. Although a full densification has been achieved, the GPWS SAL glass sintered at these temperatures and times is opaque. This might arise from the scattering effect of the compaction of inhomogeneous grains.

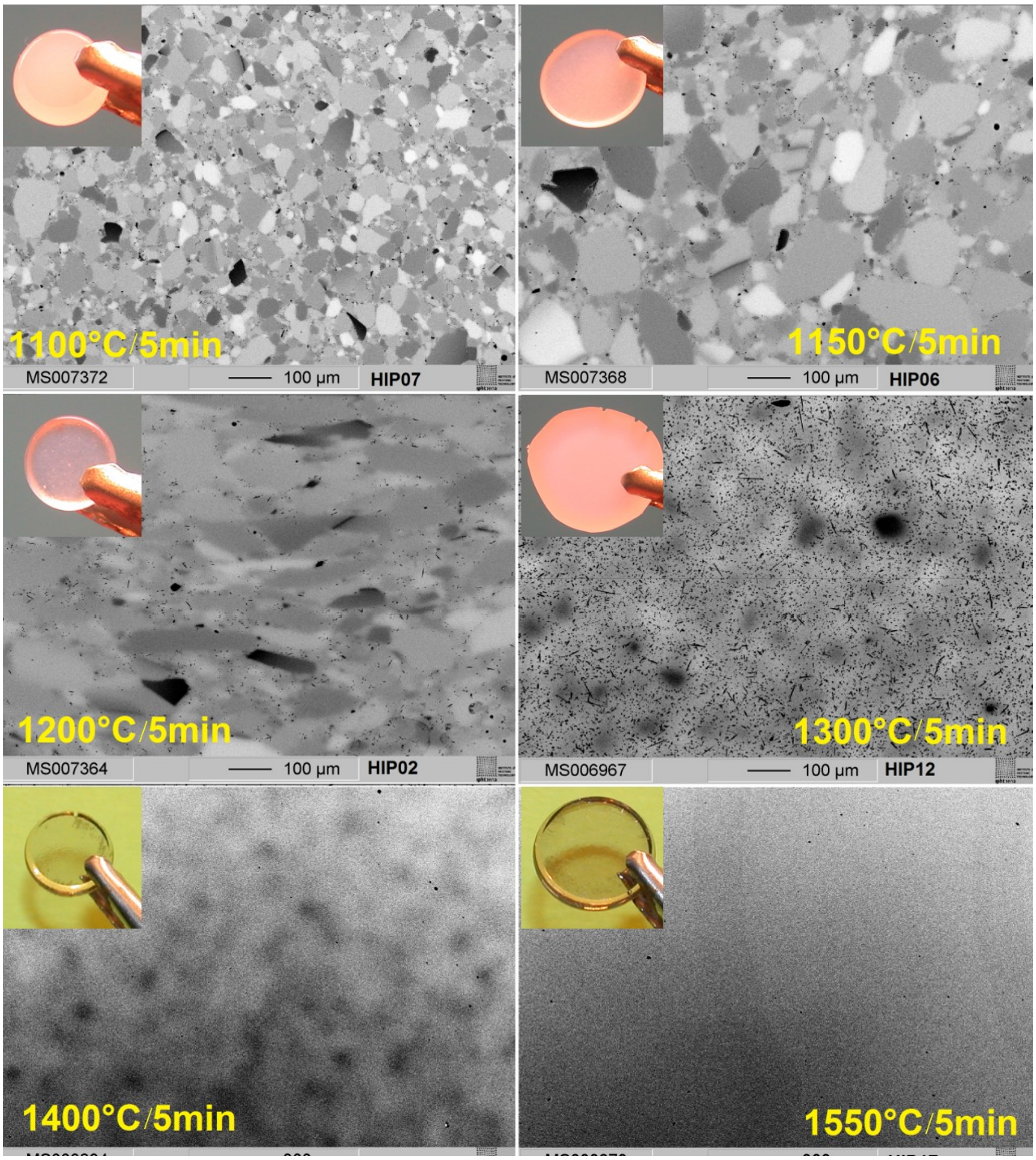

Figure 58. BSE micrograph of GPWS SAL glass sintered at different temperatures (1100 °C – 1550 °C) for 5 min at 50 bar. The corresponding pictures demonstrate their transparency.

Figure 58 demonstrates the relations between the microstructure in BSE microscopic images and the corresponding macroscopic appearance of the GPWS SAL glass sintered at higher temperatures. The transparency of sample HIP07 (1100 °C) is the poorest due to the presence of both inhomgeneous grains and boundary bumps while the HIP06 (1150 °C) becomes more transparent since some of the bumps were dissolved. The HIP02 (1200 °C) shows even better transparency due to the further dissolution of boundary bumps. However, when the temperature increases further, the HIP12 (1300 °C) becomes more opaque again due to the Mullite crystallization which will be disscussed in the next section. At 1400 °C it turned out that Mullite crystals were all dissolved. The appearance of HIP14 (1400 °C) is full transparent even though the BSE microscopic image is still not fully homogeneized. This implies that the exisitence of boundary bumps and the Mullite crystals make the GPWS SAL glass opaque at temperatures below 1400 °C. The inhomogeneous grains should not be responsible for the opacity of the SAL glasses sintered below 1400 °C.

Although the inhomogeneous grains did not make the glasses opaque, they vary the final refractive index. According to the study by Litzkendorf et al.[21], the refractive index of La and Al co-doped silica glass can be estimated by Eq. *(*19*)*

$$n = 1.456 + 0.0094 \cdot x_{La_2O_3} + 0.0032 \cdot x_{Al_2O_3} \tag{61}$$

where x_{La2O3} and x_{Al2O3} are the molar fractions of the codopants in mol%. 1.456 is the refractive index of the parent silica glass. The molar fractions have been examined by positional scans of WDX measurements. Figure 59 shows two WDX scans of two different GPWS SAL glass samples. Relative to their mean value in concentrations, Al_2O_3 and La_2O_3 have fluctuations of 0.14 mol% and 0.28 mol% at 1100 °C (HIP11). At HIP13 which was sintered at higher temperature (1350 °C), they have been

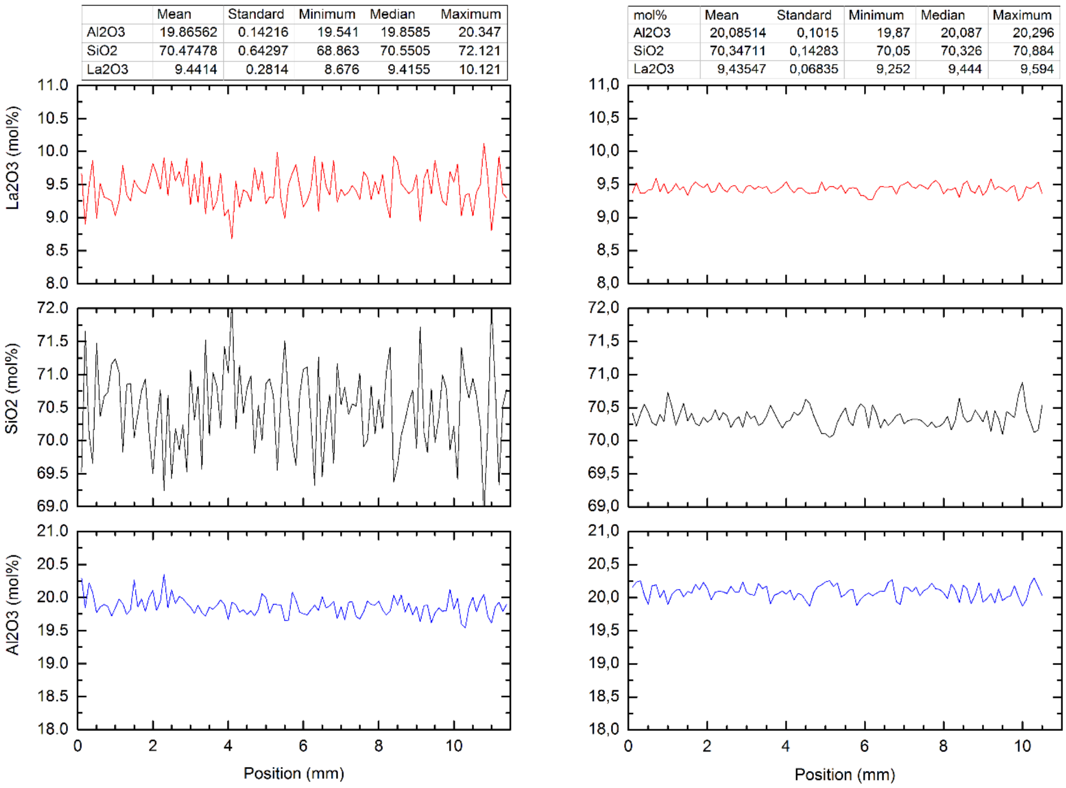

	Mean	Standard	Minimum	Median	Maximum
Al2O3	19.86562	0.14216	19.541	19.8585	20.347
SiO2	70.47478	0.64297	68.863	70.5505	72.121
La2O3	9.4414	0.2814	8.676	9.4155	10.121

mol%	Mean	Standard	Minimum	Median	Maximum
Al2O3	20,08514	0,1015	19,87	20,087	20,296
SiO2	70,34711	0,14283	70,05	70,326	70,884
La2O3	9,43547	0,06835	9,252	9,444	9,594

Figure 59. Quantitative homogenizing effect of La concentration characterized by WDX scan over the GPWS SAL samples (11 mm) of HIP11(left, 1100 °C/30 min/50 bar) and HIP13(right, 1350 °C/5 min/50 bar).The tables on top show the standard deviations of each element in mol%.

homogenized to 0.11 mol% and 0.07 mol%, respectively. Using Eq. (19), the refractive index fluctuations are $\pm 31\times 10^{-4}$ and $\pm 9.6\times 10^{-4}$ for HIP11 and HIP13, respectively. Therefore, a design with $\pm 1.0\times 10^{-3}$ and $\pm 1.0\times 10^{-4}$ varation in refractive index requires at least 0.1 mol% and 0.01 mol% of variation in La_2O_3 concentration in the starting glassy powders. This is the required homogeneity for the vitrification process if the desired consolidation temperature is below 1200 °C.

6.1.4 Summary for microstructure

In summary, pores were found along the boundaries at glass samples sintered at 1000 °C for 24 hours in air. Full densification was achieved by vacuum sintering or GPWS for SAL glass at 1000 °C for 1 hour. Therefore, 1000 °C and 1 hour dwelling time is sufficient for the P1 of the GPWS procedure. Silica rich crystalline inclusions (bumps) were found distributed along the grain boundaries. They are responsible for the opacity of the SAL glass sintered below 1200 °C. The source of these silica rich bumps are neither crystallization nor phase separation but inclusions from the agate ball miller. Hence, even pure silica grains should be considered as impurities in the consolidation process considering the transparency of the final sintered SAL glass below 1200 °C. The refractive index variations induced by inhomogeneity between grains are characterized. The requirement of the homogeneity in La_2O_3 in particles prepared by the vitrification process can be known therefore.

6.2 Crystallization

Generally, crystals in glass arise from crystallization in the glass matrix above glass transition temperature, reactions of the glass melt with the refractory material or undissolved raw material. In our study, glassy particles from frit glass are used, so no crystalline inclusions are expected in the SiO_2-Al_2O_3-La_2O_3 ternary system. The temperature range corresponding to crystallization in SAL glass has been studied from 1000 °C to 1550 °C in reducing (argon) atmosphere.

6.2.1 Crystallization of Mullite

Figure 60 proves the amorphous state of the quenched SAL glass powder from a melt at 1650 °C for 4 hours. GPWS SAL glasses sintered at 1000 °C - 1350 °C exhibit crystallization as seen at XRD measurement. Figure 61 shows one XRD pattern of one GPWS SAL glass sample sintered at 1250 °C for 15 min at 50 bar. The peaks from Mullite are identified which are overlapped with the bulk from the glass matrix. The corresponding microscopic image of a similar sample is shown in Figure 62. Tens of micrometers long needles were observed in appearance of dots (out-of-plane direction) and bars (parallel to surface). Figure 63 shows the BSE microscopic image of another similar sample, in which the crystals shapes are clearly seen. They consist of light elements such as Si and Al and appear as dark region in BSE microscopy. This confirms the Mullite found in XRD patterns.

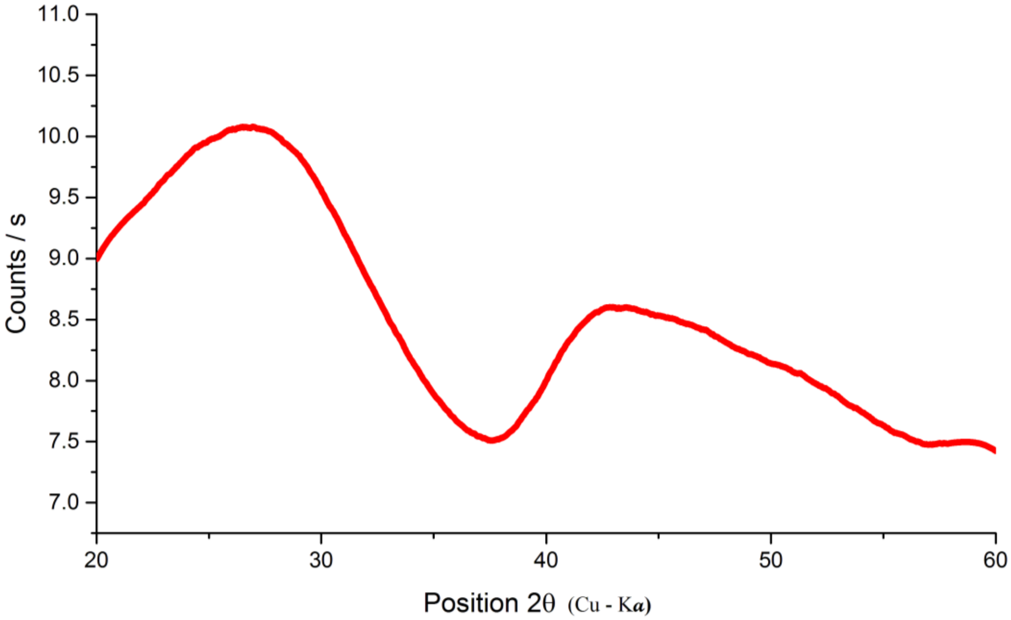

Figure 60.X-Ray diffraction pattern of starting SAL glass powder.

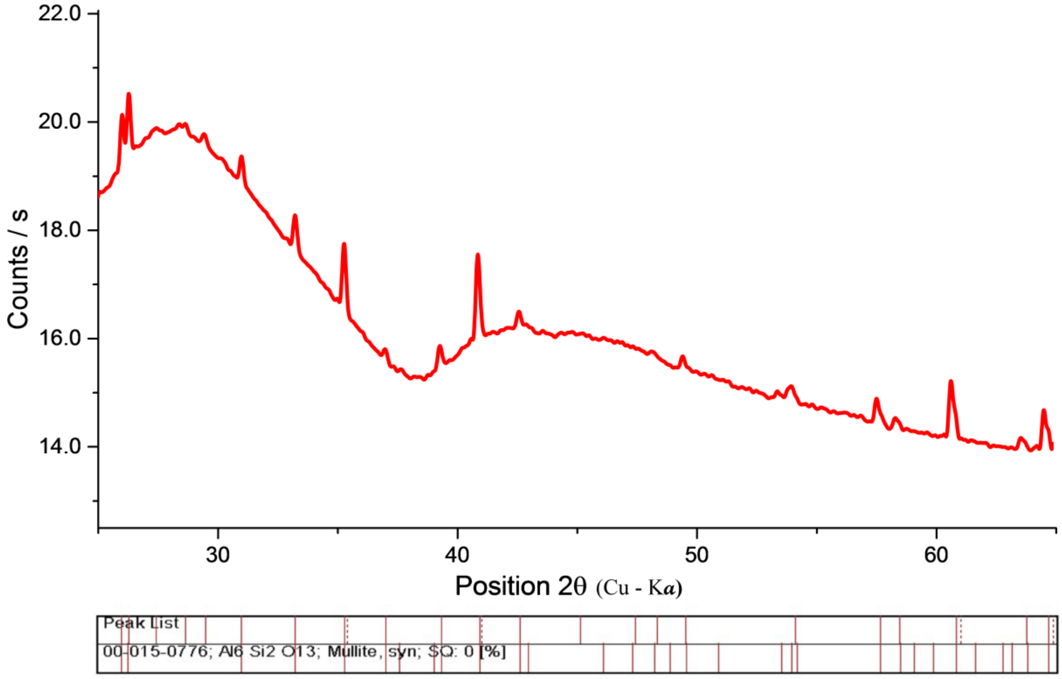

Figure 61. X-Ray diffraction pattern of GPS-SAL glass (HIP05) sintered at 1250 °C for 15min at 50 bar Argon.

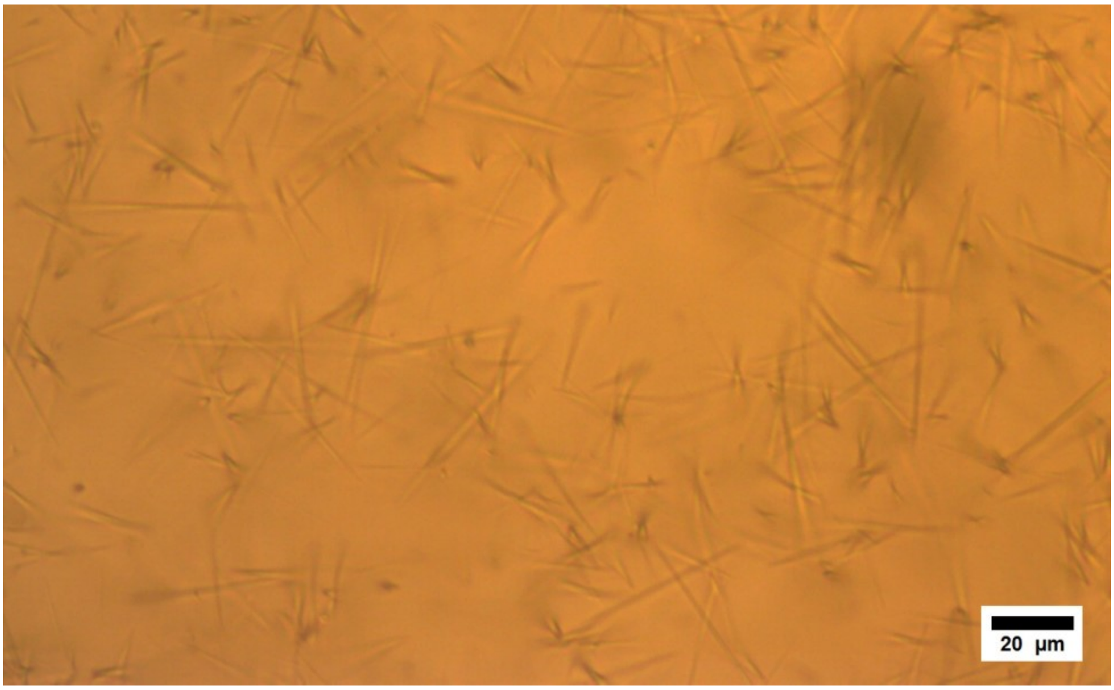

Figure 62. Dark-field Microscopy of GPS-SAL glass (HIP13) sintered at 1350 °C for 5 min in 50bar Argon. Needles like Mullite crystals are observable.

6.2.2 *Identification of Mullite phase*

Since Mullite has two phases with different ratios of Al_2O_3 : SiO_2: the low temperature 3 : 2 (3 $Al_2O_3 \cdot 2 SiO_2$) phase and the high temperature 2 : 1 (2 Al_2O_3 :

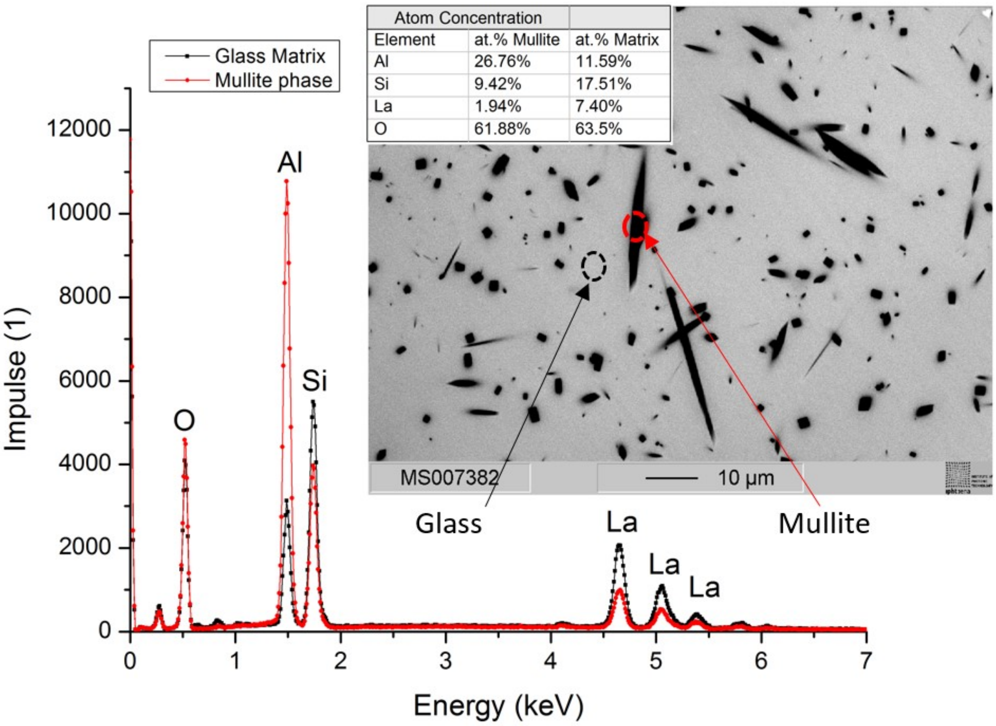

Atom Concentration		
Element	at.% Mullite	at.% Matrix
Al	26.76%	11.59%
Si	9.42%	17.51%
La	1.94%	7.40%
O	61.88%	63.5%

Figure 63. BSE micrograph of GPS-SAL glass (HIP12) sintered at 1300 °C for 5 min at 50 bar and the corresponding EDX spectrum at a region with Mullite and the glass matrix, respectively.

SiO_2) Mullite phase. According to the EDX spectra in Figure 63, the derived molar ratio of $Al_2O_3 : SiO_2$ in the dark needle is 1.42. This is close to 3 : 2 Mullite, which belongs to the low temperature phase of SiO_2·Mullite (3 : 2). This result is coincident with the Al_2O_3-SiO_2 phase diagram (Figure 64) summarized in Bergeron's study[104]. Since the phase diagram is a binary phase diagram and our glass system is ternary, a manual "phase separation" has to be made in order to find out the corresponding position of the alumina before the phase diagram in Figure 64 can be used. For this purpose, the SAL glass model proposed by Shelby[105] is used. It is assumed that the SAL glass comprises $SiO_{4/2}$ and $AlO_{4/2}$ tetrahedra interconnecting network with La^{3+} cations as dopant. Since $SiO_{4/2}$ is neutral and $AlO^-_{4/2}$ has a charge of -1, the La^{3+} is supposed to connect to only the $AlO^-_{4/2}$ tetrahedra in this ideal case. Now it is supposed that $AlO^-_{4/2}$ tetrahedra are all detached from the glass network, which makes four additional non-bridging oxygen groups that are suited to connect to La^{3+}. In this case, it makes -1 charge from each Oxygen vertex, resulting in -5 charge for each detached $AlO^-_{4/2}$ tetrahedron. Now all these tetrahedra are required to neutralize with La^{3+}, which is assumed to be 20 in

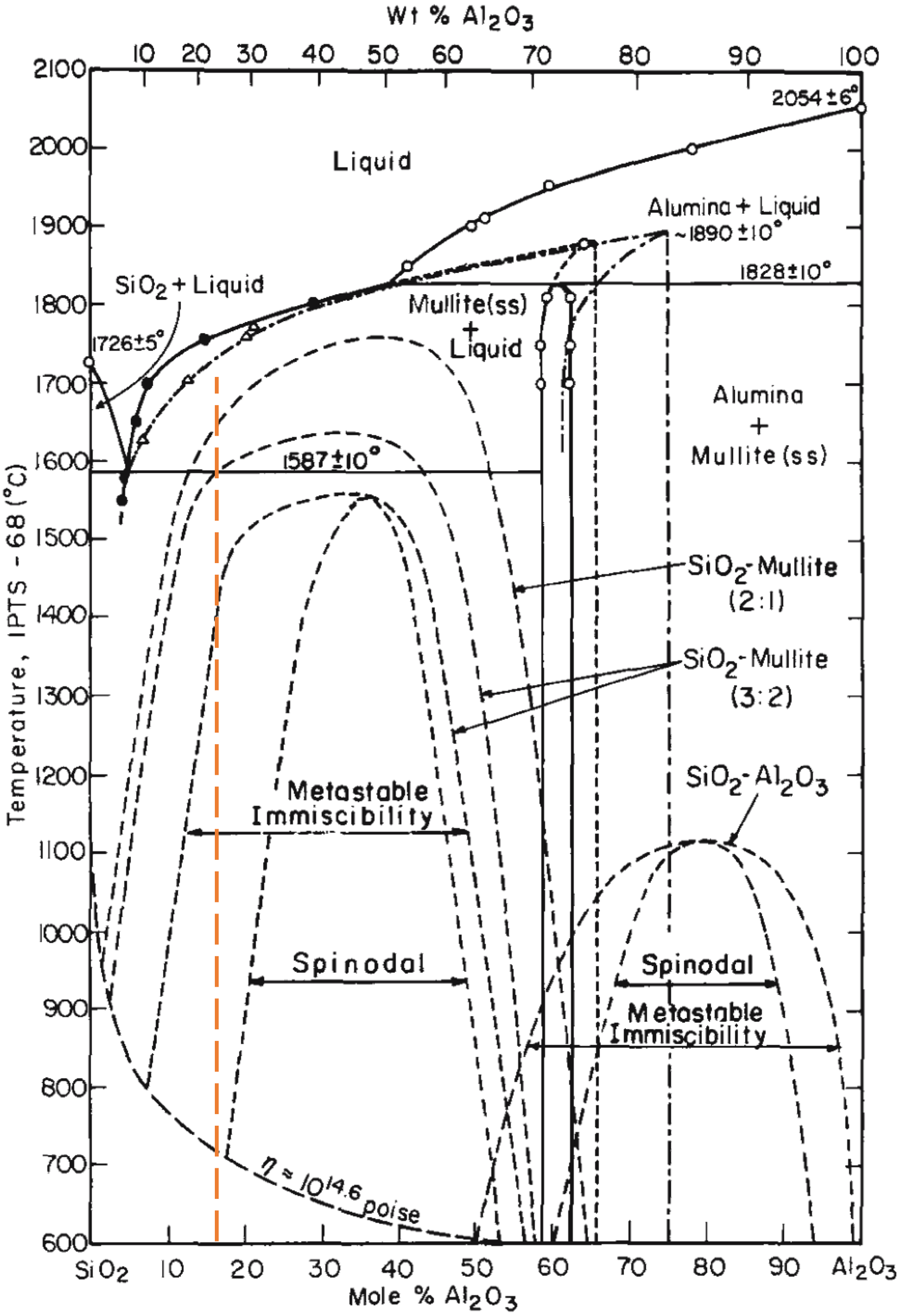

Figure 64. The thermodynamically metastable, spinodal and immiscibility region in Al_2O_3-SiO_2 system. The Al_2O_3 molar concentration is equivalent to 16.7 % in the phase diagram for our SAL glass composition which is marked with the red vertical dashed line. [104].

quantity (10 x La_2O_3), generating in sum 60+ in charge. Therefore it takes 12 $AlO^-_{4/2}$ tetrahedra (6 x Al_2O_3) to neutralize La^{3+}. Since there are 10 mol% La_2O_3 and 6 mol% of the Al_2O_3 that are required to be detached from the glass network, the SAL glass composition can be rewritten to (70 SiO_2 -14 Al_2O_3) (6 Al_2O_3 -10 La_2O_3). The Al_2O_3

concentration is then 14/(14+70)=16.6 mol% in Al_2O_3-SiO_2 phase diagram which has been marked by the red dashed line (see Figure 64). The red dashed line is located in the metastable immiscibility region at temperatures below 1400 °C. In the next section, it will be shown that 1400 °C is a critical temperature for the opaque/transparent transition of the GPWS SAL glasses.

6.2.3 Crystallization temperature of Mullite

A series of 5min GPWS SAL glass samples has been prepared at temperatures ranging from 1050 °C to 1550 °C to investigate the crystallization temperature. Mullite dots and bars were first observed obviously at 1200 °C in microscopy. Figure 65 shows a comparison of dark field microscopy from two GPWS SAL glass samples sintered at 1175 °C and 1200 °C for 5 min at 50 bar. Since the refractive index of Mullite is about 1.642[106] (> 1.598 for SAL glass matrix at 633 nm), the Mullite bars and dots are distinct from the matrix and can be observed in microscopy.

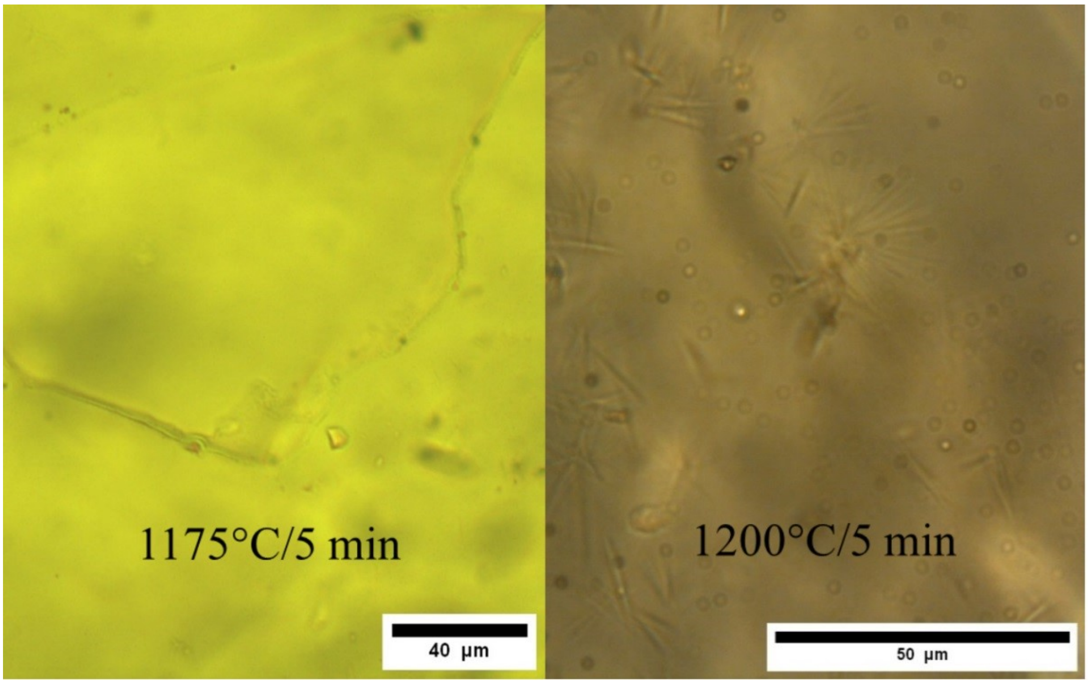

Figure 65. Dark-field Microscopy of GPS-SAL glass sintered at 1175 °C (HIP08) and 1200 °C (HIP02) for 5 min at 50 bar Argon.

Similar observations can be made in microscopy from glass samples sintered at 1250 °C, 1300 °C and 1350 °C with different number densities. The maximum number density appears at the sample sintered at 1300 °C as shown in Figure 66. At 1400 °C, 1500 °C and 1550 °C these bars and dots are no more visible under microscopy (not demonstrated here). Figure 67 shows the BSE micrographs of polished a GPWS SAL glasses sintered at 1350 °C and 1400 °C for 5 min at 50 bar. If 1200 °C is the

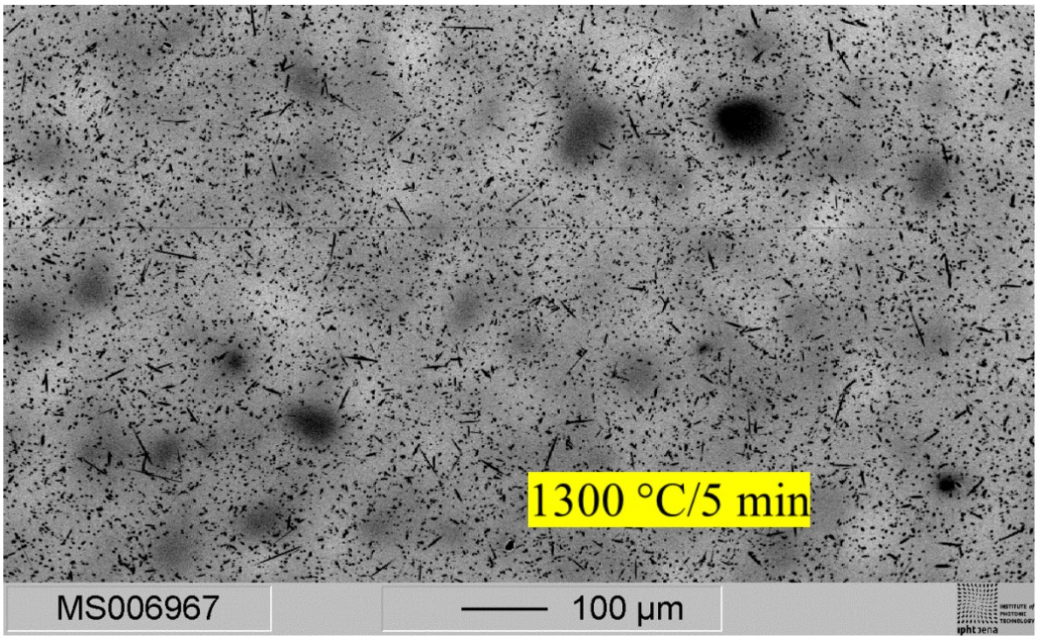

Figure 66. Back-scattered Electron micrograph (BSE) of GPS-SAL glass (HIP12) sintered at 1300 °C for 5 min at 50 bar Argon.

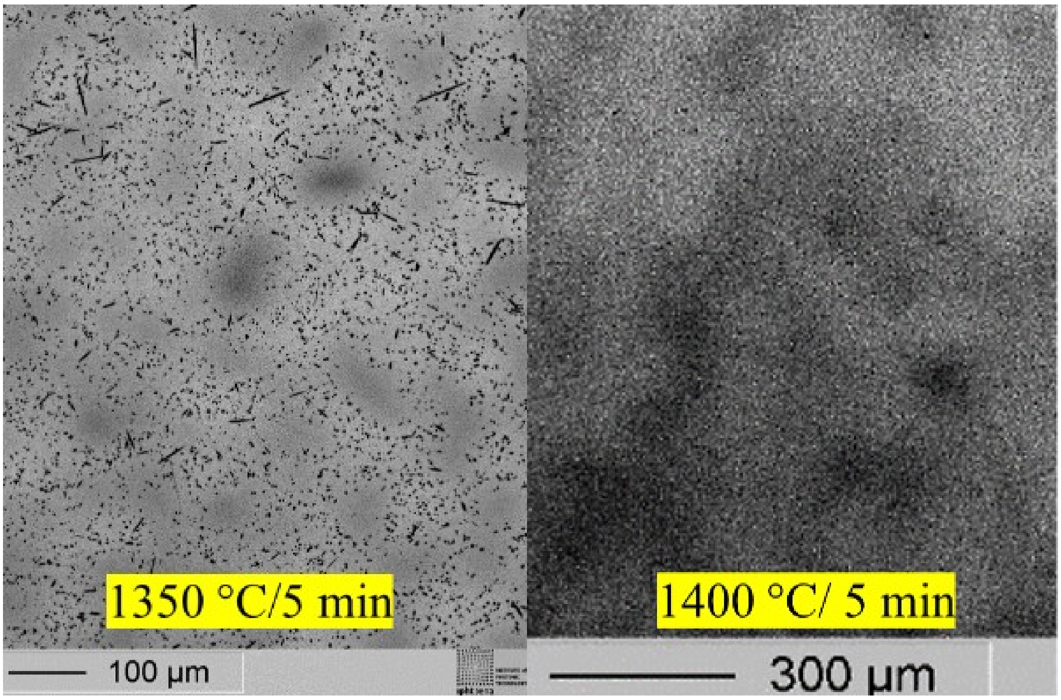

Figure 67. Back-scattered Electron micrograph (BSE) of GPS-SAL glass sintered at 1350 °C (HIP13) and 1400 °C (HIP14) for 5 min at 50 bar Argon.

temperature for the beginning of Mullite crystallization, 1400 °C should be the ending temperature. Therefore, from the BSE and optical microscopic images, 1200 °C to 1400 °C seems to be the crystallization temperature range for Mullite in SAL glass. This conclusion has been confirmed by the density measurement of the same serials of GPWS SAL glasses as demonstrated in Figure 68. The densities increase initially

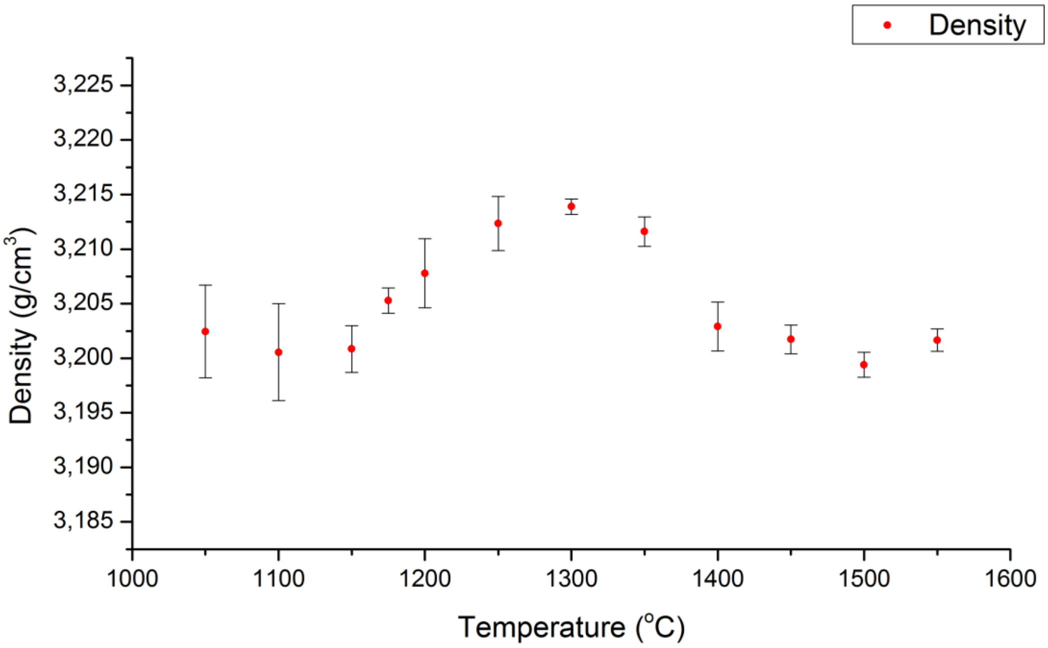

Figure 68 .Density of GPS-SAL glass samples (HIP01-02, 56-09, 12-17) sintered at different temperatures for 5 min at 50 bar Argon.

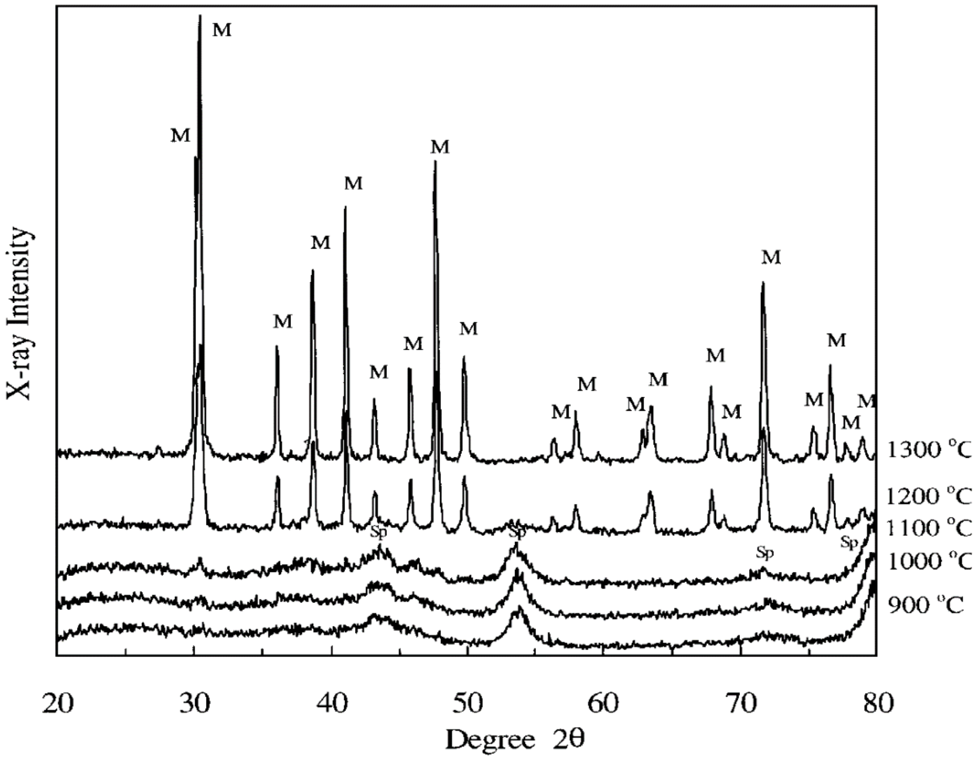

Figure 69. XRD of sol-gel prepared Mullite at different temperatures from 900°C to 1300°C. M is Mullite and Sp is γ – Al_2O_3 spinel [107].

at 1200 °C, achieving a maximum at around 1300 °C and returning to the magnitude before 1200 °C again from 1400 °C on. This result also agrees with the XRD study on a sol-gel produced Mullite by Cassidy[107] et al. as shown in Figure 69 in a more sensitive method. In addition, this comparison suggests that the application of 50 bar pressure is so low that there is no risk to change the internal topological structure of the glass. Cassidy[107] has reported that single phase Mullite crystallizes from homogenous gels at 980 °C. Figure 70 shows BSE images of an extreme long vacuum sintered SAL glass at 1000 °C (50 hours). Needle-like structures are spreading out from the boundaries (marked with circle dashed line). There is no detectable crystalline peak on such glass samples from the XRD pattern due to the too low concentration. Hence the starting temperature of the Mullite crystallization is also time dependent. It occurs earlier at about 1000 °C when the time is enough as depicted in the XRD study from Cassidy[107].

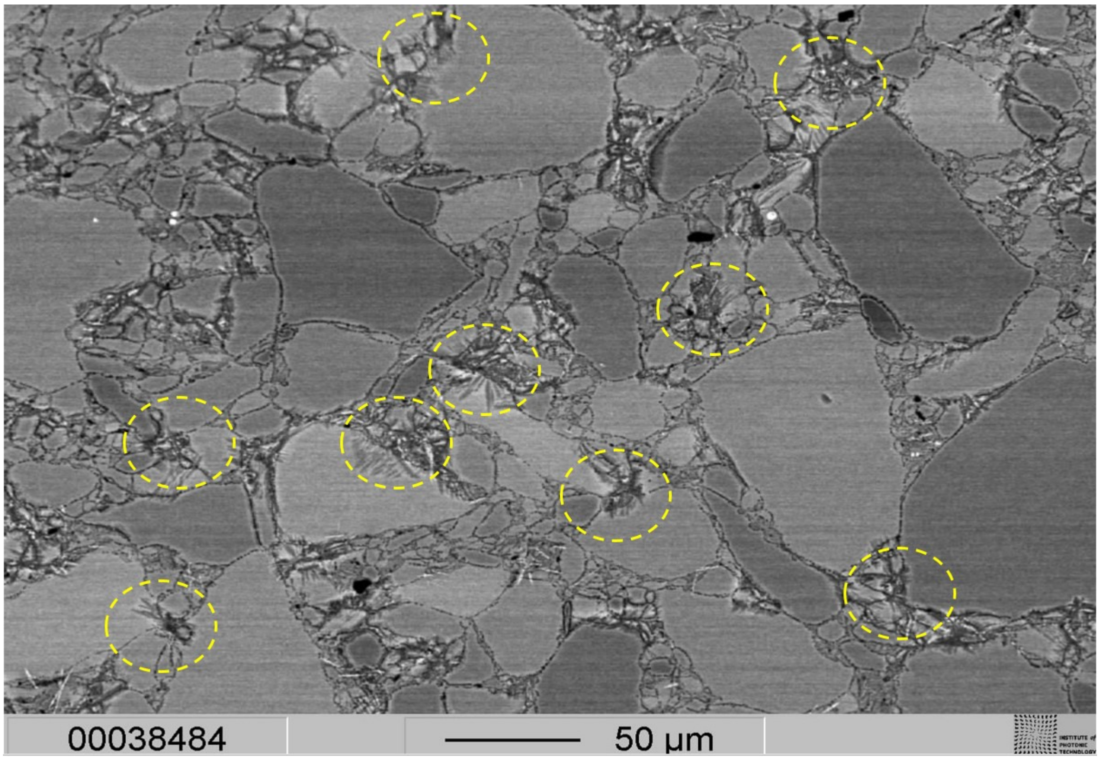

Figure 70. BSE micrograph of polished SAL (VSR02) glass sintered at 1000 °C for 50 hours in vacuum. The yellow dashed line marks the position of needles like Mullite structure.

6.2.4 *Source of Mullite crystallization*

In previous section Mullite crystallizations are found initial at the boundaries. The location of the Mullites indicates that the source of crystallization should be located on the boundary. Baghshahi[108] et al. reported in a similar (Nd_2O_3 - Al_2O_3 - SiO_2) ternary glass system that crystallization occurs from the surface to the bulk. They stated that the surface crystallization begins at 1000 °C and that the crystal growth rate increases with decreasing Si : RE and Si : Al ratios, since the boundaries are a kind of interface or

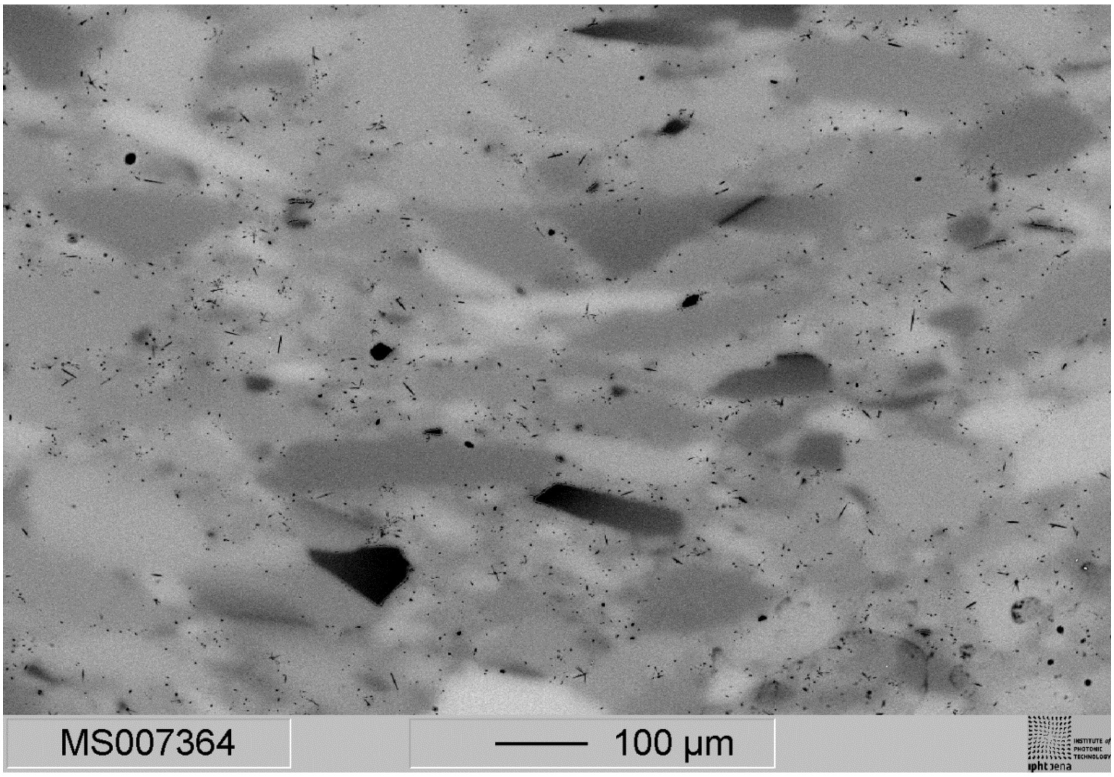

Figure 71. BSE micrograph of polished GPS-SAL glass (HIP02) sintered at 1200 °C for 5 min at 50 bar Argon.

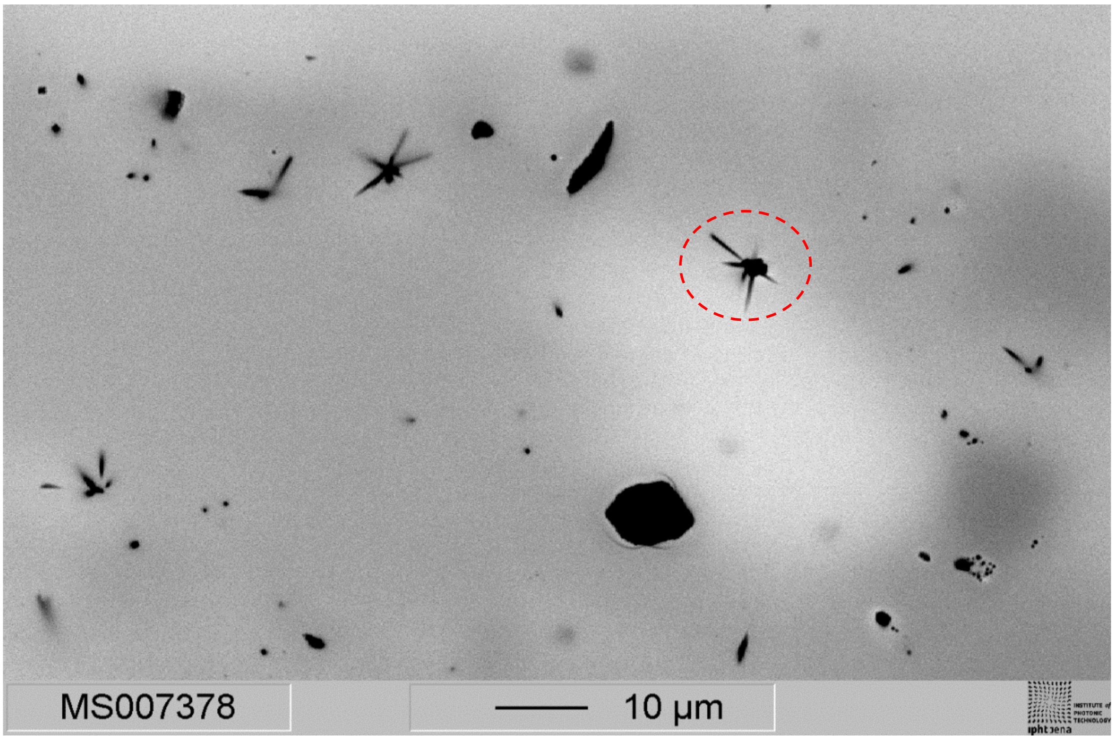

Figure 72. Mullite grows from the silicon-rich particles distributed along the grain boundaries of GPS-SAL glass sample sintered at 1175 °C for 5 min at 50 bar. The red circle marks the crystallization that is faster towards La rich region (bright), where Si : RE ratio is low.

defects. Figure 71 shows a BSE microscopic image of a GPWS SAL glass sample sintered at 1200 °C for 5min. This image is able to provide the initial state of Mullite crystallization as discussed in the previous section. The Mullite seems to grow from the silica rich bumps. In an enlarged BSE image (Figure 72) of the same sample, the growth of needle-like Mullite occurs from the silica rich bumps that are distributed along the boundaries. These bumps serve as nuclei for crystallization and they seem to be the primary source of Mullite crystallization. Furthermore, the growth rate of Mullite is higher towards the brighter region in BSE microscopic image (red circle in Figure 72) where the rare earth element concentration (La) is rich. This tendency agrees to the conclusion from Baghshahi[108] mentioned above because the brighter region in BSE microscopic image has lower Si : RE ratio. This can be confirmed by BSE microscopic image on a GPWS SAL sample sintered at 1200 °C for 5 min as in Figure 73.

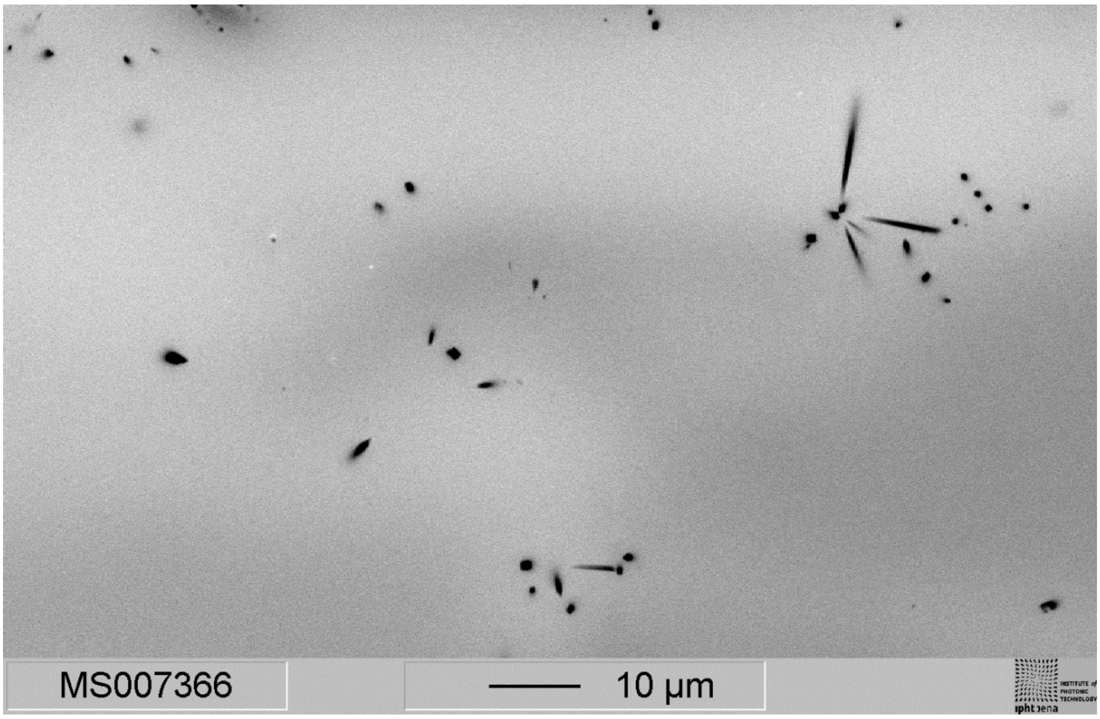

Figure 73. BSE micrograph of GPWS SAL glass (HIP02) sintered at 1200° C for 5 min in 50bar. The Mullite crystals grow preferably into the La rich region (bright region).

6.2.5 *Other crystallization phase*

Figure 74 shows the XRD diagram of a SAL glass sintered at 1100 °C in vacuum for a dwelling time of 2 hours. For such a long dwelling time cristobalite and $LaAlSiO_5$ were found other than Mullite.

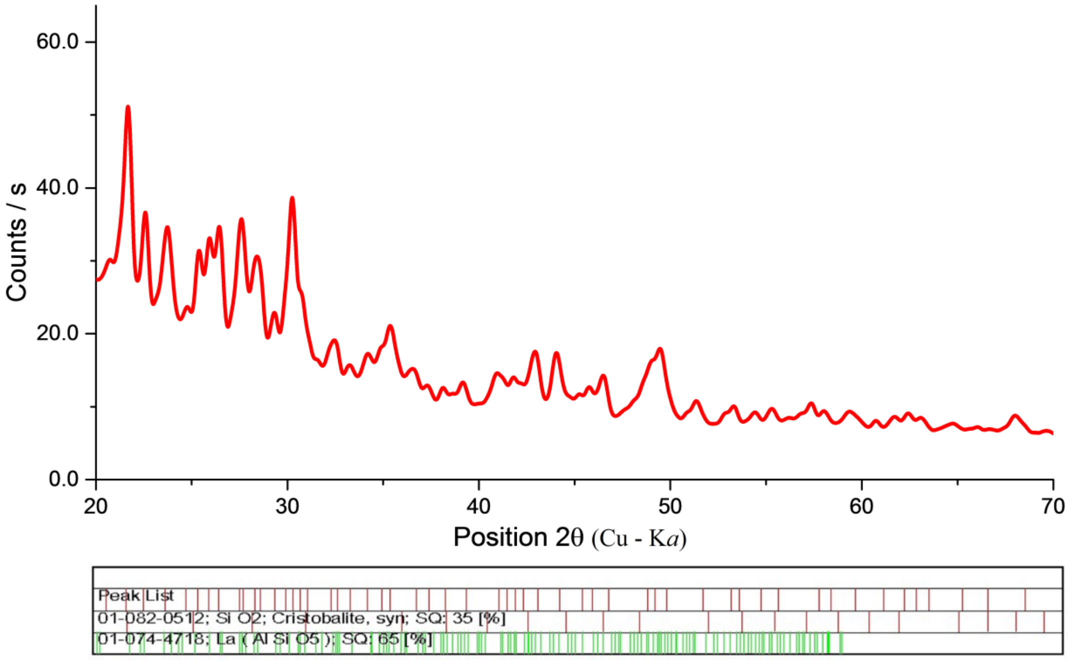

Figure 74. XRD pattern of SAL glass (VSR01) sintered at 1100 °C for 2 hours in vacuum.

6.2.6 Summary for crystallization

To summarize the crystallization effect, three kinds of crystalline phases have been observed. At temperatures between 1200 °C and 1400 °C 3 : 2 - Mullite crystallized for fast sintering in 5 min. According to the needle-like shape in BSE (Figure 70, Figure 72 and Figure 73) images, the source of the Mullite is the silica rich bumps as impurities on the grain boundary. Therefore, pure silica grains should be regarded as impurities (defects), because they make the sintered SAL glass opaque at temperature below 1200 °C and induce crystallization of Mullite at 1200 °C to 1400 °C. In addition, plenty amounts of cristobalite and lanthanum aluminosilicate ($LaAlSiO_5$) are detected on GPWS SAL glasses sintered for more than 2 hours at 1100 °C.

6.3 Knots

GPWS SAL glass sintered above 1400 °C turns out to be transparent although silica/quartz grains inclusions are present. However, it might still contain inhomogeneities such as knots, which arise from glassy phase inclusions or phase separations during heat treatment. These knots result in scattering losses. Large glassy inclusions could be easily distinguished by microscopy while very fine glassy phase arising from phase separation will be difficult to discover. For the latter case, etching with diluted hydrofluoric acid (HF) solution can be applied to reveal that very fine structure in the glass matrix, which is normally invisible in microscopy or in Atomic Force Microscopy (AFM).

6.3.1 Glassy inclusions

Figure 75 shows two 60 µm glassy inclusions in dark-field microscopy at GPWS SAL glasses sintered at 1400 °C and 1550 °C, respectively. These inclusions probably come from the "unmelted" silica-rich particles from the starting material. They disappear at higher temperatures or in longer dwelling times. The population of these knots varies strongly with temperature, e.g. only one inclusion has been found at a 13 mm in diameter and 1 mm thick GPWS SAL slice sintered at 1550 °C for 2 min while tens of knots were found in one sample (Figure 75 left) sintered at 1400 °C for 5 min. The minimum dwelling time at 1400 °C is found to be 1 hour while it is 2 min at 1500 °C for the elimination of large unmelted silica rich knots. Figure 76 shows one microscopy image of HIP13 sintered at 1350 °C. From both the population and size, this kind of knots are not problematic.

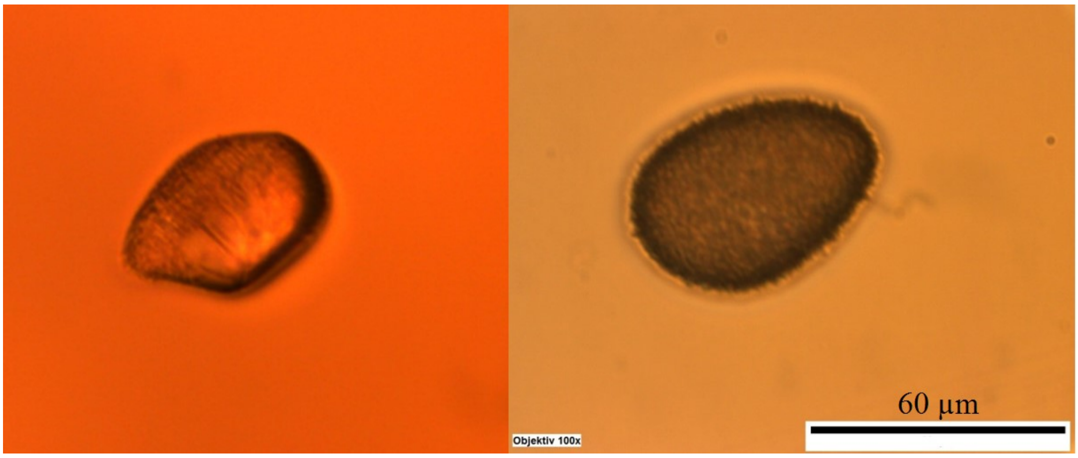

Figure 75. Dark-field Microscopy of polished GPWS SAL glasses sintered at 1400°C for 5 min (left) and 1550 °C for 2 min at 50 bar (right). A glassy inclusion of about 50 µm in diameter has been found.

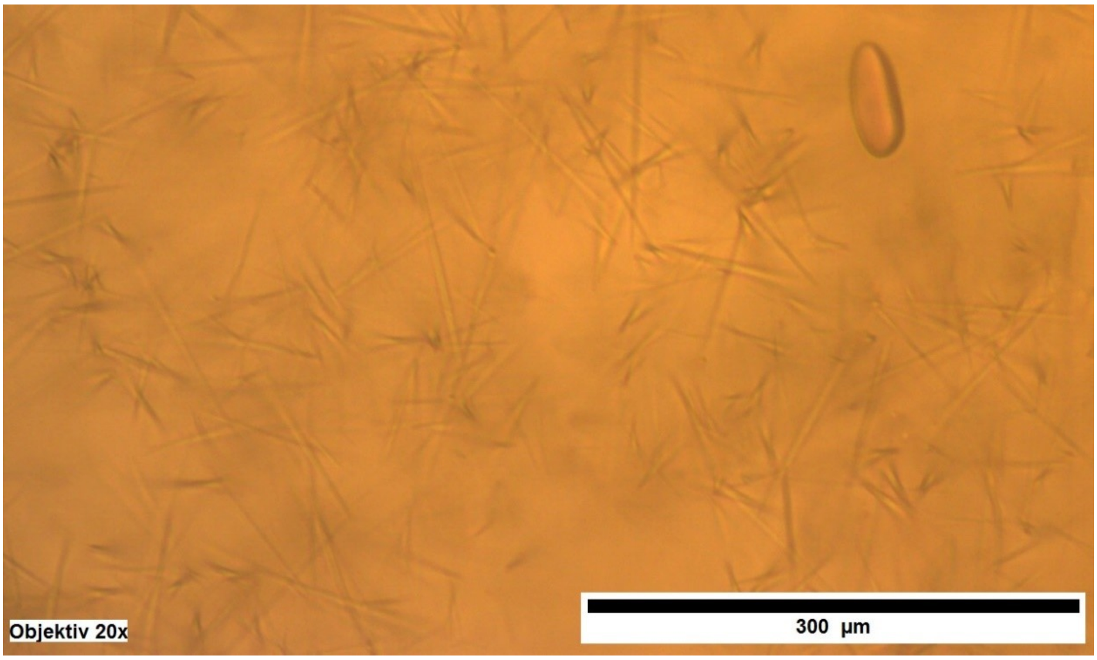

Figure 76. The coexistence of knots and Mullite in GPWS SAL glass sample (HIP13) sintered at 1350 °C for 5 min at 50 bar.

6.3.2 *Phase separation*

Another source for knots is the phase separation. According to the phase diagram in Figure 64, our glass composition is thermodynamically metastable at temperatures from 1400 °C to 1550 °C. Therefore, a long dwelling time will probably induce phase separation. When the dwelling time exceeds the minimum values described in the previous section, the glass seems to be transparent and no obvious inclusions were observed in optical microscopy, SEM, BSE and AFM microscopies. However, attenuation spectra have shown that the GPWS SAL glasses sintered above 1400 °C

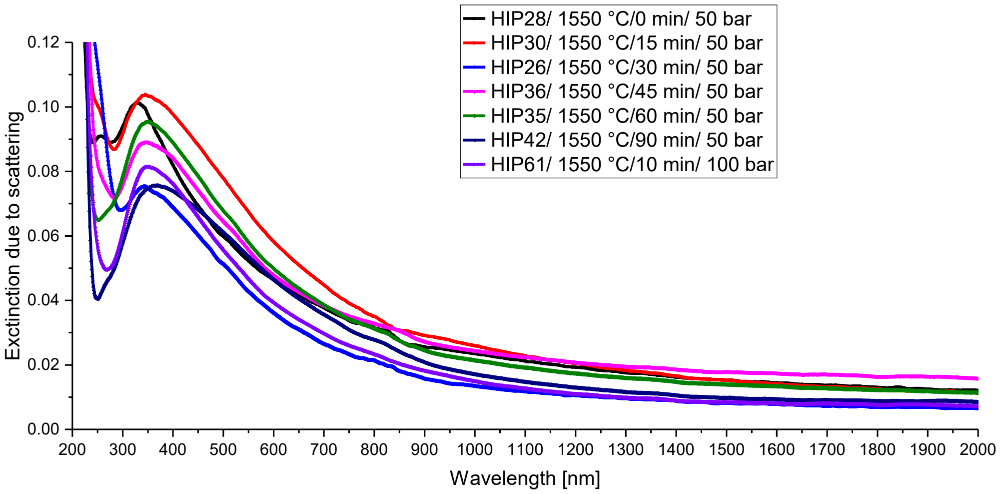

Figure 77. Absorbance spectrum of 1mm polished GPWS SAL glass slices using 1 mm thick starting SAL glass (DL_98) as a reference.

encountered scattering losses (Figure 77). These spectra are purely caused by the scattering losses since a reference of SAL glass with the same thickness has been used. The spectra show additional losses from GPWS SAL glasses near the UV region; their maximum positions are located from 330 nm - 360 nm. These additional losses change the color of SAL glass from colorless to slightly brown under illumination of the sunlight. According to the EDX measurements, no detectable cation is responsible for such color change.

6.3.3 *Fitting with Mie theory*

According to previous studies, silica rich bumps were found embedded in our SAL glass matrix. Therefore, a model has been built using Mie scattering theory[109]: pure silica spheres were assumed embedded in the SAL glass matrix. The calculation of the influence of the silica spheres on UV spectra is carried out in MiePlot 4.0[110]. The intensity of the scattered light (at 0 °) with unpolarised incident plane wave was calculated. It was set that the refractive indices for silica glass spheres is n = 1.459 – 1.467 while the SAL glasses n = 1.590 – 1.601[21]. The calculation range was set from 235 nm to 600 nm. The results are demonstrated in Figure 78 for different sphere sizes. The intensities from 0.1 µm to 5 µm with a step of 0.1 µm are then normalized and extracted to a matrix. By assigning different coefficients to each column of the matrix, the experimental curve was fitted by linear superposition of Mie scattering's curves. Figure 79 demonstrates an instant of fitting one of the GPWS SAL glasses (HIP26). The resulting coefficients, or equivalently the distributions of the size of the scattering spheres in some of the GPWS SAL glasses are demonstrated in Figure 80.

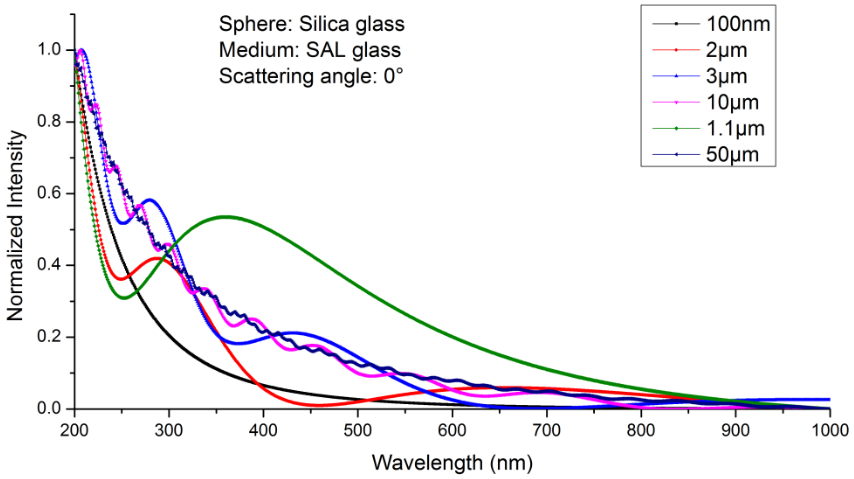

Figure 78. Calculation of Mie Scattering at 0 ° in SAL glass embedded with different radius of quartz spheres.

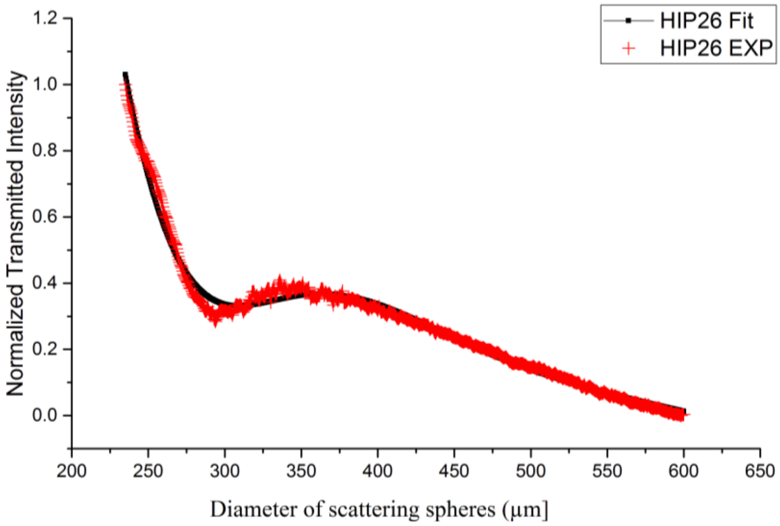

Figure 79. Comparison of normalized intensities between calculated Mie-scattering spectrum and additional losses spectra of GPWS SAL glasses using melting-and-quenching SAL glass as reference.

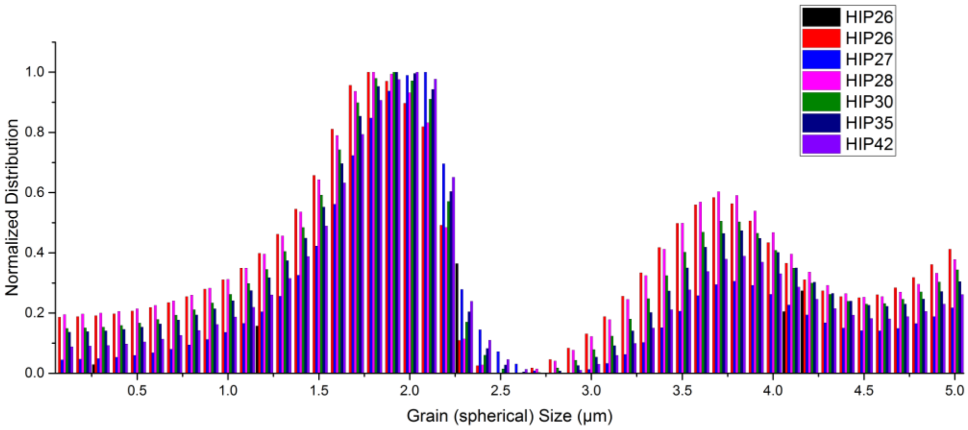

Figure 80. Normalized distributions of different scattering particle sizes (diameter) in GPWS SAL glasses. They are fitted via Mie's scattering theory.

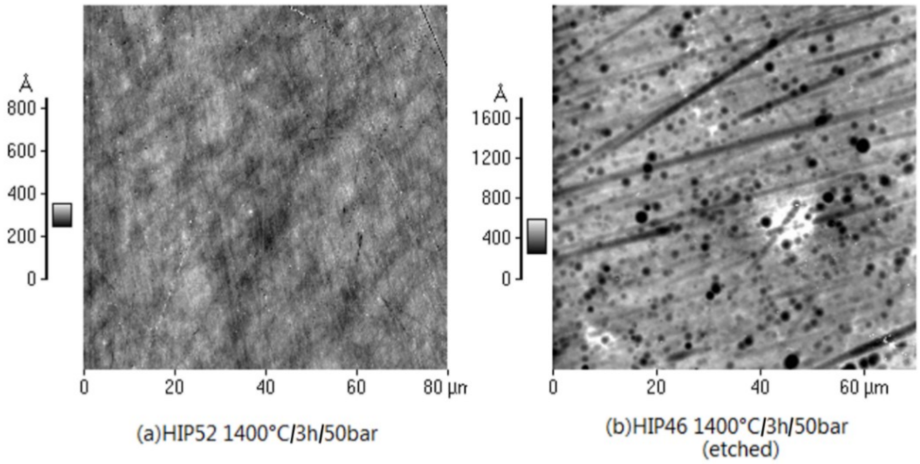

Figure 81. Comparison of etched and normal polished GPWS SAL glasses sintered at 1400 °C by Atomic Force Microscopy (AFM). Spherical concave surfaces are found after etching with diluted HF (5 %) for 10 mins.

Most of the scattering spheres are at 1.5 – 2.0 µm and the other of them are at about 3.5 – 4.0 µm. This size distribution has been confirmed by AFM measurements as shown in Figure 81b, where black spheres in dimensions of 1 – 4 µm are present. This measurement is carried out on a surface of an etched GPWS SAL glass otherwise the surface before etching looks like Figure 81a. Since the near blue range of the visible light has been scattered by these spheres, the scattering behavior explains the fact that GPWS SAL glass looks slightly brown under illumination of sunlight. Figure 82 demonstrates this appearance on the right hand side while another evidence is shown on the left hand side. The green laser beam is scattered in the glass.

Figure 82. GPWS SAL glass (HIP52 1400 °C/1 hour/10 bar) is illuminated by 532 nm laser diode and scatters the green beam. On the right hand side: illumination by sunlight.

It might be intuitively concluded that these silica glass spheres arise from those unmelted agate grains originally in the raw material as reported in previously. However, such a conclusion is contradicted by the observation of their evolution in number densities. Figure 83 shows the evolution of number density depending on temperature and time. It becomes denser at higher temperature with longer dwelling time. This behavior is opposite to the tendency in the case of unmelted grains, which decreases with longer dwelling time at high temperatures. It is also deducible from Figure 83 that the dwelling time for non-scattering GPWS SAL glass preparation should not exceed 30 min at 1550 °C unless scattering glasses are intended.

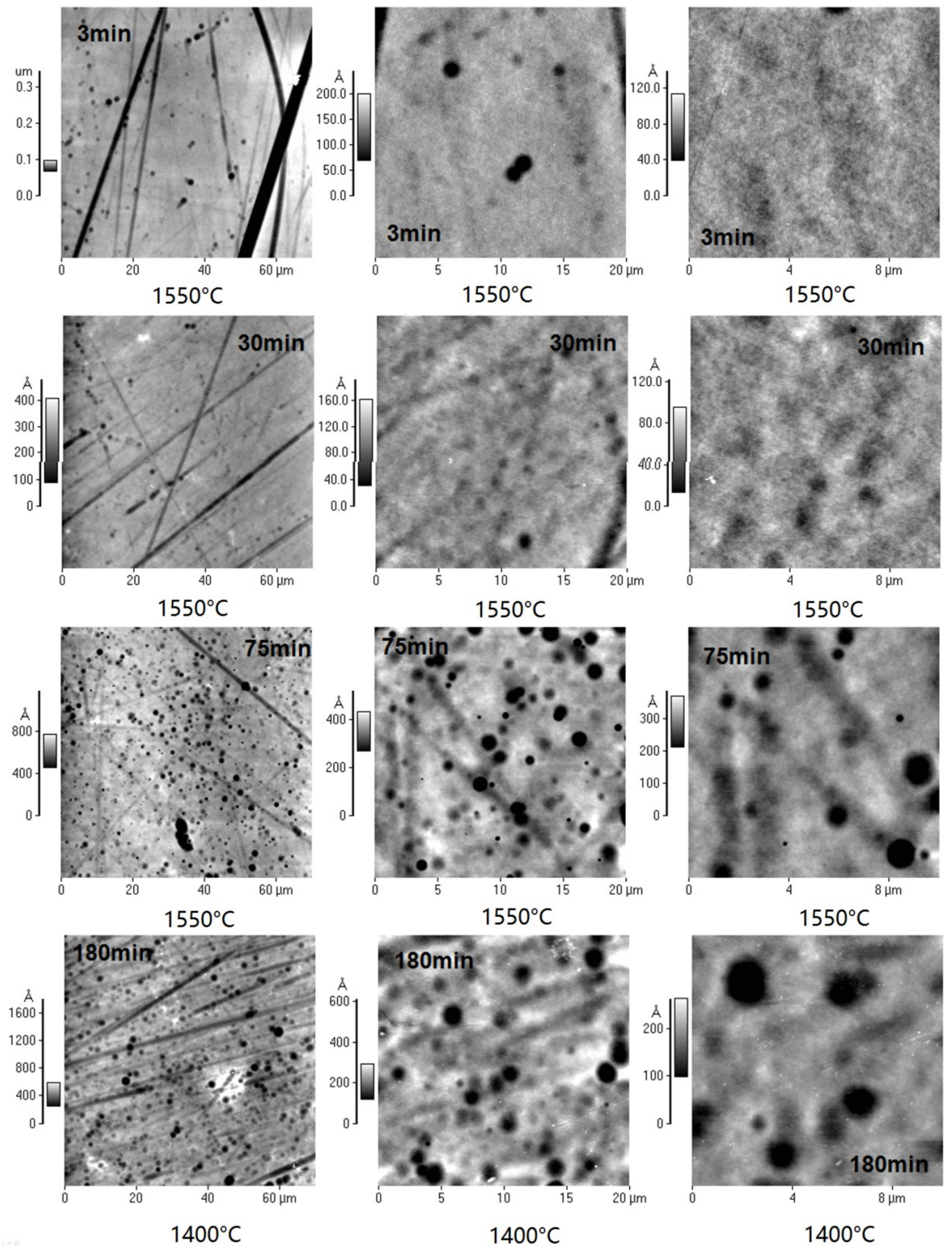

Figure 83. AFM of polished and etched GPWS SAL glass samples sintered at different temperatures and times in 50 bar. 5 % HF is used to etch for 10 min.

6.3.4 *Summary for knots*

In summary, two kinds of glassy inclusions were found in GPWS SAL glass at temperatures between 1400 °C and 1550 °C: unmelted large silica grains and fine silica phase separation. The unmelted silica grains cause negligible attenuations while the phase separation knots because scattering losses at and close to the UV range for GPWS

SAL glasses sintered in this temperature range. Their identities as well as the size distributions have been fitted by Mie's theory and confirmed by AFM microscopy on etched samples. These phase separation knots are responsible for the color change in GPWS SAL glass under sun light as well as the beam scattering observation with green laser. These number density of the phase separation knots will be limited if the dwelling time at 1550°C do not exceed 30 min. A decrease of silica content in our SAL glass composition is proposed in the future work for preparation of non-scattering SAL glasses. Otherwise, scattering SAL glass can be prepared with a dwelling time longer than 75 min at 1550 °C.

6.4 Striae

Striae in glass are another kind of inhomogeneity, which arises from localized fluctuation of refractive index. Such fluctuation is the result of the interaction of compositional inhomogeneities and the convective flow in glass melts, which is driven by the temperature and density gradient in a gravitational field. Especially if the bottom temperature is higher, the fluid parcel at the bottom is brought up by buoyance force due to its lower density while the cooler fluid parcel with higher density falls down. The resistive force to buoyance force for convection is the viscous damping force in the fluid. A dimensionless number termed as Rayleigh number is used to describe the final rate of convection under these two forces:

$$Ra = \frac{\rho g \beta}{\eta a} x^3 \Delta T \qquad (62)$$

where Ra is Rayleigh number, ρ, g, β, η, a, x and ΔT are liquid density, gravitational constant, thermal expansion coefficient, dynamic viscosity, thermal diffusivity, characteristic length and temperature difference, respectively. As Ra value increases, the convection rate becomes higher. For the initiation of the convection movement, the Ra number should exceed a critical value so that the driving force can overcome the viscous damping force.

6.4.1 Striae patterns

Striae are usually eliminated effectively by stirring. According to Jensen and Yue's simulation[111] (Figure 84), stirring deforms striae in the glass melt and creates the stream-like patterns according to the trajectory of the stirring flow. During this process, the stirring perturbation broadens the distribution of the thickness of the striae, which is defined as shown in Figure 84A. As a result the striae are being converted into thicker and thinner ones as shown in Figure 84B, C and D, respectively. Those thinner striae are eliminated faster than the thicker ones via the diffusion while the broadened striae take longer time to eliminate. Therefore, the total number of striae decreases or are eliminated with time. This explains the physical origin of the acceleration of homogenizing effect by stirring in the glass melt. Convection can be considered as another kind of "stirring" movement driven by the temperature

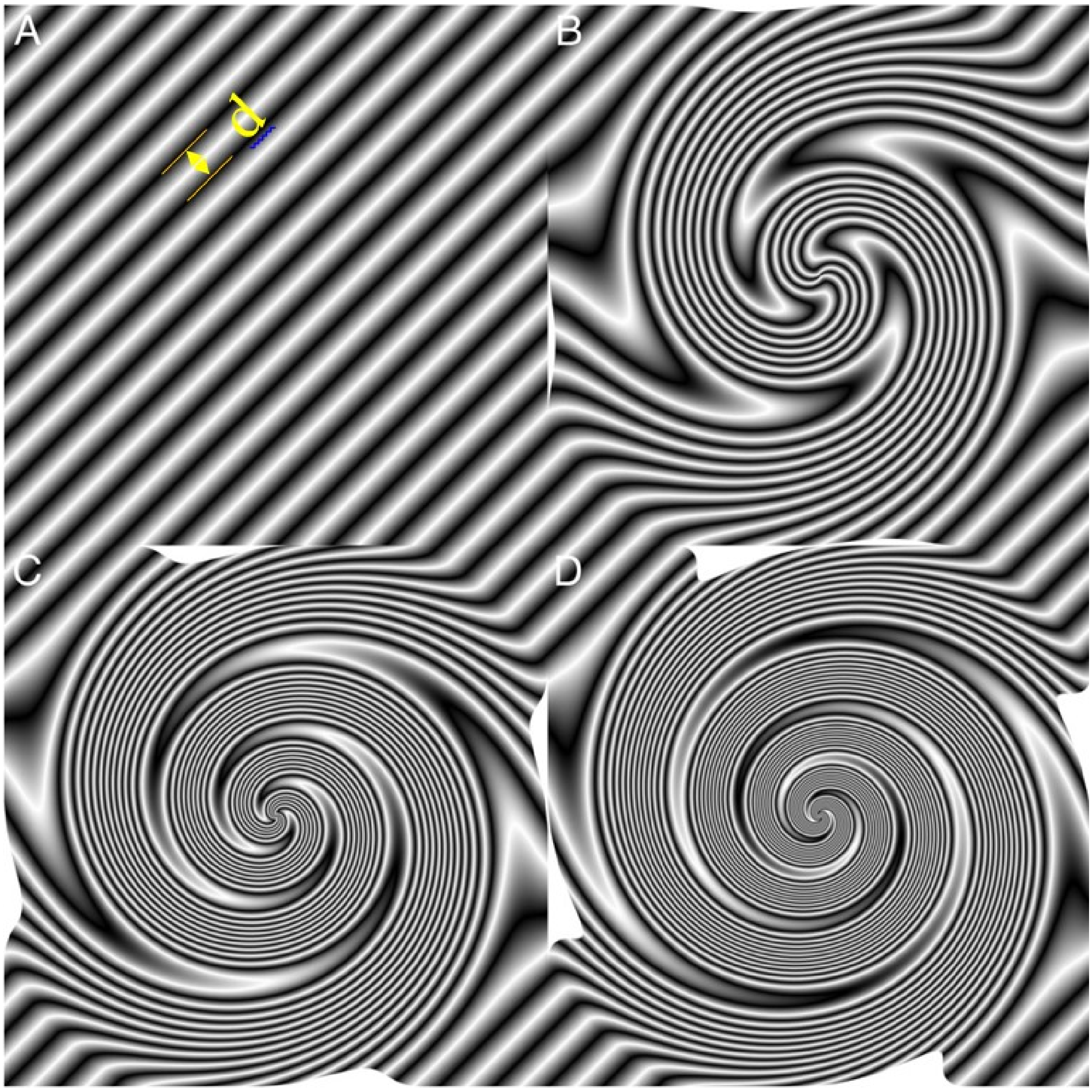

Figure 84. Images of simulated striae patterns after 360°, 720° and 1080° striation in B, C and D, respectively. The initial pattern is shown in A and the size of striae is defined as d, the thickness of the striae [111].

and density gradient instead of stirrer. Figure 85 shows the evolution of the striae patterns from GPWS SAL glasses sintered at 1550 °C at 50 bar for different times. The initial state is shown in Figure 85a, where random patterns appear due to the poor homogeneity in co-dopant concentrations. These random patterns are firstly homogenized via the diffusion as concluded in the FEM Simulations results. They become gradually blurred with increasing the dwelling time (Figure 85 b-c) due to the fact that the gradient of refractive index is reduced. In addition, the striae patterns become more and more stream like instead of random patterns. In Figure 85 d-f, the striae patterns demonstrate a strong stream-like fashion. This evolution agrees to the previous FEM Simulations results. As predicted in the FEM Simulation, the mean

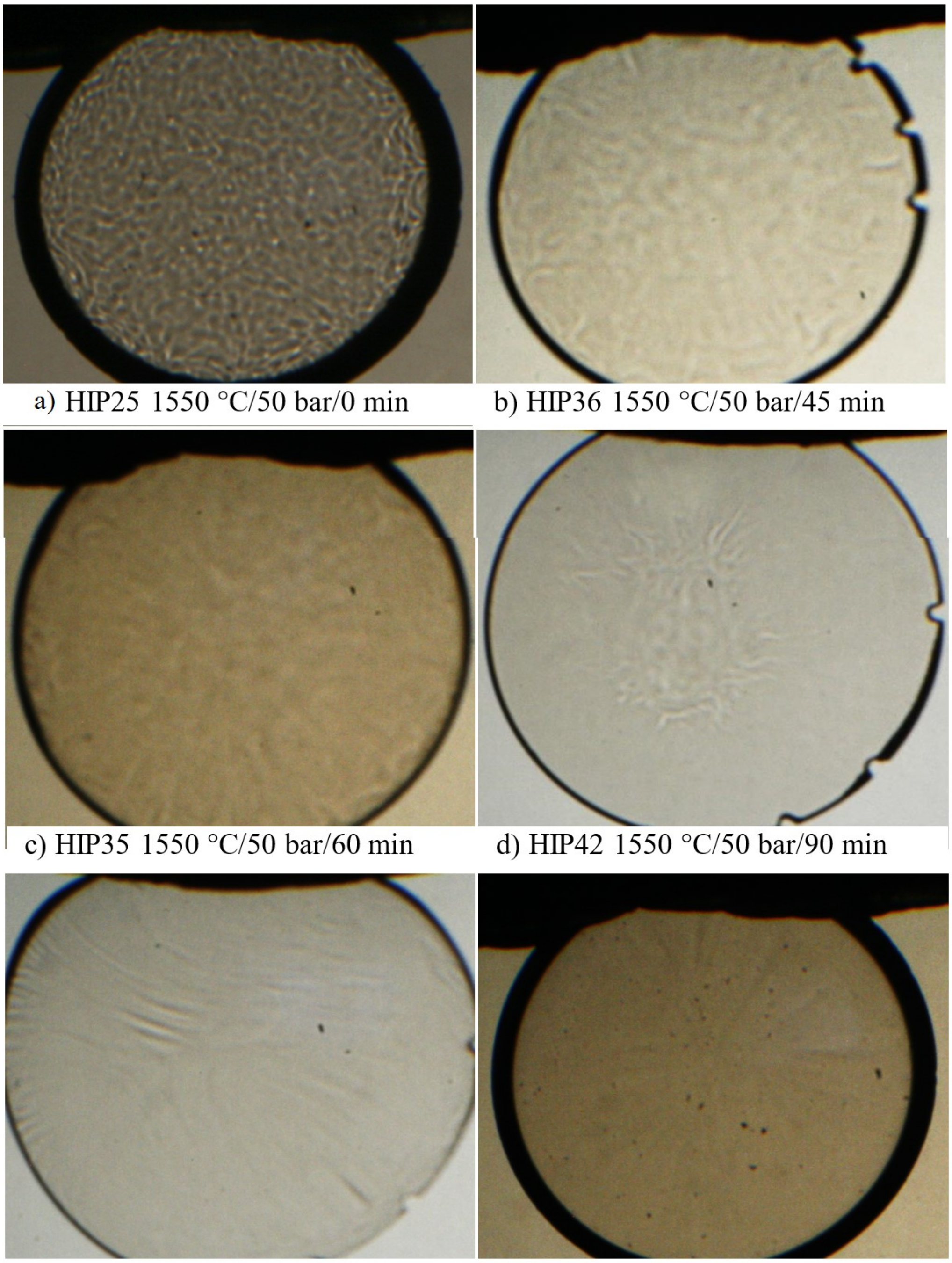
a) HIP25 1550 °C/50 bar/0 min b) HIP36 1550 °C/50 bar/45 min

c) HIP35 1550 °C/50 bar/60 min d) HIP42 1550 °C/50 bar/90 min

e) HIP43 1550 °C/50 bar/105 min f) HIP27 1550 °C/50 bar/120 min

Figure 85. Evolution of refractive index fluctuation for GPWS SAL glass samples sintered at 1550 °C/50 bar for different times. Pictures are taken under illumination of collimated light.

difference of the refractive index has already been reduced significantly, however the convection flow generates shear strain so that a local gradient is generated on the edge of the convection stream. Even these thin striae are fast to diffuse, the convection flow never stops until the Rayleigh number becomes lower than the critical value. Therefore, there are always sharp stream like striae. Figure 38a in the simulation section shows the sharp and random fluctuation pattern on a GPWS SAL glass sample which was sintered at 1400 °C for 1 hour. Comparing to the samples sintered at 1550 °C, only partial patterns are stream-like even for the one sintered for 3 hours. The patterns in this case are mainly formed due to diffusion; therefore, they are usually curl-like. This indicates a high viscosity or low thermal expansion coefficient for the melt. Besides, the effect of pressure on elimination of striae at 1550 °C has also been studied. The results are shown in Figure 86. The striae are independent from external pressure. Therefore, the dominant parameters for elimination of striae are diffusion and viscosity, which can be enhanced at higher temperatures or in longer dwelling times.

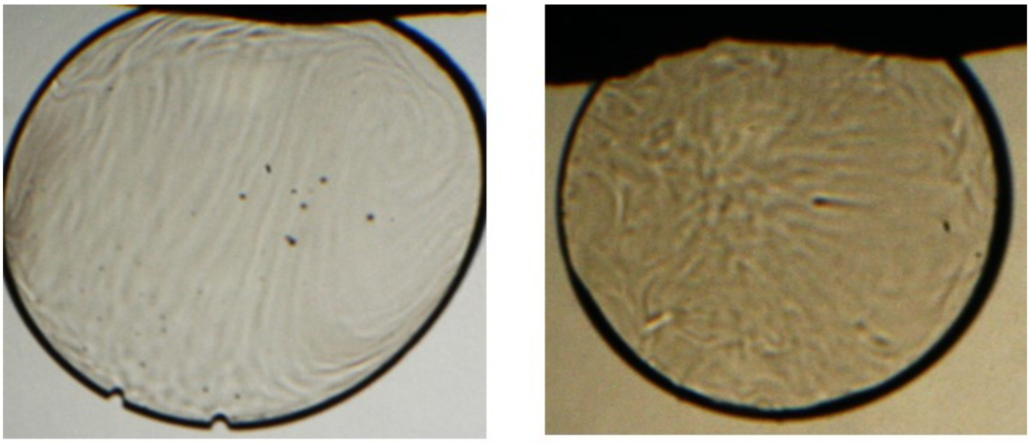

a) HIP41 1550 °C / 5 bar / 30 min b) HIP34 1550 °C / 10 bar / 30 min

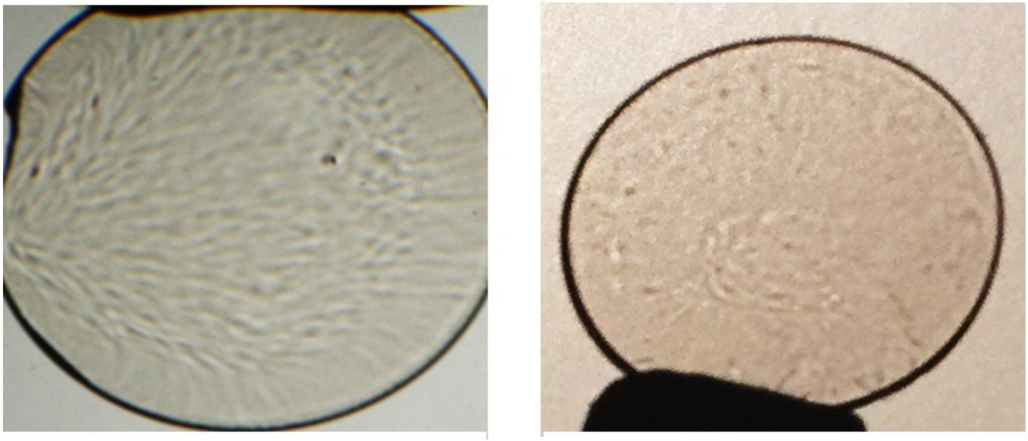

c) HIP44 1550 °C / 50 bar / 30 min d) HIP61 1550 °C / 100 bar / 30 min

Figure 86. Striae at GPWS SAL glasses sintered at 1550 °C for 30 min at different pressures.

6.4.2 *Effect of the striae*

In Figure 85 and Figure 38, it is recognized that two kinds of striae patterns (random pattern and stream like pattern) are developed at GPWS SAL glasses from 1400 °C to 1550 °C. The striae induce additional losses due to scattering of light. The attenuation spectra of those samples in Figure 85 and Figure 38 are shown in Figure 87. Most of

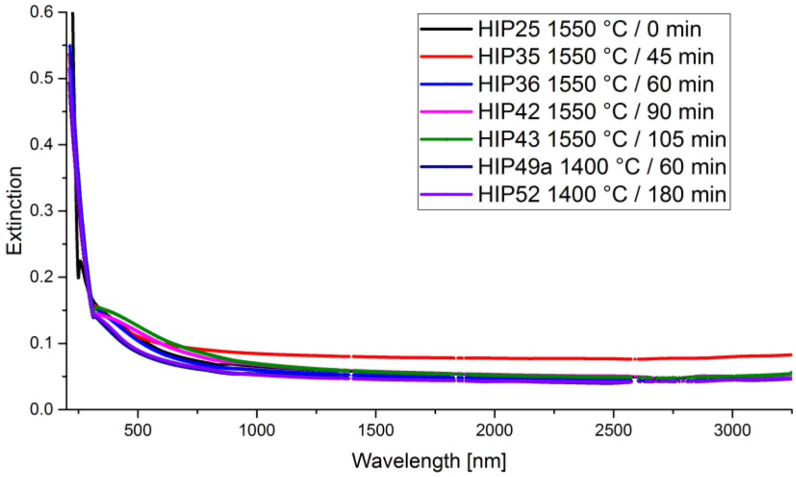

Figure 87. Absorbance spectrum of GPWS SAL glass sintered at 1550 °C for different periods of time with different patterns of refractive index fluctuation.

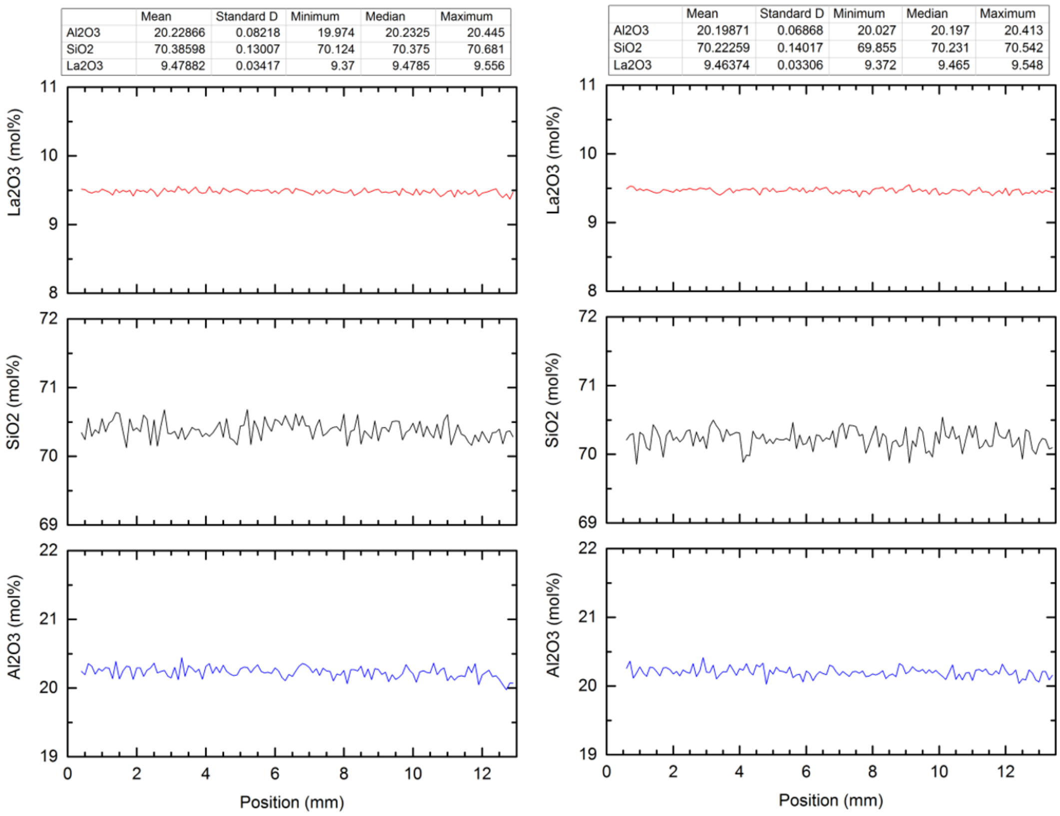

	Mean	Standard D	Minimum	Median	Maximum
Al2O3	20.22866	0.08218	19.974	20.2325	20.445
SiO2	70.38598	0.13007	70.124	70.375	70.681
La2O3	9.47882	0.03417	9.37	9.4785	9.556

	Mean	Standard D	Minimum	Median	Maximum
Al2O3	20.19871	0.06868	20.027	20.197	20.413
SiO2	70.22259	0.14017	69.855	70.231	70.542
La2O3	9.46374	0.03306	9.372	9.465	9.548

HIP36 1550°C/50bar/45min

HIP43 1550°C/50bar/105min

Figure 88. Line scan with EDX for investigation of concentration homogeneity for Al_2O_3, SiO_2 and La_2O_3 respectively.

the spectra exhibit no big differences except for HIP25, which is corresponding to the sample sintered with the smallest dwelling time in Figure 85a. According to the FEM-simulation analysis in chapter 5, Figure 85a has the largest deviation of refractive index due to its shortest dwelling time. The detailed shape of patterns has no significant influence in extinction coefficient. Those distinctive convective patterns shown in Figure 85b-f and Figure 38 are of no big difference. EDX scans have been carried out in GPWS SAL samples. Figure 88 shows the quantitative concentration of each component in our ternary SAL glass for two samples. Both samples (HIP43 and HIP36) are sintered at 1550 °C, with the dwelling times of 105 min and 45 min, respectively, showing similar results in fluctuation of concentration. Table **8** shows more results and their fluctuations in refractive index at GPWS SAL glasses at different working conditions. The largest fluctuation of refractive index and the similar fluctuations from the other samples explain the spectra in Figure 87. All these results together suggest a very slow homogenizing process at 1550 °C after 30 min for the final small fluctuations. This implies the convective flow hinders the homogenization process of the final concentration differences.

Table 8. Quantitative fluctuations in refractive index due to compositional fluctuation in samples.

Sample	Temperature	Pressure	Time	Standard deviation Al_2O_3	Standard deviation SiO_2	Standard deviation La_2O_3	Fluctuation in Refractive Index
	°C	bar	min	mol%	mol%	mol%	x10^{-4}
HIP11	1100	100	30	0.14216	0.64297	0.28140	31.00
HIP49a	1400	10	60	0.07255	0.10063	0.02951	5.09
HIP52	1400	50	180	0.05247	0.06398	0.01505	3.09
HIP41	1550	5	30	0.06967	0.14553	0.03307	5.34
HIP34	1550	10	30	0.07239	0.15506	0.03478	5.59
HIP25	1550	50	0	0.37333	0.32589	0.13401	24.54
HIP44	1550	50	30	0.07818	0.18479	0.03164	5.48
HIP36	1550	50	45	0.08218	0.13007	0.03417	5.84
HIP35	1550	50	60	0.06651	0.16082	0.03630	5.54
HIP43	1550	50	105	0.06868	0.14017	0.03306	5.31

6.4.3 Summary for striae

Finally, the striae patterns have been developed from random patterns to stream-like patterns. It reflects the concurrence of the macroscopic convection movement of the glass melt and the microscopic diffusion of the network modifier. Attenuation measurements were carried out on samples sintered at 1400 °C to 1550 °C in which the magnitude of concentration (refractive index) fluctuation determines the level of scattering losses. The homogenization at the very end seems to be hindered by the convection flow in the melt. This suggests a better temperature homogeneity is required, especially for glass melts with large thermal expansion coefficient.

6.5 Absorption groups

If metallic ions from Fe, Mn, Cu, Ni, Co, etc., are introduced into glass from metal tools, refractory material, batch contamination or even reduction processes, they can change the color of the glass due to the absorption in the visible wavelength range. Other absorption groups in the UV or IR range also lead to losses of passing light.

6.5.1 Elimination of OH groups

As $Al(OH)_3$ has been used as raw material in preparing SAL glass melt before fritting as well as the adsorbed water from the environment, the OH bands are natively contained in the starting SAL glass powder. This has been demonstrated in absorption spectrum of melting-and-quenching SAL glass slices as shown in Figure 89, where an absorption peak has been found near 3500 cm^{-1}. As reported by Suzuki ^{112} and Tomozawa^{113}, absorption bands of OH groups in silicate glasses can be found from 2650 cm^{-1} to 3750 cm^{-1}, which are categorized primary to the "free" OH groups (weakly associated), and the "bonded" OH groups, respectively. These vibration groups arise from O – H vibration and vary at such broad wavelength range due to their local environments. For example, according to Tomozawa^{113}, the H-bridging bonds can weaken the O – H vibration when they are attached. Therefore, those absorption bands with small wavenumbers correspond to the "free" OH weakened by the surrounding H-bridging bonds while the large wavenumber peaks are caused by the "isolated" or

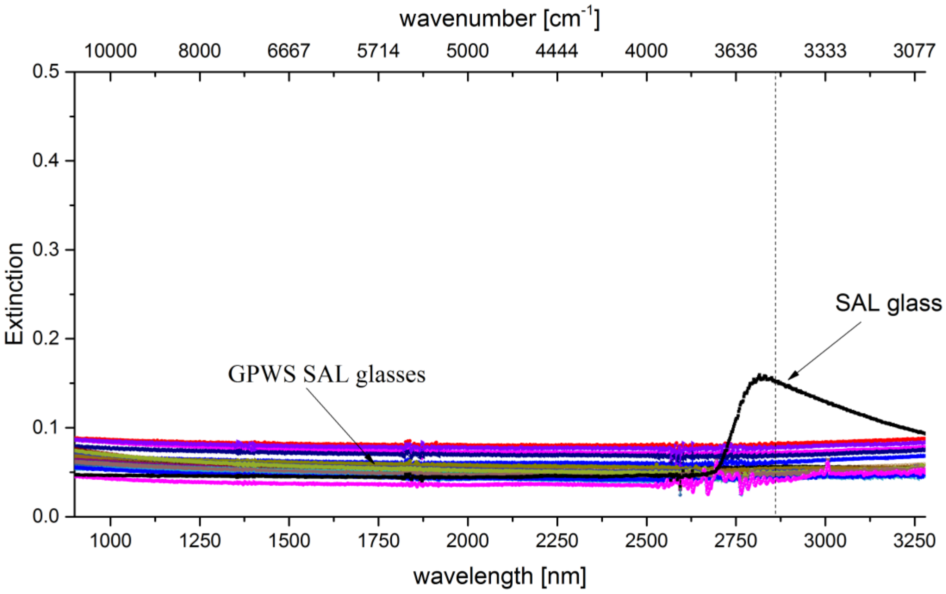

Figure 89. Absorption spectrum of GPWS SAL glasses sintered between 1400 °C and 1550 °C and the SAL glass as starting material. The absorption band at around 2800 nm in starting SAL glass has been eliminated by GPWS. Sample thickness: 1.0 mm. Reference: air.

"bonded" OH groups. Since the glass powders have been dried at 1000 °C for 1 hour in P1, the absorption peak from absorbed water[118] at 1610 $\mathrm{cm^{-1}}$ was not measured.

Scholze[114] has correlated experimentally the concentration of water to extinction coefficient in their IR spectra via water partial pressure measurements. The resulting coefficient is termed the practical extinction coefficient ε, with which the OH concentration can be obtained by Eq. (63)

$$C_{OH} = \frac{1}{d}\left(\frac{A_{3500} - A_{4000}}{\varepsilon_{3500}} + \frac{4}{3}\frac{A_{2800} - A_{4000}}{\varepsilon_{2800}}\right) \tag{63}$$

where d is the thickness of the sample in IR measurement, A_{2800}, A_{3500} and A_{4000} are the absorbance at 2800 $\mathrm{cm^{-1}}$, 3500 $\mathrm{cm^{-1}}$ and 4000 $\mathrm{cm^{-1}}$, respectively. ε_{2800} and ε_{3500} are the practical extinction coefficient at 2800 $\mathrm{cm^{-1}}$ and 3500 $\mathrm{cm^{-1}}$, respectively. The value of ε for aluminosilicate glasses has been reported[115,116, 119] to be within 52 – 80 ($\mathrm{l \cdot mol^{-1} \cdot cm^{-1}}$) according to different compositions. Using ε values in such interval, the range of concentration of OH in the starting SAL glass (Figure 89) can be estimated to be 0.013 – 0.020 mol/l. In the glass batch (556.9 g) for starting powder, 164.2 g $\mathrm{Al(OH)_3}$ has been used for our SAL glass composition. Using the density from Figure 68, the water concentration was theoretically initiated at 12.1 mol/l. This implies that 99.8% of the OH was removed in glass melting and only 0.2% remained in the quenched glass powder. Considering the saturated water vapor pressure in air[117]

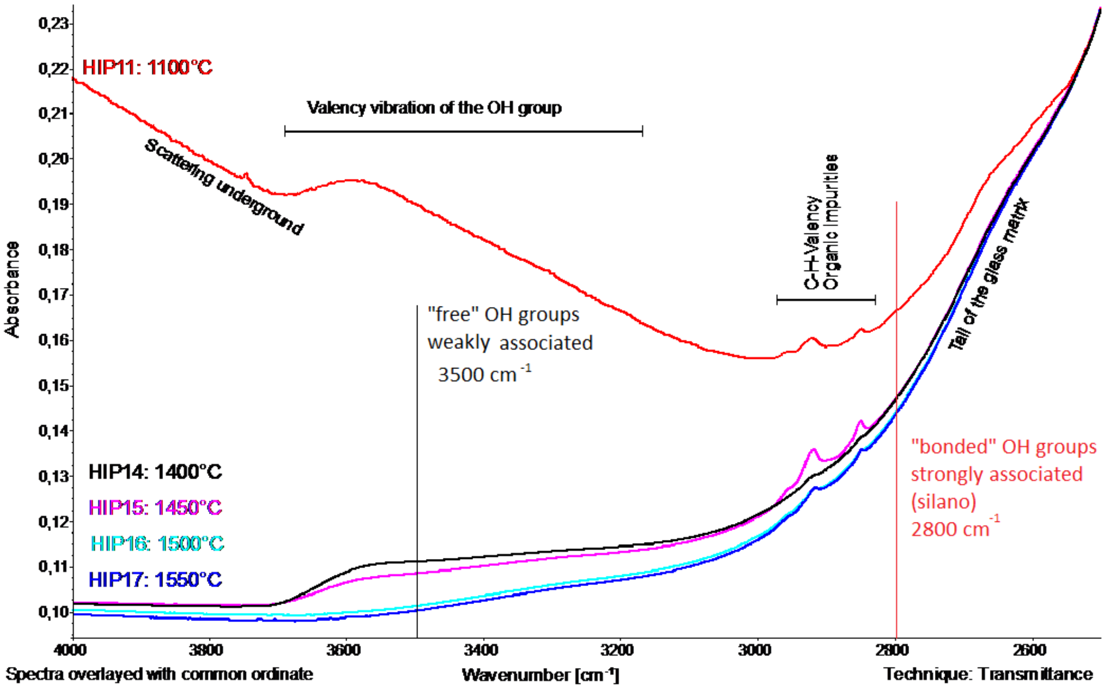

Figure 90. FTIR spectrum of GPWS SAL glass sintered at different temperatures for 5 min at 50 bar. Sample thickness: 1.0 mm. Measured by Dr. Frank Froelich.

between 20 °C (2.339 kPa) to 30 °C (4.246 kPa), the maximum concentration of water in air ranges from 1.9×10^{-3} mol/l to 3.4×10^{-3} mol/l according to the ideal gas law (each H_2O molecule corresponds to two OH groups). These values are one order of magnitude lower than the water concentration in SAL glass. Therefore, the OH in the starting SAL glass powder contributes to both the water contained in the raw material $Al(OH)_3$ as well as the environmental water. This minor amount of water has been efficiently removed after GPWS process at 1400 °C – 1550 °C otherwise is present even in glasses melted at 1650 °C. The degree of OH elimination increases with temperature and this is shown in the FTIR spectra (Figure 90) of GPWS SAL glass samples sintered at temperatures from 1100 °C – 1550 °C for 5 min at 50 bar. However, no “bonded” OH groups (2800 cm^{-1}) are observed from the FTIR spectra. Therefore, the ability of OH elimination demonstrated here is limited to the “free” OH group.

It should be noticed that the La-OH vibration[118] locates at 3580 cm^{-1}, which is close to 3500 cm^{-1}. Kirchhof[119] has demonstrated in a similar Yb doped aluminosilicate glass system that the OH concentration is found remarkably increased in the core region where concentration of Yb is high while the Al content gives no rise to the OH content. The observed weakly associated OH groups in the SAL glasses are probably attached also to Al or the La, which is similar to Yb in the work of Kirchhof.

6.5.2 Reduction of Yb^{3+} to Yb^{2+}

As shown previously Al and La ions in SAL glass are stable even in reduction atmosphere (50 bar argon) at high temperatures reaching 1550 °C, however it is not the

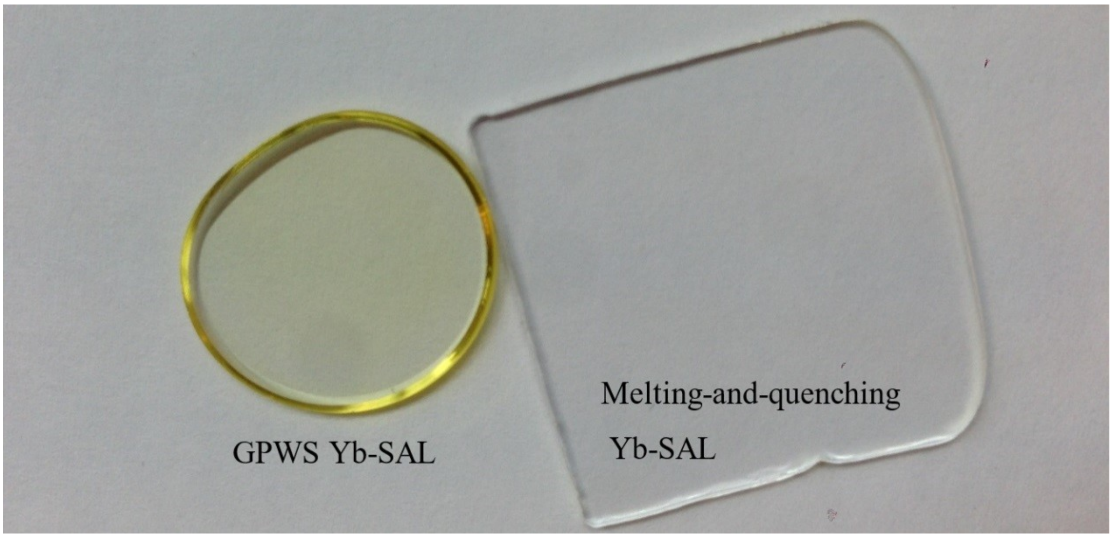

Figure 91. Yb-SAL glass sintered in gas pressure sintering furnace (1500 °C/50 bar/60 min/argon) and prepared by melting-and quenching (1650 °C/3 hours/air).

same situation for Yb-SAL glass in argon atmosphere. It is found that Yb-SAL glass becomes yellow from colorless Yb-SAL glass powder after sintering in gas sinter furnace as shown in Figure 91. The change of color attributes directly to the additional absorption peak at about 334 nm as shown in the spectrum in Figure 92. Kirchhof[119] has also reported this in his study of formation of Yb^{2+} in reductive collapsing, in which Yb^{2+} has increased the stability against photodarkening[120] and UV induced damage. According to Liu[121] et al., such 334 nm band, associated to the 4f - 5d transition of Yb^{2+} ions ($4f^{14} \rightarrow 4f^{13}5d^{1}$), can also been found in Yb doped silica glass prepared by vacuum sintering. As reported by Kirchhof[119], the formation of Yb^{2+} is associated to the oxygen deficiency groups (ODCs) generated in reductive atmosphere (e.g. H_2, He, CO, Ar). In our GPWS process, argon is used over 1000 °C so it must be dry. Although the temperature for melting Yb-SAL glass has reached 1650 °C, there is sufficient oxygen in the air. Therefore, the Yb-SAL glasses melted in air is colorless as shown in Figure 91. Kirchhof[119] has developed a quantitative method for determination of Yb^{2+} concentration in low Yb doped (<0.5 mol%) aluminosilicate glass prepared by MCVD. It is done by estimating the generated OH content after sufficiently reacted with H_2 stream at 1700 °C:

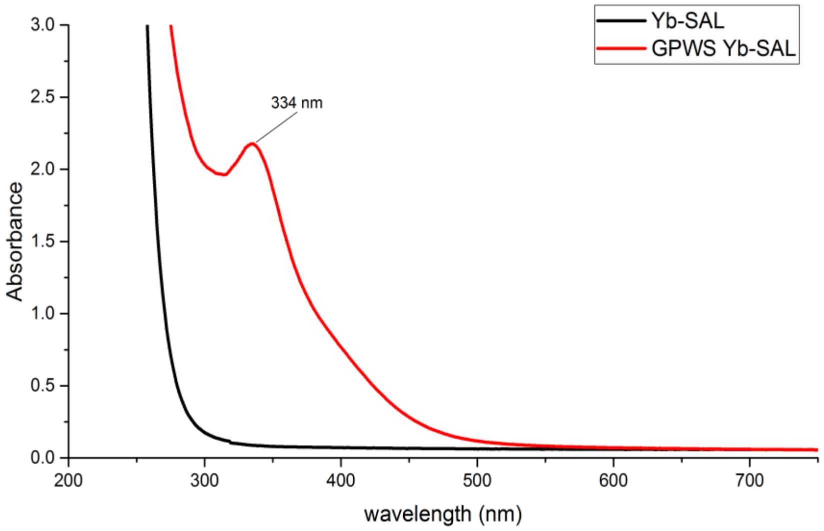

Figure 92. Absorption spectra of GPWS Yb-SAL glass (1500 °C/50 bar/60 min/argon) and Yb-SAL glass (1650 °C/3 hours/air) prepared by traditional melting-and quenching process. Sample thickness: 1.0 mm.

$$Yb_2O_3 + H_2 \leftrightharpoons \qquad \cdot H_2O \tag{64}$$

A coefficient of 500 cm^{-1}/mol% (YbO) has been derived for determination of the Yb^{2+} concentration in its UV/VIS absorption coefficient spectra (the formation of Si-H and

Si-OH are neglected). With such a coefficient, it is concluded that 0.1 mol% of Yb^{2+} has been reduced from initially 2 mol% Yb^{3+} in the Yb-SAL glass shown in Figure 92. In this case, about 5% of the Yb^{3+} was reduced to Yb^{2+}.

Shen[122] reported the role of Al^{3+} ions in such reduction behavior. It boosts the formation of ODCs (220 nm), which is important for the reduction transformation $Yb^{3+} \rightarrow Yb^{2+}$ in aluminosilicate glass. He demonstrated an Yb doped silica glass without Al^{3+} ions sintered in CO[122]; no Yb^{2+} ions were found under the same conditions. This implies that the Al^{3+} ions not only assisted indirectly (boost the formation of ODCs) but also directly take part in the generation of Yb^{2+}.

Two Yb-SAL glass samples that have been prepared in argon are shown in Figure 93. They were sintered at the same temperature but for different times. In the short time sintered sample, it is shown that the yellow color (Yb^{2+}) is initiated from the surface of the sample (Figure 93a), where Yb^{3+} ions have direct contact to the argon atmosphere. The reductive argon atmosphere generates ODCs on the surface at high temperature, or equivalently, the oxygen on the surface of the glass diffuses into the argon atmosphere. These ODCs then diffuse into the inner part of the sample. With the help of ODCs and Al^{3+}, Yb^{3+} is gradually reduced to Yb^{2+}. This results in the yellow color (absorption near 330 nm) observed in the full body in Figure 93b. Similar results can be found under vacuum, which is not demonstrated here. Figure 94 shows that the initial temperature for such reduction behavior can begin at 1000 °C

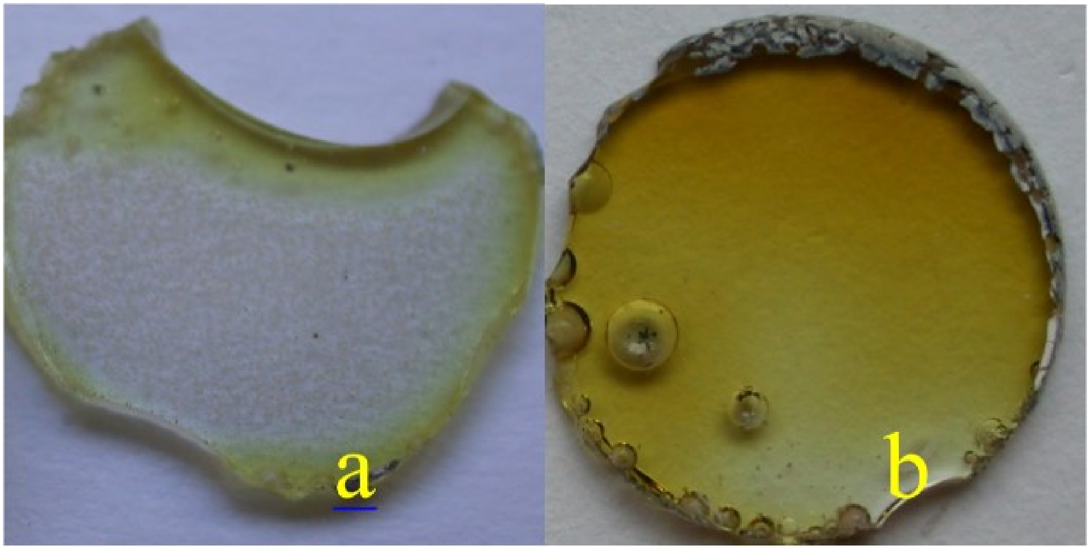

Figure 93. Yb-SAL glass powder sintered at 1500 °C for (a) 5 min and (b) 60 min at 1 bar argon, respectively.

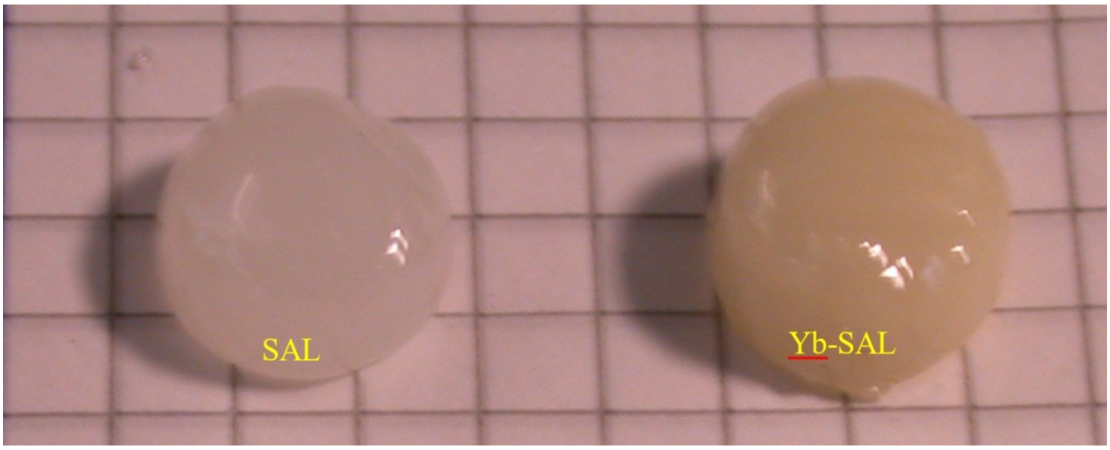

Figure 94. SAL and Yb-SAL glass sintered in vacuum at 1000 °C for 1 hour.

but at a much lower rate.

As it is reported in photodarkening studies[123,124] Yb^{2+} ions are responsible for the time-dependent photo-induced absorption occurred in fiber lasers. This source of loss is not beneficial in guiding lasers in fiber. However, the Yb^{2+} ions can improve the photoluminescence (PL) for the application of white light generation[125,126]. Depending on different applications, the oxidation behavior of the atmosphere gas in GPWS should be carefully chosen. For example, the non-reductive gas, such as CO_2, can be considered if the formation of Yb^{2+} is not desired

6.5.3 Summary for absorption groups.

Two important absorption groups have been found: the creation of Yb^{2+} and elimination of weakly associated OH groups in GPWS SAL glass. The reduction behavior in GPWS Yb-SAL glass occurs generally at temperatures from 1000 °C to 1550 °C so as the elimination of OH groups. The elimination of OH groups has been observed even at samples sintered for 5 min. If Yb^{2+} is not desired, a 5 min GPWS process should be taken as recommended dwelling time at 1500 °C to limit the formation of Yb^{2+} on the surface. It will be practical to control the Yb^{2+} concentration by tuning the dwelling time instead of temperature. Alternatively, using a non-reductive gas atmosphere should be considered.

6.6 Bubbles

Bubbles are problematic in optical glass due to scattering losses. Entrapped gases or decomposition of glass components usually causes the formation of bubbles. The environmental gases can be trapped in glass melts during the melting-and-quenching process. One of the most highlight benefit in using GPWS is the ability to prepare bubble-free glass bulk in a short time.

6.6.1 Bubble free glasses prepared by GPWS

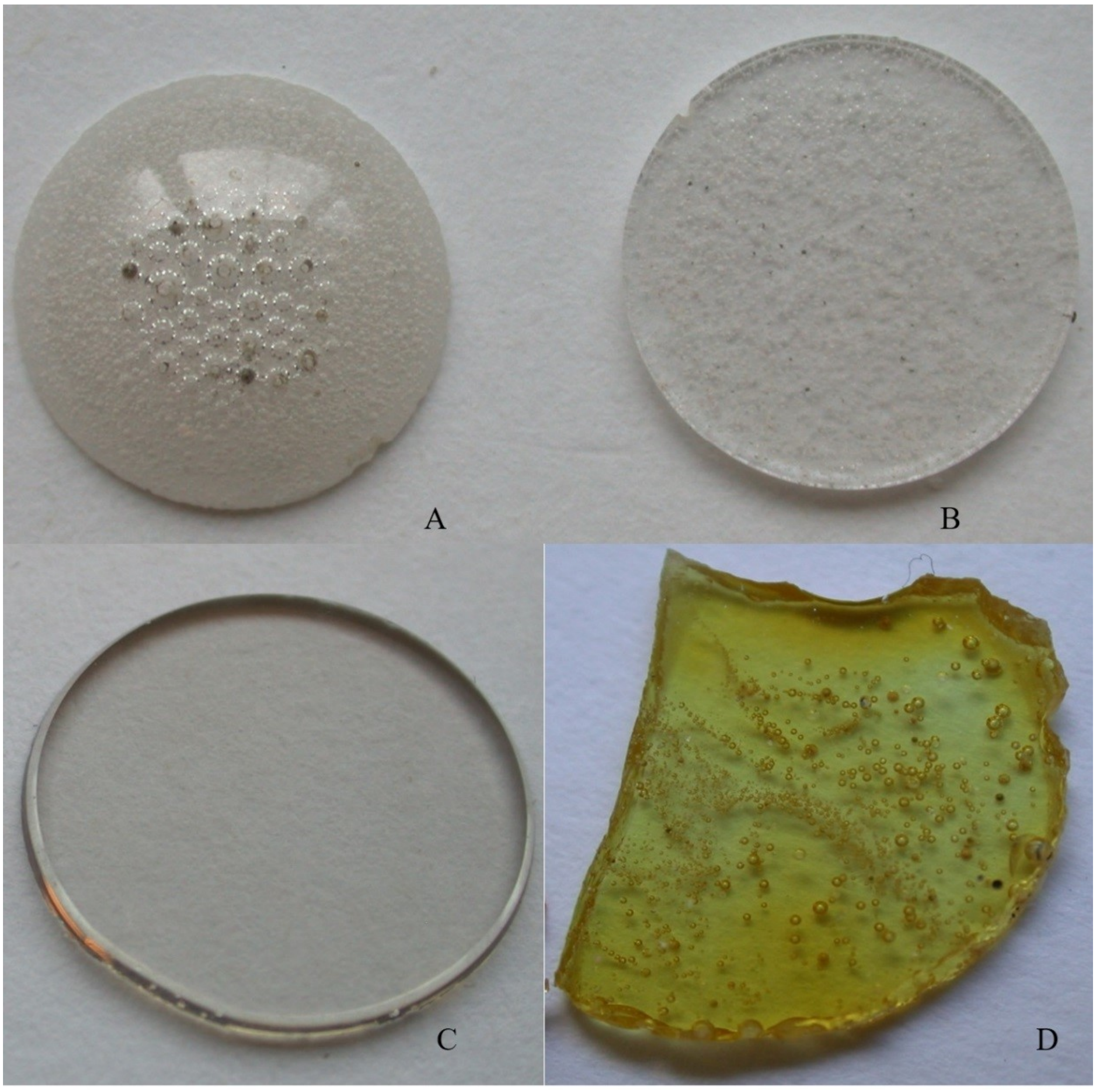

Figure 95. Pictures of (A) top and (B) polished middle slice of SAL glasses sintered at 1500 °C for 1 hour in vacuum. The Yb-SAL glass sintered at the same condition is shown in (D). The GPWS SAL glass sintered at 1550 °C for 1 hour at 50 bar argon is shown in (C).

Figure 95A and B show the SAL glass sintered at 1550 °C for 1 hour in vacuum while Figure 95D exhibits the Yb-SAL glass sintered at the same condition. In these three pictures, many bubbles are embedded in the glass. Figure 95C shows the GPWS SAL glass sintered at 1550 °C for 1 hour at 50 bar of argon without bubbles. In order to examine if there is any compressed entrapped gas in this sample, additional heat treatment at 1550 °C was carried out for 1 hour in vacuum. The GPWS SAL glass in Figure 95C remains the same, without seeing any bubble restored from the glass matrix. This implies that the vacuum bubbles were compressed without any entrapped gases. As it is already demonstrated in the microstructure section, the SAL glasses sintered in vacuum at 1000 °C can be fully densified. Hence, the bubbles observed in Figure 95A, B and D attribute to the glass decomposition. Correlating these bubbles and the elimination of “free” OH groups as discussed in previous section, these bubbles are probably initiated by released water vapor at 1550 °C. Even though all the gaseous water in the bubbles will finally diffuse out of the glass by continuous evacuation, the remaining vacuum bubbles need time to collapse. This mechanism explains the observed phenomenon supposed that the rate of the decomposition is much higher than the diffusion rate of OH groups through the glass in order to give rise to vacuum bubbles. Because no external pressure is present in vacuum sintering, the capillary stress is the only driving force to collapse. It becomes very slow if the viscosity is high and the bubbles are large. On the other hand, if external pressure is applied, vacuum bubbles collapse rapidly. HIP41 can serve as an example which was sintered at 1550 °C for 0 min at 50 bar and which is bubble free.

6.6.2 Compression of bubbles with entrapped gases

In addition to collapse vacuum bubbles, the application of external gas can also be used to compress previous existing bubbles in glass body with entrapped gases. Figure 96

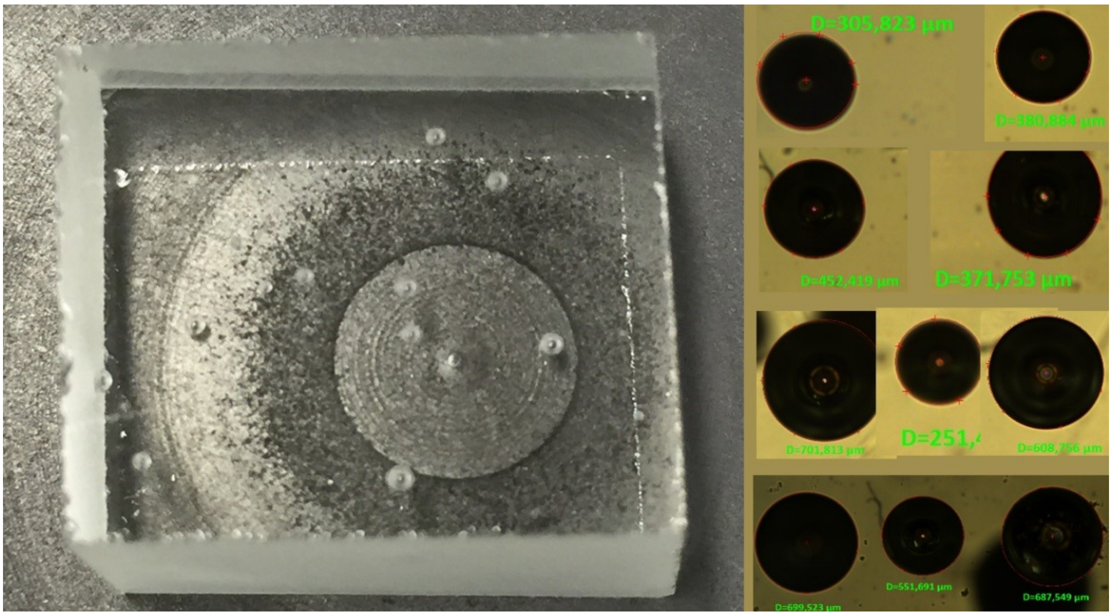

Figure 96. SAL glass block (1 cm x 1 cm x 8 mm) with bubbles (entrapped gases) and the microscopy of its all spherical bubbles.

shows the SAL glass block that is melted and quenched in atmospheric pressure. Perfectly circular bubbles with entrapped gases are seen in microscopy. The average diameter of all these bubbles is 501 µm, measured by microscopy. These blocks are then given to a gas pressure sintering furnace at 1050 °C for 30 min at 50 bar and 100 bar, respectively. The initial bubbles diameter of 500 µm (average) has been compressed to 190 µm and 144 µm under 50 bar and 100 bar, respectively as shown in Figure 97. The initial spherical bubbles in the starting glass block became non-spherical

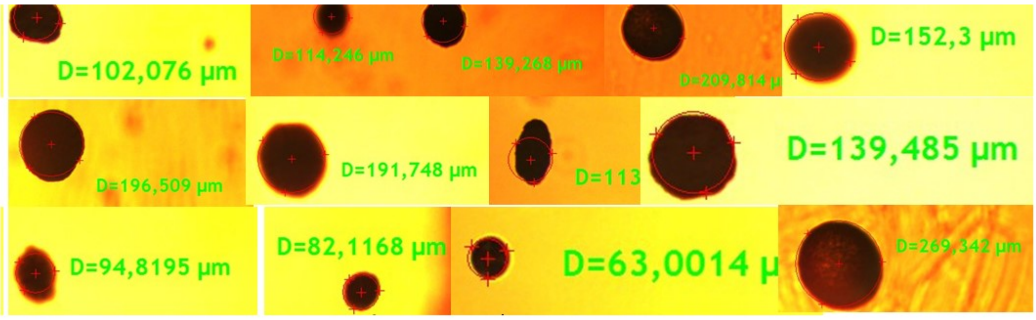

a) 1050 °C/30 min/100 bar

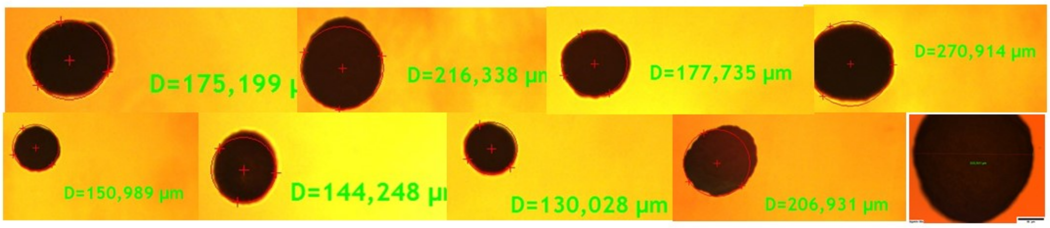

b) 1050 °C/30 min/50 bar

Figure 97. Microscopy of bubbles in SAL glass block after treated at 1050°C for 30min under b) 50bar) and a) 100bar respectively.

after compression by argon gas pressure. This indicates anisotropic viscosity inside the glass. Figure 98 demonstrates FEM simulations results of inhomogeneous bubble shape

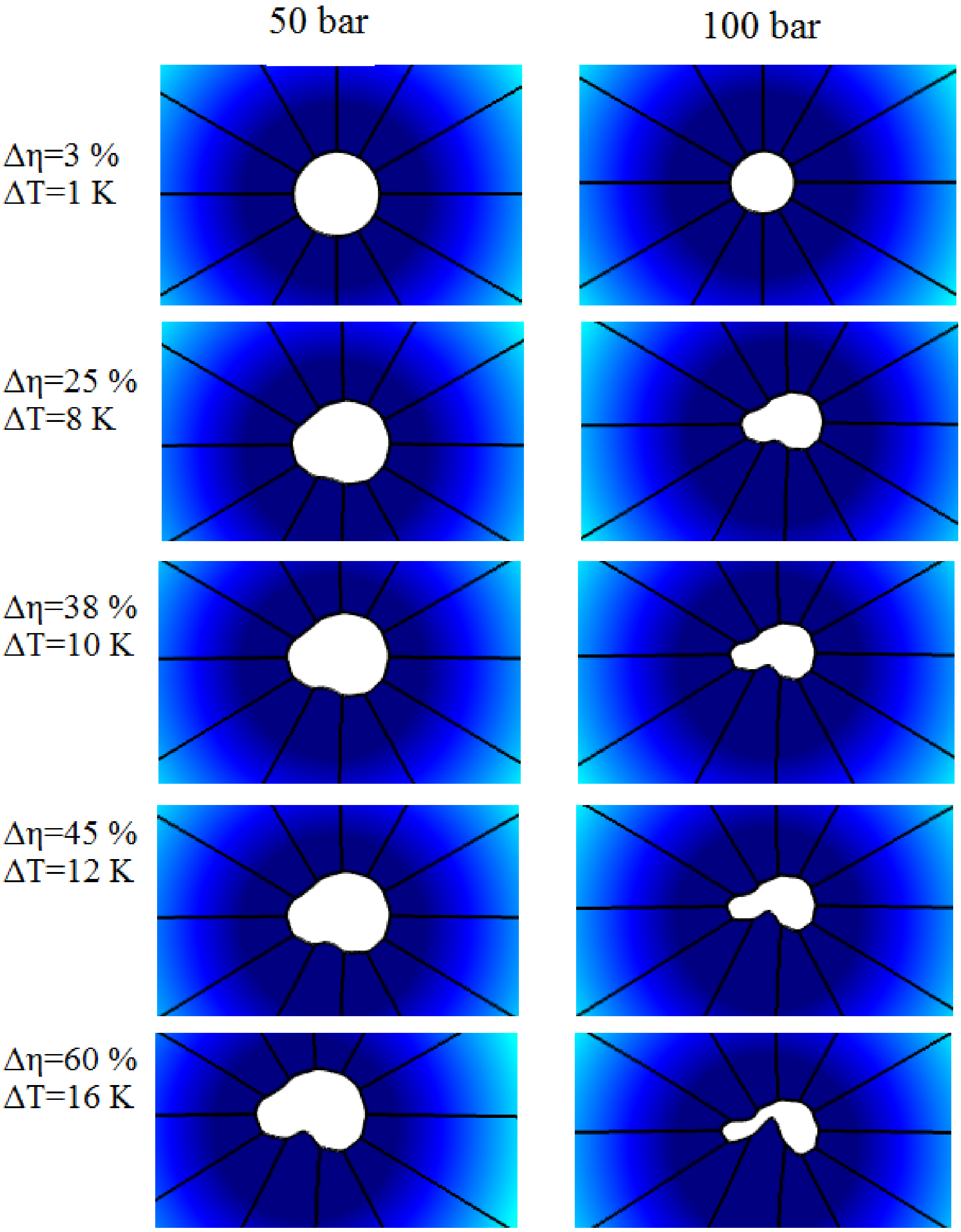

Figure 98. FEM simulation of bubble compression under inhomogeneous viscosities from perfect spherical bubbles. The variations of viscosity in percentages as well as the corresponding temperature difference are presented on the left hand side.

due to different variation in viscosity. The corresponding temperature variations can be calculated using Eq. (56). The results show that a variation of viscosity about 25% - 37.5% causes the non-spherical bubble shapes corresponding to about 10 K variation in the glass. Such temperature variation is coincident with the manufacture's instruction (FCT).

Table 9.Diameter of bubbles measured in microscopy

Bubble No.	1	2	3	4	5	6	7	8	9	10	11	12	13	Ave rage	St. Dev.
Starting (µm)	700	552	688	702	251	452	609	306	372	381				501	171
GS139 (µm)	175	234	216	271	178	151	144	130	207					190	46
GS143a (µm)	102	114	139	210	269	197	192	113	95	82	63	152	139	144	59

6.6.3 Summary for bubbles

In general, the application of external gas pressure after vacuum sintering – GPWS is quite advantageous in accelerating glass sintering where diffusive gas decomposition occurs. In case of diffusive gas decomposition in glass at sintering temperatures, the GPWS can guarantee a bubble free sintered glass. The ability of compressing bubbles with gas entrapped has also been demonstrated with GPWS technology. Additionally, it has been shown that at 1050 °C about 10 K is varied in the SAL glass.

Conclusion

SAL glasses have many innovative applications in high power lasers. However, some of the compositions are limited to the melting temperature of Pt crucibles at about 1700 °C. Therefore, an alternative method is proposed to prepare bulk glasses from high melting crystalline powders by two steps: the vitrification of the crystalline powder and a subsequent consolidation process. Consequently, the GPWS procedure was developed for one of the basis of this method: to consolidate the already vitrified amorphous powders. In this work, the high melting SAL glass has been taken as the model glass. Since the working temperature is significantly altered, the GPWS SAL glasses have been characterized in five aspects of inhomogeneities: crystallization, knots, striae, absorption groups and bubbles. It appears to be a suitable method to consolidate SAL glasses at 1000 °C to 1200 °C, provided that no impurities such as silica glass/quartz grains exist. Such low temperature range is preferred because the properties of the starting particles are more likely to maintain at high viscosity range. As a result, the consolidation procedure will not alter the powder properties. The 1200 °C to 1400 °C can be used if no failures such as silica/quartz grains are present in the powder mixture or when they are dissolved at high temperature first. Otherwise, Mullite crystallization occurs. The higher temperature range of 1400 °C to 1550 °C can be excluded by the facts that the formation of striae (both viscosity and diffusion coefficient are low) and phase separation are observed, which degrades the glass homogeneity.

With the here developed viscous stretching measurement as well as the FEM Simulation results, the viscosity of the glass melt, diffusion coefficients for Al and La groups and surface tension of the SAL glass have been determined. This viscous stretching method is not limited to single viscosity value at a certain temperature point, but delivers at first time a continuous viscosity-temperature dependence for low to middle temperature range. These results were successfully applied to the pressure assisted viscous sintering theory to determine the procedure parameters including working temperatures, external gas pressures and the dwelling time. It is found that a low pressure of 50 bar, for instance, is sufficient for GPWS to accelerate the sintering rate as if 148 nm particles were used. As a result, 50 – 100 µm large particles are fine enough to use in GPWS procedure. The only necessary condition for all the above parameters to become available is that a closed surface has been built in the first (P1) stage of the GPWS, which was found sufficient at 1000 °C for 1 hour using 50 – 100 μm SAL glass particles.

Compared to normal vacuum sintering, the GPWS method sinters in higher rate and is able to compensate the loss of sintering rate by using large particles. The GPWS method provides also the ability to suppress bubble formation at high temperature, which is due to gas decomposition rather than entrapped gas. If the gas is kind of high diffusive one, the corresponding bubbles can be closed by GPWS procedure. For the Yb-SAL glass, Yb^{2+} ions can be generated from partial reduction of Yb^{3+} ions via using insufficient oxygen atmosphere, such as argon. Compared to the SAL glasses prepared from conventional melting and quenching in air, the GPWS SAL glasses are free of OH absorption peaks that provides better transmission properties in the middle infrared range.

For future work, the lowering of the concentration of silica in our SAL glass composition will be recommended (~5 %) to avoid phase separation. Care should be taken in preparation of glassy powder in the vitrification process to avoid inclusions from silica/quartz grains. The change of the atmosphere – CO_2 instead of argon should be tested in order to minimize the reduction of Yb^{3+} in GPWS Yb-SAL glasses.

Finally, we can conclude that GPWS is an efficient consolidation procedure that allows sintering at lower temperature/high viscosity, for a shorter time, using larger starting particles. The resulting bubble-free and OH-free GPWS SAL glasses have the potential to deliver homogeneous high melting glass material in high quality.

Zusammenfassung

SAL-Gläser finden viele innovative Anwendungen in Hochleistungslasern. Dennoch ist die Herstellung einiger hochschmelzender Kompositionen durch die Schmelztemperatur von Pt-Tiegeln von 1700 °C nicht möglich. Folglich wird nun eine alternative Methode vorgeschlagen, um kompaktes Glas aus kristallinem Pulver mit hohem Schmelzpunkt in zwei Schritten anzufertigen: die Glasbildung aus dem kristallinen Pulver mit anschließendem Konsolidierungsprozess.

Daraus folgend wurde das GPWS-Verfahren entwickelt, um das bereits glasig-amorphe Pulver zu verdichten. In dieser Arbeit wurde SAL-Glas als Modellsystem verwendet. Da die Arbeitstemperatur deutlich verändert wurde, wurden die GPWS-SAL-Gläser hinsichtlich der folgenden fünf Inhomogenitäten charakterisiert: Kristallisation, Steinchen, Schlieren, Absorptionsgruppen und Blasen. Es zeigt sich, dass es sich bei GPWS um eine geeignete Methode handelt, um SAL-Gläser bei Temperaturen zwischen 1000 °C und 1200 °C zu verdichten, vorausgesetzt, dass keine Verunreinigungen, wie z.B. Siliziumdioxidkörner/Quarzkörner im Glas vorhanden sind. Dieser niedrige Temperaturbereich wird vorgezogen, da die Eigenschaften der Ausgangspartikel bei hoher Viskosität eher erhalten bleiben und damit der Konsolidierungsprozess die Pulvereigenschaften nicht verändert. Der Temperaturbereich von 1200 °C bis 1400 °C kann nur dann verwendet werden, wenn keine Fehler wie Siliziumdioxidkörner/Quarzkörner in der Pulvermischung vorhanden sind oder wenn diese zuerst bei hohen Temperaturen aufgelöst werden. Anderenfalls entstehen Mullit-Kristalle. Ein höherer Temperaturbereich von 1400 °C bis 15550 °C kann ausgeschlossen werden, da sich Schlieren bilden (niedrige Viskosität und niedriger Diffusionskoeffizient) und es zur Phasenseparation kommt, was die Glashomogenität verschlechtert.

Anhand der hier entwickelten Messmethode des viskosen Stretchings und der FEM Simulationsresultate konnten die Viskosität der Glasschmelze, die Diffusionskoeffizienten für Al- und La-Gruppen und die Oberflächenspannung der SAL-Gläser bestimmt werden. Die Methode des viskosen Stretchings ist nicht auf Viskositätsfixpunkte und damit nur wenige diskrete Temperaturen beschränkt, sondern liefert eine durchgehende Viskositäts-Temperatur-Abhängigkeit für niedrige bis mittlere Temperaturbereiche. Diese Resultate wurden erfolgreich in der Druck-unterstützten, viskosen Sintertheorie angewendet, um die Prozessparameter, wie z. B.

die Arbeitstemperaturen, den Gasaußendruck und die Verweilzeit festzulegen. Es wurde festgestellt, dass für GPWS ein geringer Druck von 50 bar ausreicht, um den Sinterprozess so zu beschleunigen, als ob 148 nm große Partikel verwendet würden. Folglich sind 50 – 100 µm große Partikel fein genug, um dem GPWS-Prozess unterzogen zu werden. Die einzige notwendige Voraussetzung, damit alle genannten Parameter anwendbar sind, ist, dass in der ersten Stufe des GPWS (P1) eine geschlossene Oberfläche erzielt wird. Das konnte bei 1000 °C innerhalb 1 h mit 50 – 100 µm großen Glaspartikeln erreicht werden.

Im Vergleich zum Sintern bei Normaldruck sintert die GPWS-Methode schneller und ermöglicht es damit, den Verlust der Sinterrate bei der Verwendung größerer Partikel zu kompensieren. Die GPWS-Methode ermöglicht es ebenfalls, der Bildung von Blasen bei hohen Temperaturen vorzubeugen, welche eher durch eine Gaszersetzung als durch Gaseinschlüsse entstehen. Sollte es sich um ein schnell diffundierendes Gas handeln, können die entsprechenden Blasen durch den GPWS-Prozess entfernt werden. Beim Yb-SAL-Glas können Yb2+-Ionen durch die partielle Reduktion von Yb3+-Ionen unter einer sauerstoffarmen Atmosphäre, wie z.B. Argon, generiert werden. Verglichen mit den SAL-Gläsern, welche durch ein herkömmliches Schmelz- und Quenching-Verfahren an Luft hergestellt wurden, sind die GPWS-SAL-Gläser frei von OH-Absorptionspeaks, was zu besseren Transmissionseigenschaften im mittleren Infrarotbereich führt.

Für zukünftige Arbeiten empfiehlt sich eine Verringerung des Quarzgehaltes (um etwa 5 %) in den SAL-Gläsern, um einer Phasenseparation vorzubeugen. Des Weiteren muss während der Herstellung des Glaspulvers im Glasbildungsverfahren darauf geachtet werden, Einschlüsse durch Siliziumdioxidkörner/Quarzkörner zu vermeiden. Ein Wechsel der Atmosphäre – CO2 anstelle von Argon – sollte getestet werden, um die Reduktion von Yb3+ in GPWS-Yb-SAL-Gläsern zu minimieren.

Schließlich kann festgestellt werden, dass GPWS einen effizienten Konsolidierungsprozess darstellt, welcher das Sintern bei niedriger Temperatur/hoher Viskosität in einem kürzeren Zeitraum und mit größeren Startpartikeln ermöglicht. Dieser Prozess hat das Potenzial, homogenes, hochschmelzendes und hochwertiges Glas zu liefern.

CV

Personal Information

Name:	Pan
Given name:	Zhiwen
Date of birth:	28.05.1981
Place of birth:	Guangdong, China

Education

2000-2004	Bachelor	Sun Yat-sen University, China	Material Physics
2004-2007	Master	Sun Yat-sen University, China	Condensed Physics

Working experience

2010-2015	PhD student	Leibniz Institute of Photonic Technology
2015-	Researcher	Otto Schott Institute of Materials Research

location, Date

Signature of the author

Selbständigkeitserklärung

Ich erkläre, dass ich die vorliegende Arbeit selbständig und unter Verwendung der angegebenen Hilfsmittel, persönlichen Mitteilungen und Quellen angefertigt habe.

Ort, Datum	Unterschrift des Verfassers/ der Verfasserin

References

---

1 J. E. Shelby, *Introduction to Glass Science and Technology, 2nd* (the Royal Society of Chemistry, New York, 2005), Chapter 7.

2 N. P. Bansal and R. H. Doremus, *Handbook of Glass Properties* (Academic Press, Florida, 1986).

3 J. R. Gonteman and M. A. Weinstein, Fiberglass and Glass Technology (Springer, UK, 2010), Chapter 11, pp. 431-451.

4 K. Schuster, S. Grimm, A. Kalide, J. Dellith, M. Leich, A. Schwuchow, A. Langner, G. Schötz, H. Bartelt, “Evolution of Fluorine Doping Following The REPUSIL Process for the Adjustment of Optical Properties of Silica Materials”, Opt. Mater. Express **5** (2015) 887.

5 H. Roggendorf, H. Schmidt, “Sol-Gel Processing - an Alternative Way to Glasses for Optoelectronics“, SPIE 1128 (1989) 40.

6 J. Frenkel, “Viscous Flow of Crystalline Bodies under the Action of Surface Tension”, J. Phys. **4** (1945) 385-391.

7 Lockheed Martin, 2014, http://www.lockheedmartin.com/us/newspress-releases/2014/january/140128-mst-lockheed-martin-demonstrates-weapons-grade-high-power-fiber-laser.html

8 G. Overton, A. Nogee and C. Holton, “Laser Manufacturers are Tired of our Uncertain Economy and Eager to Focus on Emerging Consumer and Industrial Innovations That Could Spark New Growth for the Worldwide Laser Industry.”, (Laser Focus World, 2014), http://www.laserfocusworld.com/articles/print/volume-50/issue-01/features/laser-marketplace-2014-lasers-forge-21st-century-innovations.html. (June.2015)

9 M. J. Dejneka et al., “La_2O_3–Al_2O_3–SiO_2 Glasses For High-Power, Yb^{3+}-Doped, 980-nm Fiber Lasers“, J. Am. Ceram. Soc., **85** (2002) 1100–106.

10 O. G. Okhotnikov, *Fiber Lasers* (Viley-Vch, Weinheim, 2012), Chapter 1-2.

11 R. J. Mears, L. Reekie, I.M. Jauncey And D. N. Payne, “Low-Noise Erbium-doped Fibre Amplifier at 1.54μm”, Electron. Lett., **23** (1987) 1026–1028.

12 P. Wang, D. Weng, K. Li, Y. Liu, X. Yu And X. Zhou, “Multi-Wavelength Erbium-Doped Fiber Laser Based on Four-Wave-Mixing Effect in Single Mode Fiber and High Nonlinear Fiber”, Opt. Express **21** (2013) 12570-12578.

13 Institute of Applied Physics, “Ultrafast Fiber Oscillators”, (IAP 2014), http://www.iap.uni-jena.de/fiber+_+waveguide+lasers/research/ultrafast+fiber+oscillators.html. (June.2015)

14 Research Group Introduction, “Fiber Sensors“, (IPHT Jena, 2014), http://www.ipht-jena.de/en/research-units/research-groups/fiber-sensors.html. (June 2015)

15 M. J. F. Digonnet, *Rare-earth-doped Fiber Lasers and Amplifiers* (CRC Press, New York, 2001), Chapter 1.

16 A. G. Clare, “Rare Earths in Glasses for Laser Applications“, K. Eng. Mater. **94-95** (1994) 161-180.

17 N. Troy et al., “Structural Modification in Er-Yb Doped Zinc Phosphate Glasses with Megahertz Repetition Rate Femtosecond Pulses”, SPIE Proc. **8247** (2012) 82470U.

18 J. E. Shelby, “Rare Earths as Major Components in Oxide Glasses“, Key Eng. Mater. **94-95** (1994) 1-42.

19 B. Pahari, S. Iftekhar, A. Jaworski, K. Okhotnikov, K. Jansson, B. Stevensson, J. Grins and M. Ede´N, “Composition-Property-Structure Correlations of Scandium Aluminosilica glasses Revealed By Multinuclear

45Sc, 27Al and 29Si Solid-State NMR", J. Am. Ceram. Soc., **95** (2012) 2545–2553.

20 L. Bois Etc., "Aqueous Alteration of Lanthanum Alumino-Silica glasses", J. Non-Cryst. Sol. **276** (2000) 181.

21 D. Litzkendorf, S. Grimm, K. Schuster, J. Kobelke, A. Schwuchow, A. Ludwig, J. Kirchhof, M. Leich, S. Jetschke, J. Dellith, "Study of Lanthanum Aluminum Silica glasses for Passive and Active Optical Fibers", Int. J. Appl. Glass Sci., **3** (2012) 321–331.

22 S. Kuhn, A. Herrmann, J. Hein, M. C. Kaluza, C. Rüssel, "Sm^{3+}-Doped La_2O_3–Al_2O_3–SiO_2-Glasses: Structure, Fluorescence and Thermal Expansion", J. Mater. Sci. **48** (2013) 8014–8022.

23 W. Vogel, *Glass Chemistry* (Springer-Verlag, Berlin, 1994), Chapter 1.

24 F. Farges, D. R. Neuville and G. E. Brown Jr., "Structural Investigation of Platinum Solubility in Silica Glasses", Am. Mineral. **84** (1999) 1562–1568.

25 A. R. Boccaccini, W. Stumpfe, D. M. R. Taplin, C. B. Ponton, "Densification and Crystallization of Glass Powder Compacts During Constant Heating Rate Sintering", Mater. Sci. Eng. **A219** (1996) 26-31.

26 S-J. L. Kang, *Sintering, Densification, Grain Growth and Microstructure* (Elsevier Butterworth-Heinemann, Great Britain, 2005), Chapter 2.

27 X. Xiong, H-C. Sheng, J. Chen, P-P. Yao, "Effects of Sintering Pressure and Temperature on Microstructure and Tribological Characteristic of Cu-Based Aircraft Brake Material", Trans. Nonferrous Met. Soc. China **17** (2007) 669-675.

28 R. M. German, *Sintering, from Empirical Observations to Scientific Principles* (Elsevier Oxford, UK, 2014), Chapter 12.

29 W. Yang, J. Mao, W. Wang, J. Zou and R. Zhou, "Effects of Heat Treatment on Prior Particle Boundary Precipitation in a Powder Metallurgy Nickel Base Superalloy", Adv. Perform. Mater. **2** (1995) 269-279.

30 T. G. Mayerhofer, Z. Shen, E. Leonova, M. Edén, A. Kriltz and J. Popp, "Consolidated silica glass from nanopartcles". J. Solid State Chem. 181(2008) 2442-2447.

31 N. Hirosaki, A. Okada, "Gas-Pressure Sintering Map for Silicon Nitride-Based Materials", in *Hot Isostatic Pressing— Theory and Applications* (Springer, Netherlands, 1992) pp.143-148.

32 G. E. Gazza, R. N. Katz, Mater. Res. Soc. Symposium Proceedings, **251** (1992) 199-209.

33 J. D. Mackenzie, "High-Pressure Effects on Oxide Glasses: I, Densification in Rigid State", J. Am. Cera. Soc. **46** (1963).

34 A. Sparavigna, "The Egyptian Sintered-Quartz Ceramics" http://philica.com/display_article.php?article_id=426. (Sep 2015)

35 D. Bonn, J. Eggers, J. Indekeu, J. Meunier and E. Rolley, "Wetting and Spreading", Rev.Mod. Phys. **81** (2009) 739-805

36 P. E. Wretblad, J. Wulff, "Sintering", Powder Metallugry, Am. Soc. Metals (1942) 36-59.

37 J. P. Hirth, "A Brief History of Dislocation Theory", Metall. Trans. A **16**A (1985) 2085-2090.

38 V. I. Trefilov, Y. V. Mil'man and I. V. Gridneva, "Role of Plastic Deformation in Sintering Covalent Crystals", Powder Metall. Met. C+ **33** (1994) 7-8.

39 R. A. Gregg And F. N. Rhines, "Surface Tension and the Sintering Force in Copper", Metall. Trans. **4**(1973) 1365.

40 J. Brett and L. Seigle, "Shrinkage of Voids in Copper", Acta Metall. Mater. **11** (1963).

41 I. Langmuir, "Surface Chemistry", Nobel lecture, (December 14. 1932)

42 H. Nakajima, "The Discovery and Acceptance of Kirkendall Effect: The Result of a Short Research Career", JOM. **49** (1997) 15-19.

43 R. E. Hoffman and D. Turnbull, "Lattice and Grain Boundary Self-Diffusion in Silver", J. Appl. Phys. **22** (1951) 634-639.

44 H. Mehrer, *Diffusion in Solids – Fundamentals, Methods, Materials, Diffusion-Controlled Processes* (Springer,

Berlin, 2007), Chapter 10-11.

45 W. D. Kingery and M. Berg, “Study of the initial stages of sintering solids by viscous flow, evaporation-condensation,and self-diffusion”, J. Appl. Phys. **26** (1955) 1205-1212.

46 D. Hull and D. J. Bacon, *Introduction to Dislocations, 4 Edition* (Butterworth Heinemann Oxford, UK, 2001), Chapter 3.

47 W. Schatt, H. E. Exner, E. Friedrich and G. Petzow, “Versetzungsaktivierte Schwindungsvorgänge beim Einkomponenten-Sintern”, Acta Metall. **30** (1982) 1367-1375.

48 M. F. Ashby, “A First Report on Sintering Diagrams”, Acta Metall. **22** (1974) 275-289.

49 F. B. Swinkels and M. F. Ashby, “A Second Report on Sintering Diagrams”, Acta Metall. **29** (1980) 259-281.

50 M. A. Lauffer, “Motion in Viscous Liquids”, J. Chem. Educ. **58** (1981).

51 M. M. Ristić and S. Dj. Milosević, “Frenkel's Theory of Sintering”, Sci.Sinter. **38** (2006) 7-11.

52 J. K. Mackenzie and R. Shuttleworth, “A Phenomenological Theory of Sintering”, Proc. Phys. Soc. B **62** (1949) 833.

53 G. W. Scherer, "Sintering of Low Density Glasses: I. Theory", J. Am. Ceram. Soc. **60** (1977) 236-239.

54 G. W. Scherer and D. L. Bachman, "Sintering of Low Density Glasses: II. Experimental Study", J. Am. Ceram. Soc. **60** (1977) 239-243.

55 G. W. Scherer, "Sintering of Low Density Glasses: III. Effect of a Distribution of Pore Sizes", J. Am. Ceram. Soc. **60** (1977) 243-246.

56 W. Ostwald, *Lehrbuch der Allgemeinen Chemie*, *2, part 1* (Leipzig, 1896).

57 R. M. German, P. Suri, S. J. Park, “Review: liquid phase sintering”, J. Mater. Sci. **44** (2009) 1-39.

58 R. L. Coble, “Sintering Crystalline Solids.I. Intermediate and Final Stage Diffusion Models”, J. Appl. Phys. **32** (1961) 787.

59 L. Rayleigh, “On the Capillary Phenomena of Jets”, Proc. R. Soc. A **29** (1879) 71-97.

60 R. J. Brook, “Pore-Grain Boundary Interactions and Grain Growth”, J. Am. Ceram. Soc, **52**(1969) 56-57.

61 F. N. Rhines, R. T. DeHoff, ”A Topological Approach to the Study of Sintering”, in *Modern Developments in Powder Metallurgy, vol. 4* (Plenum Press, New York, 1971), 173-188.

62 P. J. Wray, “The Geometry of Two-Phase Aggregates in Which the Shape of the Second Phase is Determined by its Dihedral Angle”, Acta Metall. **24** (1976) 125-135.

63 A. J. Markworth, “Growth of Inert-Gas Bubbles in Solids; Behaviour of Non-Uniform Size Distributions”, J. Mater. Sci. **7** (1972) 1225-1228.

64 F. C. Roesler, “Brittle Fractures near Equilibrium”, Proc. Phys. Soc. B **69** (1956) 981.

65 A. W. Neumann and J. K. Spelt, *Applied Surface Thermodynamics* ***63*** (CRC Press, New York, 1996), chapter 1.

66 Z. Z. Fang, Sintering of Advanced Materials (Woodhead Publishing, UK, 2010).

67 S-J. L. Kang, *Sintering, Densification, Grain Growth and Microstructure* (Elsevier Butterworth-Heinemann, UK, 2005), Chapter 4.

68 R. M. German, *Sintering, From Empirical Observations to Scientific Principles* (Elsevier Oxford, UK, 2014), Chapter 7.

69 H. Giesche, “Mecury Porosimetry: a General (Practical Overview)”, Part. Part. Syst. Charact. **23** (2006) 1-11.

70 K. S. W. Sing, “Adsorption Methods for Characterizatioin of Porous Materials”, Adv. Colloid Interfac. **76-77** (1998) 3-11.

71 G. W. Scherer, “Cell Models for Viscous Sintering”, J. Am. Ceram. Soc., **74** (1991) 1523-31.

72 Werner Vogel, *Glass chemistry* (Springer, Berlin, 1994), Chapter 13.

73 E. Arzt, M. F. Ashby and K. E. Easterling, “Practical Applications of Hot-Isostatic Pressing Diagrams: Four Case Studies”, Metall. Trans. A, **14A** (1983) 211-221.

74 R. L. Coble, “Diffusion models for hot pressing with surface energy and pressure effects as driving forces“, J. Appl. Phys. **41** (1970) 4798-807.

75 J. Kirchhof, “Reactor Problems in Modified Chemical Vapour Deposition (I)”, Cryst. Res. Technol. **20** (1985) 705-712.

76 W. H. Zachariasen, “The Atomic Arrangement in Glass”, J. Am. Chem. Soc., **54** (1932) 3841-3851.

77 J. E. Stanworth, “Oxide Glass Formation from the Melt“, J. Am. Ceram. Soc. **54** (1971) 61.

78 H. Mehrer, *Diffusion in Solids – Fundamentals, Methods, Materials, Diffusion-Controlled Processes* (Springer, Berlin, 2007), Chapter 16.

79 B. Messerschmidt, T. Possner and R. Goering, “Colorless gradient-index cylindrical lenses with high numerical apertures produced by silver-ion exchange“, Appl. Opt. **34** (1995) 7825-7830.

80 J. E. Shelby, *Introduction to Glass Science and Technolgy, Second Edition* (The Royal Society of Chemistry, New York, 2005), Chapter 8.

81 A. T. Young, “Rayleigh scattering”, Appl. Opt. **20** (1981) 533-535.

82 W. Vogel, *Glasfehler* (Springer, Germany, 1993).

83 B. Mehdikhani, G. H. Borhani, “Optical spectroscopy of sodium silica glasses prepared with nano- and micro-sized iron oxide particles”, Proc. Appl. Ceram. **7** (2013) 117-121.

84 W. Hergert, T. Wriedt, The Mie Theory, basics and applications (Springe,Berlin, 2012).

85 R. Kitamura, L. Pilon and M. Jonasz, “Optical constants of silica glass from extreme ultraviolet to far infrared at near room temperature”, Appl. Opt. **46** (2007) 8118-8133.

86 C. Gautam, A. K. Yadav and A. K. Singh, “A Review on Infrared Spectroscopy of Borate Glasses with Effects of Different Additives”, ISRN Ceram. **2012** (2012) 1-17.

87 E. L. Morales, K. M. Rocha, M. R. Chalita, W. Nose, M. P. Avila, “Comparison of optical Aberrations and contrast Sensitivity Between Aspheric and Spherical Intraocular Lenses”, J. Refract. Surg. **27** (2011) 723-728.

88 E. Abbe, H. Lawson, (Translated by H. E. Fripp), “A Contribution to the Theory of the Microscope and the Nature of Microscopic Vision”. Proc. BNS **1** (1876) 200–261.

89 F. A. Jenkins, H. E. White, *Foundamentals of Optics, 4th ed.* (McGraw-Hill, New York, 1976).

90 W. H. Zachariasen, “The Atomic arrangement in glass”, J. Am. Ceram. Soc. **54** (1932) 3841.

91. B. E. Warren, “X-Ray determination of the structure of glass”, J. Am. Ceram. Soc., **17** (1934) 249–254

92. B. D. Cullity, *Elements of X-RAY Diffraction, Second Edition* (Addison-Wesley, USA, 1956).

93 A. Ludwig, Diplomarbeit, *Untersuchungen zur Yb-dotierung in Lanthan-Alumosilikat-Gläsern und die Realisierung von optischen Fasern* (Fachhochschule Jena, Jena, 2012).

94 A. W. Date, *Introduction to Computational Fluid Dynamics* (Cambridge University Press, NewYork, 2005).

95 M. Kaviany, *Heat Transfer Physics* (Cambridge University Press, NewYork, 2008).

96 COMSOL Multiphysics (2015), http://www.comsol.com.

97 L. van der Tempel, “Thermal Conductivity of a Glass: II. The Empirical Model”; Glass Phys. Chem. 28 (2002) 147-152.

98 J. Leitner, P. Chuchvalec, D. Sedmidubsky, A. Strejc and P. Abrman, “Estimation of heat capacities of solid mixed oxides”, Thermochim. Acta **395** (2003) 27-46.

99 Z. Pan, J. Kobelke, K. Schuster and H. Bartelt, “Determination of effective axial temperature profile in tube furnaces via the viscous stretching method“, Opt. Mater. Express **5** (2015) 2024-2035.

100 E. L. Bourhis, Glass Mechanics and Technology (Wiley-VCH, 2007).

101 R. D. Shannon, “Revised Effective Ionic Radii and Systematic Studies of Interatomie Distances in Halides and Chaleogenides”, Acta Cryst. A **32** (1976) 751.

102 J. Marchi, D. S. Morais, J. Schneider, J. C. Bressiani and A. H. A. Bressiani, “Characterization of rare earth aluminosilicate glasses”, J. Non-Cryst. Solids **351** (2005) 863-868.

103 Wikipedia, “Agate”, http://en.wikipedia.org/wiki/Agate. (June 2015)

104 D. J. Duval, S. H. Risbud and J. F. Shackelford, *Ceramic and Glass Materials: Structure, Properties and Processing* (Springer, New York, 2008).

105 J. E. Shelby, *Introduction to Glass Science and Technology, 2nd* (the Royal Society of Chemistry, New York, 2005), Chapter 5.

106 Mindat, “Mullite”, http://www.mindat.org/min-2806.html. (June 2015)

107 D. J. Cassidy, J. L. Woolfrey and J. R. Bartlett, “The Effect of Precursor Chemistry on the Crystallisation and Densification of Sol-Gel Derived Mullite Gels and Powders”, J. Sol-Gel Sci. Technol. **10** (1997) 19-30.

108 S. Baghshahi, M. P. Brungs, C. C. Sorrell and H. S. Kim, “Surface crystallization of rare-earth aluminosilica glasses“, J. Non-Cryst. Solids **290** (2001) 208-215.

109 M. Kerker, *The Scattering of Light and Other Electromagnetic Radiation* (Academic Press, New York, 1969).

110 MiePlot, “A computer program for scattering of light from a sphere using Mie theory & the Debye series”, http://www.philiplaven.com/mieplot.htm. (Oct 2014)

111 M. Jensen, Y. Yue, “Effect of stirring on striae in glass melts”, J. Non-Cryst. Solids, **358** (2012) 349-353.

112 T. Suzuki, J. Konishi, K. Yamamoto, S. Ogura and K. Fukutani, “IR Practical Extinction Coefficients of Water in Alkali Lime Silicate Glasses Determined by Nuclear Reaction Analysis”, J. Am. Ceram. Soc. **98** (2015) 1794-1798.

113 H. Tomozawa and M. Tomozawa, “Diffusion of water into a borosilicate glass”, J. Non-Cryst. Solids **109** (1989) 311.

114 H. Scholze, “Der Einbau des Wassers in Gläsern. I. Der Einfluß des im Glas gelösten Wassers auf das Ultrarot-Spektrum und die quantitative ultrarotspektroskopische Bestimmung des Wassers in Gläsern,” Glastech. Ber. **32** (1959) 81–88.

115 T. Suzuki, J. Konishi, K. Yamamoto, S. Ogura and K. Fukutani, “Practical IR Extinction Coefficients of Water in Soda Lime Aluminosilicate Glasses Determined by Nuclear Reaction Analysis”, J. Non-Cryst. Solids **382** (2013) 66-69.

116 S. Kuhn, M. Tiegel, A. Herrmann, J. Körner, R. Seifert, F. X. Yue, D. Klöpfer, J. Hein, M. Kaluza and C. Rüsse, “Identification and Characterization of Surface Hydroxyl Groups by Infrared Spectroscopy”, Opt. Mater. Express, **5** (2014) 430-440.

117 R. L. David, *CRC Handbook of Chemistry and Physics* (CRC Press, Florida, 2005).

118 R. A. Nyquist and R. O. Kagel, *Infrared Spectra of Inorganic Compounds, (3800-45cm*$^{-1}$*)* (Academic Press, New Yokr, 1971).

119 J. Kirchhof, S. Unger, A. Schwuchow, S. Jetschke, V. Reichel, M. Leich, A. Scheffel, “The Influence of Yb^{2+} Ions on Optical Properties and Power Stability of Ytterbium-Doped Laser Fibers.” Proc. SPIE **7598** (2010) 75980B.

120 S. Jetschke, S. Unger, U. Röpke, J. Kirchhof, “Photodarkening in Yb Doped Fibers: Experimental Evidence of Equilibrium States Depending on the Pump Power“, Opt. Express **15** (2007) 14838-14843.

121 S. Liu, S. Zheng, C. Tang, X. Li, W. Xu, Q. Sheng, D. Chen, “Photoluminescence and Radioluminescence Properties of Yb^{2+}-doped Silica Glass”, Mater. Let. **144** (2015) 43-45.

122 Y. Shen, Q. Sheng, S. Liu, W. Li and D. Chen, “Effect of Aluminum Co-doping on the Formation of Yb^{2+} in Ytterbium-doped High Silica Glass”, Chin. Opt. Lett. **11** (2013) 051601.

123 S. Jetschke, S. Unger, U. Röpke and J. Kirchhof, “ Photodarkening in Yb Doped Fibers: Experimental Evidence of Equilibrium States Depending on the Pump Power“, Opt. Express **15** (2007) 14838 - 14843.

124 S. Jetschke, S. Unger, A. Schwuchow, M. Leich, V. Reichel and J. Kirchhof, “Photodarkening in Yb-doped Silica Fibers: Influence of the Atmosphere during Preform Collapsing”, Proc. SPIE **6873** (2008) 68731G.

125 L. Liu, R-J. Xie, N. Hirosaki, T. Takeda, C-N. Zhang, J. Li and X. Sun, “Photoluminescence Properties of β-

Sialon: Yb^{2+}, A Novel Green-Emitting Phosphor for White Light-Emitting Diodes", Sci. Technol. Adv. Mater. **12** (2011) 034404.

126 C. Xia, G. Zhou, Y. Han, X. Zhao and L. Hou, "Luminescence of Yb^{2+}, Yb^{3+} Co-doped Silica Glass for White Light Source", Opt. Mater. **34** (2012) 769-771.